

Nonreciprocity and Nonlinearity in Polymer Photonic Integrated Circuits

vorgelegt von
M. Sc.
Hauke Conradi
ORCID: 0000-0002-7799-4811

an der Fakultät II – Mathematik und Naturwissenschaften
der Technischen Universität Berlin
zur Erlangung des akademischen Grades

Doktor der Naturwissenschaften
- Dr. rer. nat. -

genehmigte Dissertation

Promotionsausschuss:

Vorsitzende: Prof. Dr. rer. nat. Ulrike Woggon, TU Berlin

Gutachter: Prof. Dr. rer. nat. Martin Schell, TU Berlin

Gutachter: Dr. rer. nat. Tim Schröder, HU Berlin

Gutachter: Prof. Dr. rer. nat. Janik Wolters, TU Berlin

Tag der wissenschaftlichen Aussprache: 22.06.2022

Berlin 2022

List of Publications

Journal contributions

- [1] H. Conradi et al., "Second Harmonic Generation in Polymer Photonic Integrated Circuits," *Journal of Lightwave Technology*, vol. 39, no. 7, pp. 2123–2129, 2021, doi: 10.1109/JLT.2020.3046371.
- [2] M. Kleinert, H. Conradi, H. Hübel, and B. Schrenk, "UNIQORN – Making quantum photonics affordable," *Laser Focus World*, Apr. 2019.
- [3] M. Happach, H. Conradi et al., "On-chip free beam optics on a polymer-based photonic integration platform," *Opt. Express, OE*, vol. 25, no. 22, pp. 27665–27670, 2017, doi: 10.1364/OE.25.027665.

Conference contributions

- [1] H. Conradi, "Tunable DBR Laser with Integrated Optical Isolator," *Optical Fiber Communications Conference and Exhibition (OFC)*, 2021, pp. 1-3.
- [2] H. Conradi et al., "Hybrid integration of a polarization independent optical circulator," in *2020 Photonics West*, San Francisco, USA, 112830J.
- [3] H. Conradi et al., "High Isolation Optical Isolator: A new Building Block for PolyBoard Photonic Integrated Circuits," in *2018 European Conference on Optical Communication (ECOC)*, 2018, pp. 1–3.
- [4] M. Weigel, H. Conradi et al., "3D Photonic Integration: Cascaded 1x1 3D Multi-mode Interference Couplers for Vertical Multi-layer Connections," *European Conference on Integrated Optics (ECIO), SPIE Digital Library*, Paris, France, Jun. 2020.
- [5] M. Kleinert, H. Conradi et al., "A platform approach towards hybrid photonic integration and assembly for communications, sensing, and quantum technologies based on a polymer waveguide technology," in *2019 IEEE CPMT Symposium Japan (ICSJ)*, Kyoto, Japan, Nov. 2019 - Nov. 2019, pp. 25–30.
- [6] M. Kleinert, H. Conradi et al., "Versatile micro-optical bench for photonic integration in quantum technology," *European Quantum Technology Conference (EQTC19)*, Grenoble, France Feb. 2019.
- [7] F. Laudenbach, M. Hentschel, M. Kleinert, H. Conradi, and H. Hübel, "Intrinsic entanglement generation on polymer-based integrated circuit," *Central European Workshop on Quantum Optics (CEWQO)*, Paderborn, Germany, June 2019.
- [8] M. Nuck, H. Conradi et al., "3D photonic integrated 4x4 multi-mode interference coupler," *undefined*, 2019 *Photonics West*, San Francisco, USA.
- [9] A. Polatynski, H. Conradi et al., "Virtual prototyping of complex photonic components and integrated circuits for polymer-based integration platform," in *2018 Photonics West*, San Francisco, USA, p. 1053624.
- [10] D. de Felipe, H. Conradi et al., "Ultra-Wide Band Tunable Lasers on the PolyBoard Polymer-Waveguide Based Photonic Integration Platform," in *2018 European Conference on Optical Communication (ECOC)*: 23-27 Sept. 2018, Rome, Italy, 2018, pp. 1–3.
- [11] M. Nuck, H. Conradi et al., "Low-Loss Vertical MMI Coupler for 3D Photonic Integration," in *2018 European Conference on Optical Communication (ECOC)*, 2018, pp. 1–3.
- [12] D. de Felipe, H. Conradi et al., "Polymer-Based Hybrid Photonic Integration for Flexible PIC Design," in *Integrated Photonics Research, Silicon and Nanophotonics: Part of Advanced Photonics : 24-27 July 2017, New Orleans, Louisiana, United States*, New Orleans, Louisiana, 2017, ITh2A.3.

Zusammenfassung

Optische Isolatoren und Zirkulatoren finden in der Optik zum einen Verwendung für den Schutz von Lasern vor ungewolltem optischen Feedback und zum anderen ermöglichen Zirkulatoren, vor allem in der Sensorik, die bidirektionale Transmission optischer Pfade. Eine fundamentale Anforderung an optische Isolatoren und Zirkulatoren ist, dass sie die Lorentz-Reziprozität brechen, weshalb beide Komponenten den nichtreziproken Elementen zugeordnet werden.

In dieser Arbeit wird die Integration nichtreziproker Elemente für die Realisierung optischer Isolatoren und Zirkulatoren in eine polymerbasierte photonische Integrationsplattform demonstriert. Die Integration der hierfür benötigten Faraday Rotatoren erfolgt über Chip-integrierte Freistrahlbereiche, die das Einsetzen optischer Materialien ermöglichen.

Die Realisierung des optischen Isolators erfolgt über die Integration eines Freistrahlisolators in das PolyBoard, wobei neben einer fundamentalen Charakterisierung des Isolators erstmals die Co-Integration mit einem abstimmbaren Distributed Bragg-Reflektor Laser mit Isolator demonstriert wird. Mit gemessenen optischen Verlusten unterhalb von einem dB und einer optischen Isolation größer als 40 dB zeigt der Isolator eine vergleichbare Performance zu kommerziellen Isolatoren in der Freistrahloptik.

Neben Isolatoren werden Zirkulatoren auf Basis von freistrahlintegrierten Faraday Rotatoren und Polarisationsstrahlteilern in einer ersten Variante und auf Basis eines Mach-Zehnder-interferometrischen Ansatzes in einem zweiten Demonstrator realisiert. Aufgrund der ferrimagnetischen Eigenschaften der Faraday Rotatoren fungieren die Zirkulatoren ebenfalls als selbsthaltende Schalter, die nur während des aktiven Schaltvorgangs Energiezufuhr benötigen. Gemessene optische Verluste der Zirkulatoren liegen im Bereich von 4 – 8 dB bei einer optischen Isolation von 9 – 18 dB.

Die Einbringung von Freistrahlbereichen in der integrierten Optik ermöglicht neben der Implementation nichtreziproker Elemente eine Vielzahl weiterer Anwendungsmöglichkeiten. Im zweiten Abschnitt dieser Arbeit wird die Integration nichtlinearer Lithiumniobat-Kristalle für Frequenzverdopplung demonstriert. Mit Hilfe eines Dauerstrichlasers und eines Femtosekunden Pulslasers wird dabei nicht nur die Erzeugung der zweiten, sondern auch der dritten und vierten Harmonischen im sichtbaren Wellenlängenbereich und somit die erste Erzeugung von sichtbarem Licht auf der verwendeten Polymer-Plattform demonstriert. Neben den genannten konkreten Anwendungsbeispielen beschreibt diese Arbeit die theoretischen Grundlagen von chipintegrierten Freistrahlbereichen mit Hilfe von GRIN-Linsen, genannt mikrooptische Bank, welche eine Vielzahl weiterer Anwendungsfelder eröffnet und eine Brücke zwischen der Freistrahloptik und der integrierten Optik bildet.

Abstract

Optical isolators and circulators are used in optics to protect sensitive elements, such as lasers, from unwanted feedback. Especially in sensing, optical circulators also enable the bidirectional transmission of optical paths. A fundamental requirement of optical isolators and circulators is that they break Lorentz reciprocity, thus both components are classified as non-reciprocal elements. In this work, the implementation of non-reciprocal elements in polymer-based photonic circuits via collimated chip-integrated free-space sections is demonstrated.

Optical isolators are realized by integrating a separately assembled free-space isolator into this free-space section. In addition to a fundamental characterization, a co-integration of a tunable distributed Bragg reflector laser together with an isolator is demonstrated for the first time in integrated photonics. With measured optical loss below 1 dB and an optical isolation greater than 40 dB, the isolator shows comparable performance to commercial isolators in free-space optics.

Circulators based on free-beam integrated Faraday rotators and polarization beam splitters are realized in a first variant and based on a Mach-Zehnder interferometric approach in a second demonstrator. Due to the ferrimagnetic properties of the Faraday rotators, the circulators also act as latching switches that require energy supply only during the active switching process. Measured optical losses of the circulators are in the range of 4 - 8 dB with an optical isolation of 9 - 18 dB.

The integration of free-space sections in integrated optics enables a variety of other applications beyond the implementation of non-reciprocal elements. In the second part of this thesis, the integration of nonlinear lithium niobate crystals for second-harmonic generation from 1550 nm to 775 nm is demonstrated. Using a continuous-wave laser and a femtosecond pulse laser, not only the second but also the third and fourth harmonics in the visible wavelength range are observed due to higher-order phase-matching. In addition to the chip-demonstrators mentioned above, this work describes the fundamentals and physics of chip-integrated free-space sections using graded-index lenses, called the micro-optical bench. The fundamentals of this work are easily applicable to the integration of other free-space materials, enabling a multitude of new applications normally not feasible in integrated photonics. Thus, this work enables a bridge between optical bench experiments and integrated optics.

List of abbreviations

- AR *Anti reflection*
BBO *Beta-barium borate*
BIG *Bismuth-doped rare earth iron garnets*
DBR *Distributed Bragg-reflector*
DFB *Distributed feedback*
DWDM *Dense wavelength division multiplexing*
EAM *Electro-absorption modulator*
EDFA *Erbium-doped fiber amplifier*
GRIN *Graded index*
HR *High reflection*
HWP *Half-wave plate*
IC *Integrated circuit*
IL *Insertion loss*
InP *Indium phosphide*
KTP *Potassium titanyl phosphate*
LN *Lithium niobate, Lithium niobate*
LPE *Liquid phase epitaxy*
MEMS *Micro-electromechanical system*
MFD *Mode field diameter*
MMI *Multimode interference coupler*
MO *Magneto-optic*
MRR *Microring resonator*
MZI *Mach-Zehnder interferometer*
NA *Numerical aperture*
NRPS *Nonreciprocal phase shift*
NRZ *Non-return-to-zero*
OLT *Optical line termination*
ONU *Optical network units*
ORL *Optical return loss*
OSA *Optical spectrum analyzer*
PBS *Polarization beam splitter*
PER *Polarization extinction ratio*
PIC *Photonic integrated circuit*
ppLN *Periodically poled lithium niobate*
QPM *Quasi phase matching*
SAM *Saturable absorber*
SFG *Sum frequency generation*
SHG *Second-harmonic generation*
SiN *Silicon nitride*
SiP *Silicon photonics*
SMF *Standard single-mode fiber*
SNR *Signal-to-noise ratio*
SPDC *Spontaneous parametric down conversion*
TE *transverse electric*
TFF *Thin-film filter*
TGG *Terbium gallium garnet*
TM *transverse mlectric*

YIG *Yttrium iron garnet*
YOFC *Yangtze Optical Fibre and Cable*

Contents

I. INTRODUCTION.....	9
II. FUNDAMENTALS.....	12
A. Integrated Photonics and the PolyBoard platform.....	12
B. Theory of on-chip free-space sections	15
1. Gaussian beams	15
2. Graded-index optics	18
3. Transfer matrix analysis for Gaussian beam transmission in GRIN lenses	22
C. Nonreciprocal elements.....	24
1. Theory of optical isolators and circulators	25
2. Faraday effect and free-space isolators	27
3. Optical isolators and circulators in integrated photonics	29
4. Isolator and circulator designs in this work.....	30
D. Nonlinear elements.....	35
1. Nonlinear polarization density and nonlinear wave equation	35
2. Second-harmonic generation	36
3. Boyd-Kleinman condition	37
4. Phase-matching with periodic poling	39
5. Materials for second-harmonic generation.....	41
III. SIMULATION.....	43
A. Optical modes in polymer waveguides	43
B. Simulation of on-chip free-space sections	43
IV. FABRICATION.....	49
A. The PolyBoard.....	49
1. Waveguide fabrication	50
2. U-groove fabrication and GRIN lens alignment.....	50
3. Additional optical functionalities.....	51
B. GRIN lens fabrication.....	54
C. Preparation of nonreciprocal and nonlinear materials	56
1. Nonreciprocal elements	56
2. Nonlinear elements	57
V. RESULTS.....	58
A. On-chip free-space sections	58
1. Glue-filled free-space sections	58
2. Fiber-coupled free-space sections.....	60
3. Resonant cavity design	62
B. Integrated optical isolator	65
1. Stand-alone isolator	65

2.	Isolator integration with a tunable DBR laser	69
3.	Integrated optical isolators at other wavelengths	73
C.	Integrated optical circulator	74
1.	Polarization-based circulator.....	74
2.	Phase shift based optical circulator.....	77
3.	Comparison between both circulator designs.....	80
D.	Integrated second-harmonic generation	82
1.	Overview.....	82
2.	Characterization with a continuous wave laser	82
3.	Characterization with a pulsed laser	84
4.	Discussion	85
VI. CONCLUSION		88
APPENDIX		90
1.	Sellmeier equation for Mg:O doped ppLN	90
2.	Fabry-Pérot resonator and the Airy function	90
3.	Measurements on thermo-optic components	91
4.	Transparency of rare-earth-doped iron garnets	91
5.	Measurements on PBS test structures	92
6.	Measurements on Mach-Zehnder-interferometric test structures	93
VII. REFERENCES		95

I. Introduction

With the demonstration of the first working transistors by Bardeen, Brattain, and Shockley in 1948 [1, 2] and the development of semiconductor integrated circuits (IC) in the late 1950s and early 1960s by Robert Noyce and Jack Kilby [3, 4], an unprecedented leap in technology development started. Technology nodes reduced from 10 µm in the early 1970s to 5 nm in the late 2010s, which lead to a doubling of IC transistor density every two years described by Moor's law [5]. These advances in integration density and thus computing power, combined with the accompanied cost reduction, led to a widespread consumer availability of computers and smartphones. Together with the commercialization of the internet in the 80s and 90s [6], and increased connectivity between computational devices, this also led to the doubling of communication traffic every two years, known as Edholm's law in reference to Moore's law [7]. The foundation to support the exponential growth of Edholm's law was laid by the work of Charles K. Kao in the 1960s, who promoted the use of high purity silica fibers at 1550 nm for long-distance communication [8] and the development of the first laser in 1960 [9]. Today, optical fibers form the backbone of the consumer IP traffic, estimated to exceed $3 \cdot 10^{21}$ bit/s per year by the end of 2021, and connecting almost 25 billion devices [10]. With standard single-mode fibers (SMFs) providing a theoretical spectral efficiency of a few bit/s/Hz or a few hundred Tbit/s, according to Shannon's information theory [11], at least as of today, the bottleneck to keep up with the increasing traffic is not the transport medium itself but the optical components to reach this limit.

The aforementioned shift from discrete circuits to ICs in electronics also arose in the advances of photonic integrated circuits (PICs) but with a delay of around 30 years compared to ICs [12]. Similar to the transistor, the first laser diodes proposed and developed in the 1960s and 1970s [13] were used as discrete light sources, followed by the first monolithic PICs comprising of a distributed feedback (DFB) laser and an electro-absorption modulator (EAM) in the 1980s [14]. Taking this as a starting point, an exponential growth in the integration density of components and data transmission rates started to supply the similarly growing demand for transmission bandwidth. Especially with the requirement of high capacity links not only in long-haul communication spanning up to 1000s of kilometers but also in metro area networks (10's -100's km) and even data centers (<10 km), the cost and size reduction met by PICs along with some unique building blocks are of increased importance for the telecommunication industry [15].

Unlike ICs, where 99% of all chips are fabricated using CMOS technology, and monolithic integration [16], various photonic integration platforms rely on different material compositions and integration techniques like heterogeneous and hybrid integration [17, 18]. All these photonic platforms have distinct strengths and weaknesses, meaning there is not one material system and integration approach covering every application. Instead the integration platform is often chosen depending on requirements, applications, and the available components of one platform. Even though there is an increasing trend towards on-chip integration, a few optical components are especially challenging to realize in PICs. Two such components are optical isolators and circulators. Optical isolators are components that allow light transmission in forward direction but block all backward propagating light. They are widely used to protect lasers from unwanted optical feedback that might distort stable operation or even cause a coherence collapse of the device. Optical circulators are multiport devices that transmit light from one port to the next, while also optically isolating the previous port. Circulators are useful whenever optical fibers, or in general optical paths, are used bidirectional, for example in sensing applications like optical coherence tomography and fiber Bragg grating interrogators or in telecommunications for dispersion compensators with chirped Bragg gratings [19–21]. Today, the development of integrated isolators and circulators is still a field of active research, and there are no commercially available integrated isolators and circulators in

Introduction

integrated optics. This implies that if an isolator or circulator is necessary for an application, it must rely on additional free-space optics and not only the PIC itself.

The fundamental requirement for optical isolators and circulators to work is that they must break the Lorentz reciprocity, thus they are often referred to as nonreciprocal elements. In optics, Lorentz reciprocity states that the scattering amplitude B from a forward propagating incident electromagnetic field A is equal to the scattering amplitude A from a backward propagating incident electromagnetic wave with the amplitude B [22]. In other words, it is possible to reverse any reciprocal optical system or interchange the input and output. For example, a common misconception is that materials like one-way mirrors, as used in surveillance rooms, seem to break reciprocity, when in fact they only work for environments with a strong brightness contrast. The materials most commonly used in optics that truly break reciprocity are magneto-optic elements. In free-space optics, these can be used as bulk crystals, so-called Faraday rotators that induce a nonreciprocal polarization rotation, to build optical isolators. This approach yields components with good performance in terms of insertion loss and optical isolation. However, the integration of magneto-optic materials in integrated circuits is challenging and even though demonstrated many times, suffers from relatively high loss and optical isolation that does not necessarily work for arbitrary polarizations [23–28]. Furthermore, while the standalone demonstration of a working isolator is already difficult, the co-integration with other optical components like lasers has been demonstrated only a few times with very limited performance so far [29].

This work demonstrates the integration of an isolator and circulator in a polymer photonic integration platform, the PolyBoard. Since free-space isolators and circulators based on bulk magneto-optic components perform significantly better than current integrated approaches in terms of insertion loss and optical isolation, the proposal is to combine integrated waveguide and free-space optics on a single chip. This is achieved by implementing on-chip free-space sections into deeply etched trenches inside the polymer that are accessed with waveguides. To reduce the beam divergence caused by the waveguide to free-space interfaces, graded-index (GRIN) lenses are used to connect and couple waveguides to the free-space section. Thus, the GRIN lenses create collimated on-chip free-space sections with low optical loss to insert bulk elements. Within this work, a theoretical model that describes the underlying physics of waveguide coupled free-space sections based on Gaussian beam propagation is derived. Built on this model, three different devices relying on the integration of nonreciprocal elements are demonstrated. The first one is an integrated isolator characterized as a stand-alone device and co-integrated with a tunable distributed Bragg-reflector (DBR) laser, demonstrating the first co-integration of a DBR laser and an isolator in a PIC. Furthermore, two integrated circulators based on a nonreciprocal polarization rotation and a nonreciprocal phase shift are proposed, fabricated and characterized. Both approaches can be used as circulators and also operate as latching switches, defined as a switch that requires energy only during active switching and maintains its switch configuration otherwise.

The free-space section described above can be used for the integration of various bulk materials that offer additional functionalities normally not accessible by the polymer integration platform. Besides nonreciprocal elements, another group of functional materials for several applications are nonlinear crystals. One application example for nonlinear crystals is frequency conversion like second-harmonic generation (SHG), which creates a photon with twice the frequency from two degenerate incident photons. Based on the theory of SHG for Gaussian beams from Boyd and Kleinman [30], the second part of this work demonstrates SHG in the PolyBoard, by integrating a periodically poled lithium niobate (ppLN) bulk crystal inside the aforementioned free-space section.

Nonreciprocity and nonlinearity have different applications, but the underlying physics of both are described by interactions between light and matter that follow similar mathematical concepts

Introduction

described by Maxwell's equations. Moreover, the integration concept based on on-chip free-space sections is identical, therefore this work is not divided into nonreciprocity and nonlinearity, but follows a structure of shared chapters on both aspects. In chapter II, the fundamental concepts and physics behind the realization of on-chip free-space sections, and the physics behind nonreciprocal and nonlinear elements will be outlined, along with the concepts of the integrated circuits to be fabricated and characterized. This chapter is followed by simulations of the polymer waveguides and the free-space section in chapter III to achieve ideal coupling. Fabrication of the polymer integrated circuits, the GRIN lenses, and the preparation of nonreciprocal and nonlinear elements is covered in chapter II.C.3. The characterization and results of all fabricated components are then described in chapter V.

II. Fundamentals

The results of this work are based on the PolyBoard, a hybrid photonic integration platform developed at the Fraunhofer Heinrich Hertz Institute, and this work aims to demonstrate the integration of nonreciprocal and nonlinear elements into the platform. There are numerous different technology platforms available in integrated photonics, each with its distinct advantages and disadvantages. The following section, II.A, gives a brief overview of different integration platforms and some of their various strengths and weaknesses. Furthermore, the PolyBoard is introduced and the unique approach of on-chip free-space sections for the integration of nonreciprocal and nonlinear elements is discussed. In II.B, a theoretical model for integrated free-space sections, based on the propagation of Gaussian beams in free-space and graded-index lenses is derived. Section II.C will derive a formal definition of optical isolators and circulators and describe the differences between classical free-space isolators and recent developments of integrated isolators and circulators. One design for an integrated isolator and two designs for integrated circulators in the PolyBoard are proposed based on these findings. Besides integrated isolators and circulators, second-harmonic generation in the PolyBoard is demonstrated within this work. In the last section of this chapter, the fundamentals of second-harmonic generation based on a plane wave model and focused Gaussian beams in nonlinear crystals are described. Furthermore, a second-harmonic source in the PolyBoard is proposed with the goal to maximize its conversion efficiency.

A. Integrated Photonics and the PolyBoard platform

In contrast to classical free-space optics that uses lenses, mirrors or filters to guide and manipulate the light, integrated photonics utilizes optical waveguides that guide the light and interconnect different optical functionalities. Like integrated electronics, this offers miniaturization of optical components and a potential cost reduction compared to free-space optics. Besides waveguides and waveguide bends, essential integrated elements include lasers and photo detectors for generating and detecting light and components for splitters, polarization control, optical isolation, switching, and modulation [31]. For the fabrication of most of these components, the same lithographic tools utilized in microelectronics are used, even though the material compositions of PICs might be different. Four of the most prominent material systems for integrated circuits include indium phosphide (InP), silicon photonics (SiP), silicon nitride (SiN), and lithium niobate (LN). With efficient lasers, fast photo detectors, and modulators, InP is the most utilized platform for applications in telecom and datacom, working in the infrared from 1.3 μm to 1.6 μm [32]. SiP enables the usage of established silicon semiconductor manufacturing processes and the co-integration of electronics and optics with standard CMOS fabrication technologies for medium and large-scale integration. However, a significant drawback is the lack of a direct band gap in silicon that makes the development of on-chip light sources challenging [33]. By far the lowest propagation loss exhibit SiN PICs, enabling e.g. the integration of high-quality microring resonators for low linewidth lasers via the hybrid integration of semiconductor light sources [34]. Another advantage of SiN is the wide transparency ranging from 405 nm up into the infrared [35]. Lithium niobate offers a high nonlinear coefficient that makes it suitable for nonlinear optics, e.g. nonlinear frequency conversions like SHG [36] or spontaneous parametric down-conversion (SPDC) used in quantum optics [37]. Still, it is also often used for electro-optic modulators [38].

All these platforms have distinct strengths and weaknesses and thus different optical applications that they target. This is also attributed to the fact that not every optical component can be fabricated in every material system. A prime example being the already mentioned lack of a native laser in SiP. Other components that are not yet fully developed up to commercialization in any of these material systems are nonreciprocal elements like optical isolators and circulators. Even

though they are widely available as optical components for free-space optics, their integration is still a field of active research to reach the performance standards set by their bulk counterparts. A more thorough overview about different isolators and circulators in integrated photonics is given in II.C.4.

The results of this work are based on the PolyBoard, a polymer hybrid integration platform developed at Fraunhofer HHI. Like SiN photonic integration platforms and in contrast to the aforementioned monolithic integration platforms, e.g. InP, it follows a hybrid integration approach based on embedded polymer waveguides. Similar to other platforms, the fabrication is based on photolithographic processes, but instead of epitaxial growth, spin coating is used for layer deposition, which makes it potentially much cheaper than semiconductor-based platforms. Applications range from classical telecommunications to sensing and emerging fields like quantum technologies. Early developed components in telecommunication include polymer-based 90°hybrid 100 Gbit/s receivers [39], dense wavelength division multiplexing (DWDM) components like 40 channel arrayed waveguide gratings for optical line termination (OLT) [40], and tunable laser transmitters for optical network units (ONUs) [41]. All these components are based on a polymer motherboard with embedded waveguides. Passive waveguide components include arrayed waveguide gratings, waveguide-inscribed Bragg-gratings as well as power splitters like multimode interference couplers (MMIs) or Y-branch couplers. The average propagation loss for the waveguides at 1550 nm is 0.7 dB/cm that originates mostly from the polymers' material absorption. Heating the waveguides with buried electrodes allows the fabrication of components like switches, phase shifters, or tunable Bragg-gratings due to a high thermo-optic coefficient of $-10^{-4}/K$ [42]. As additional active elements, InP components like gain elements or laser diodes can be coupled directly to the polymer waveguides. On the receiving end, InP photo diodes are coupled either directly to the polymer waveguides, or used as bottom illuminated photo diodes integrated via 45° mirrors. Polarization manipulation is done with thin-film filters (TFFs) that are inserted into the light path via etched slots, enabling half-wave plates (HWPs) or polarization beam splitters (PBSs) and combiners. In combination, these components offer a set of building blocks to fabricate PICs for different applications. One example is a tunable distributed Bragg reflector laser that comprises an InP gain element, a phase shifter, and a tunable Bragg grating. Figure II-1 depicts a sketch of all standard elements of the PolyBoard.

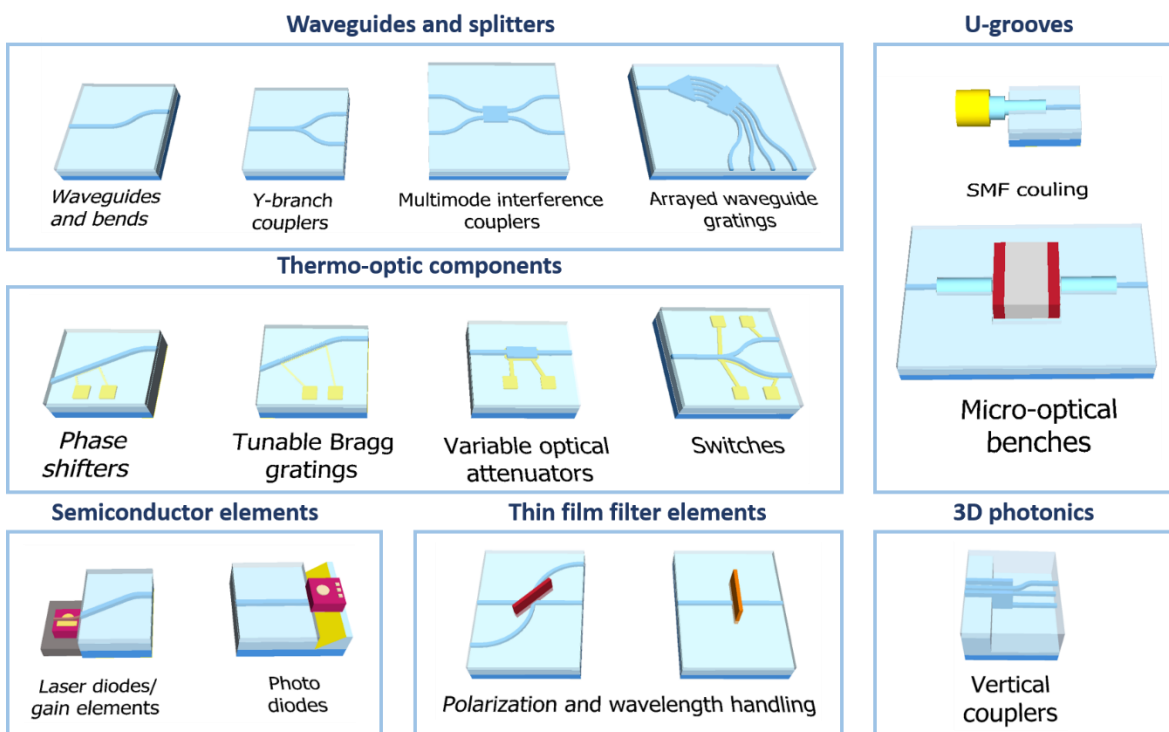


Figure II-1: Available standard building blocks of the polymer-based hybrid integration platform PolyBoard.

Besides the previously introduced components, additional building blocks of the PolyBoard are so-called U-grooves for fiber-to-chip coupling. Like the slots for thin-film filters, these are precisely etched slots such that the bottom surface of the U-groove can be used to align the fiber core with the polymer waveguide passively. The width of the U-groove is designed to be a little smaller than the 125 µm cladding diameter of the fiber, and the fiber can be clamped in the slightly flexible polymer.

Within this work, these U-grooves are used to create on-chip free-space sections to insert optical bulk materials with the help of two collimating GRIN lenses. Since it copies the concept of an optical bench with its free-space beam sections where materials can simply be inserted into the optical path, this approach is generally referred to as the micro-optical bench. While the length of optical materials inserted into thin-film filter slots is limited to a few microns, the micro-optical bench enables the insertion of materials up to a few millimeters in length. It consists of an input GRIN lens coupled to the polymer waveguide via a U-groove, a free-space section for the insertion of optical crystals, and an output GRIN lens coupled to the output waveguide. The first GRIN lens enlarges the beam diameter of the waveguide/GRIN lens interface. It creates a collimated beam with low beam divergence that propagates through the free-space section and the second GRIN lens focuses the light back into the output waveguide. Figure II-2 depicts a schematic of the on-chip free-space section used to integrate nonlinear or nonreciprocal optical crystals. Within this work, the insertion of nonreciprocal and nonlinear materials, the first for optical isolators and circulators and the latter for second-harmonic generation, is demonstrated.

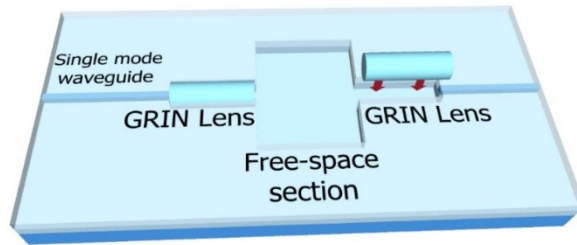


Figure II-2: Schematic layout of the micro-optical bench. A GRIN lens is coupled to a polymer waveguide to create a free-space with low beam divergence. A second GRIN lens couples the light back into the polymer waveguide. In between the GRIN lenses is a free-space section that enables the insertion of functional materials.

Prior to this work, first experiments with etalons for wavelength locking were already carried out with commercially available GRIN lenses [43, 44]. However, due to the high costs of the required GRIN lenses with a diameter of 125 µm, a GRIN lens fabrication process for cheap mass production of GRIN lenses was also developed within the scope of this work. The following section describes the theory of GRIN lenses and the physics involved to derive a model for the description of the free-space section.

B. Theory of on-chip free-space sections

The key idea for integrating nonreciprocal and nonlinear media into the PolyBoard is enabled by an on-chip free-space section to insert bulk crystals, as described in the previous section. This section aims to derive a simple model for the simulation of light propagating inside the free-space section and the physics involved.

Both, the optical mode inside the polymer waveguides and the free-space section, and the GRIN lenses that form it can be described by propagating Gaussian modes and beams. This section will introduce Gaussian beams as a solution for the wave equation, describe light propagation inside a GRIN lens based on Fermat's principle and combine both in a simple formalism for beam propagation with ABCD matrices. These fundamentals form the tools used for the simulations to determine required GRIN lens lengths and the coupling efficiencies of different free-space sections in chapter III. The derivation of the Gaussian beam as a solution to the paraxial Helmholtz equation derived from Maxwell's equation is mainly based on chapters 1, 3, and 5 from Saleh and Teich's "Fundamentals of Photonics", as is the ray theory of graded-index lenses in subsection II.B.2 [45].

1. Gaussian beams

Wave equation and the Helmholtz equation

The wave equation describes the propagation of an electromagnetic wave in a medium or vacuum. This second-order partial differential equation can be derived from the Maxwell equations. These equations in a medium with no charges or currents can be written as

$$\vec{\nabla} \vec{E} = 0 \quad (\text{II-1})$$

$$\vec{\nabla} \vec{B} = 0 \quad (\text{II-2})$$

$$\vec{\nabla} \times \vec{E} = -\frac{\delta \vec{B}}{\delta t} \quad (\text{II-3})$$

$$\vec{\nabla} \times \vec{H} = \frac{\delta \vec{D}}{\delta t}, \quad (\text{II-4})$$

where \vec{E} and \vec{H} are the electric and magnetic field and \vec{D} and \vec{B} the electric and magnetic flux density. ϵ_0 and μ_0 are the vacuum permittivity and permeability that describe the relationship between the electromagnetic fields and the flux densities:

$$\vec{D} = \epsilon_0 \vec{E} + \vec{P} \quad (\text{II-5})$$

$$\vec{B} = \mu_0 \vec{H} + \vec{M}, \quad (\text{II-6})$$

with \vec{P} and \vec{M} being the polarization and magnetization density. The polarization density \vec{P} will play an essential role in the description of nonreciprocal elements in section C and nonlinear optics for second-harmonic generation in section D of this chapter, but for now, it is assumed to be simply proportional to the electrical field such that $\vec{D} = \epsilon_0(1 + \chi^{(1)})\vec{E} = \epsilon\vec{E}$, where $\chi^{(1)}$ is the first order electric susceptibility and ϵ the electric permittivity. The magnetization density \vec{M} is assumed to be zero for all considerations in this work.

Taking the curl of equation (II-3)and (II-4), simplifying with the vector identity

$$\nabla \times (\nabla \times \vec{E}) = \nabla(\nabla \cdot \vec{E}) - \nabla^2 \vec{E},$$

and the zero divergence theorem from equation (II-1) and (II-2) of the electric field and magnetic flux, Maxwell's equations can be rewritten as

$$\frac{1}{c^2} \frac{\delta^2 \vec{E}}{\delta^2 t} - \vec{\nabla}^2 \vec{E} = 0 \quad (\text{II-7})$$

$$\frac{1}{c^2} \frac{\delta^2 \vec{B}}{\delta^2 t} - \vec{\nabla}^2 \vec{B} = 0, \quad (\text{II-8})$$

known as the wave equation for a linear, nondispersive homogeneous and isotropic medium, where $c = 1/\sqrt{\epsilon\mu_0}$ is the speed of light in the medium. The following solution of the wave equation is derived for the electrical field. However, since the wave equation for the electric and magnetic field are written equivalently, and both fields are connected via Maxwell's equation, the solution also holds true for the magnetic field. A solution of the wave equation can be derived by a time-harmonic wave function of the form

$$\vec{E}(\vec{r}, t) = \vec{E}(\vec{r}) e^{i\phi(\vec{r})} e^{i\omega t}. \quad (\text{II-9})$$

Substituting this into the wave equation (II-7) yields the Helmholtz equation

$$\left(\vec{\nabla}^2 + \frac{\omega^2}{c^2} \right) \vec{E}(\vec{r}) e^{i\phi(\vec{r})} = 0. \quad (\text{II-10})$$

If the envelope of equation (II-9) varies only slowly within its propagation direction z , one can assume a plane wave character of $\vec{E}(\vec{r}) = A(\vec{r}) e^{-ikz}$ that leads to the paraxial Helmholtz equation or slowly varying envelope approximation:

$$\left(\frac{\delta^2}{\delta x^2} + \frac{\delta^2}{\delta y^2}\right)A - i2k \frac{\delta A}{\delta z} = 0 \quad (\text{II-11})$$

For this assumption to hold, the change of A in propagation direction must be small within the distance of one wavelength.

Gaussian beams

A solution to the Helmholtz equation (II-10) with the paraxial wave approximation in equation (II-11) is a Gaussian beam, where the complex amplitude $\vec{E}(\vec{r}_{x,y}, z)$ can be written as

$$\vec{E}(\vec{r}_{x,y}, z) = \vec{E}_0 \frac{\omega_0}{\omega(z)} e^{-\frac{r^2}{\omega(z)^2}} e^{(-i(kz + \frac{r^2}{2R(z)} - \psi(z))}. \quad (\text{II-12})$$

Here

- \vec{E}_0 is the electrical field vector at the origin,
- $\omega_0 = \omega(0)$ is the waist radius at the origin,
- $\omega(z)$ the waist radius at which the field amplitude is equal to $1/e$ of their axial value (similarly equal to $1/e^2$ for the intensity) defined by

$$\omega(z) = \omega_0 \sqrt{1 + \left(\frac{z}{z_R}\right)^2}, \quad (\text{II-13})$$

- with the wavelength (λ) dependent Rayleigh length, where the cross-sectional area of the beam is doubled:

$$z_R = \frac{\pi \omega_0^2 n}{\lambda} \quad (\text{II-14})$$

- $R(z)$ is the radius of curvature

$$R(z) = z(1 + (\frac{z_R}{z})^2) \quad (\text{II-15})$$

- and $\psi(z)$ is the Gouy phase

$$\psi(z) = \arctan\left(\frac{z}{z_R}\right) \quad (\text{II-16})$$

Another useful value is the beam divergence θ (in radians) defined by

$$\theta = \frac{\lambda}{\pi \omega_0 n} \quad (\text{II-17})$$

A similar expression can be derived for the Gaussian beam intensity with the relation $I(\vec{r}_{x,y}, z) = \frac{c_0 n \epsilon_0}{2} |\vec{E}(\vec{r}_{x,y}, z)|^2$:

$$I(\vec{r}_{x,y}, z) = I_0 \left(\frac{\omega_0}{\omega(z)}\right)^2 e^{-\frac{r^2}{\omega(z)^2}}. \quad (\text{II-18})$$

A Gaussian beam has its maximum intensity at its waist $z = 0$ and the intensity drops monotonically with increasing position. From equation (II-12) or (II-18) and its substitutes follows that the complete Gaussian beam is defined by only one parameter, e.g. the waist ω_0 , for a given λ and n . The beam width of a Gaussian beam is depicted in Figure II-3.

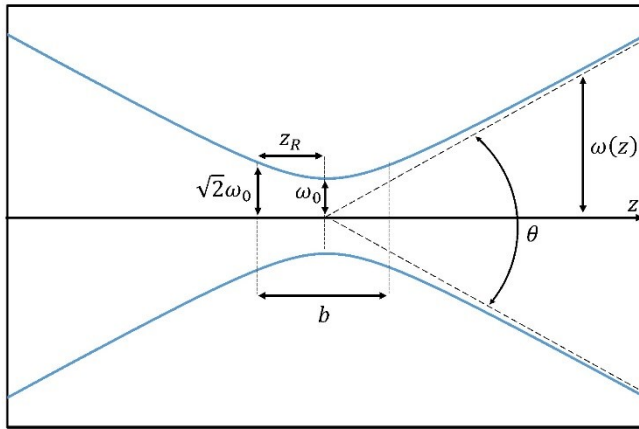


Figure II-3: Width $\omega(z)$ of a Gaussian beam and highlighted waist ω_0 , beam divergence θ , Rayleigh range z_R and the confocal parameter b defined as twice the rayleigh range.

Equation (II-12) and (II-18) describe the fundamental (TEM_{00}) Gaussian mode. There exist higher order modes of Gaussian beams, but they are not of interest for this work since the waveguides of the PolyBoards are single-mode, which in return results only in the excitation of TEM_{00} modes in the GRIN lenses and subsequently the free-space section. Together with ABCD matrices that will be introduced in section 3 of this subchapter, Gaussian beams form a handy tool to describe the complete light propagation inside the free-space section. This includes the coupling efficiency to the waveguides, the optical beam formed inside the free-space section, and the required parameters of the GRIN lenses for optical beam forming.

2. Graded-index optics

As long as Gaussian beams are not confined, e.g. inside a waveguide as a Gaussian mode, they have an intrinsic beam divergence proportional to the wavelength and inversely proportional to the waist of the Gaussian beam (see equation (II-17)) as depicted in Figure II-1. For example, polymer waveguides that support a Gaussian mode with a waist of $2\text{ }\mu\text{m}$ would have a beam divergence of 14° and a Rayleigh range of $8\text{ }\mu\text{m}$ when the waveguide excites into air. Meaning that the mode field area doubles in size every $8\text{ }\mu\text{m}$. This beam divergence can be significantly reduced by expanding the beam diameter. A Gaussian waist of $40\text{ }\mu\text{m}$ results in a Rayleigh range of $3243\text{ }\mu\text{m}$, roughly 400 times more than for a simple waveguide facet, and a beam divergence of 0.7° . Thus, for the integration of nonreciprocal or nonlinear bulk crystals into the polymer circuit, the optical modes of the waveguides must be expanded and collimated to reduce the beam divergence and loss inside the free-space elements. One way to expand the beam is to use two optical lenses with their focal point at the free-space section's input and output waveguide facet, as depicted earlier in Figure II-2. Well-suited lenses for this implementation are graded-index lenses or GRIN lenses. In contrast to conventional lenses, GRIN lenses are optical lenses that do not get their focusing ability from their geometrical shape and surface refraction but from a gradual variation of the refractive index inside the lens. Thus, optical rays inside a GRIN lens follow curved trajectories and not straight lines as in conventional lenses. The required variation of the refractive index can be achieved by material doping of silica glass with dopants like Ge/F. The advantage of GRIN lenses over conventional lenses for the waveguide coupling is their flat facets, making the alignment much easier and allowing waveguide butt-coupling inside U-grooves. Furthermore, they do not require an air interface to work, meaning they can be glued into place with index-matching glue without the need for any

anti-reflection (AR) coatings. This section describes the fundamental principles of light transmission in GRIN lenses based on ray optics and how they can be used for beam tailoring, and general characteristics important to GRIN lenses.

Fermat's Principle and the ray equation

Fermat's principle states that a ray of light that travels between two points always takes the path that is stationary concerning slight variations. This can be written mathematically as

$$\delta S = \delta \int_A^B n(\vec{r}) ds = 0 \quad (\text{II-19})$$

Here, A and B are the starting and end point of the trajectory, $n(\vec{r})$ the refractive index variation of the GRIN material, ds a differential path length across the optical path and δS a first-order change in the optical path length S . In other words, Fermat's principle states that any small change to the optical path between A and B must result only in a second-order change of the optical path length and not a first-order change. This formulation is similar to the first-order derivative of a function which indicates a local extremum. In the more popular strong formulation, Fermat's states that light takes the path of least time between two points, indicating that the second-order change in the path length also has to be positive.

If the trajectory along its path from A to B inside the GRIN lens is described by the vector $\vec{r}(s)$, including the three spatial components, then $\vec{r}(s)$ is required to satisfy the ray equation resulting from Fermat's principle (Chapter 5 in [46]):

$$\frac{d}{ds} \left(n(\vec{r}) \frac{d\vec{r}}{ds} \right) = \nabla n \quad (\text{II-20})$$

Similar to the wave equation and the paraxial wave equation used for the derivation of Gaussian beams in section 1 of this subchapter, there is a paraxial ray equation under the assumption that the ray's trajectory is nearly parallel to the propagation axis z and $ds \approx dz$ that can be written as

$$\frac{d}{dz} \left(n \frac{dx}{dz} \right) = \frac{\partial n}{\partial x}, \quad (\text{II-21})$$

$$\frac{d}{dz} \left(n \frac{dy}{dz} \right) = \frac{\partial n}{\partial y}, \quad (\text{II-22})$$

making it much easier to solve.

Light propagation in GRIN lenses

The GRIN lenses used in this work have a decreasing refractive index profile that can be approximated with

$$n = \sqrt{n_{core}^2(1 - \alpha^2(x^2 + y^2))} \approx n_{core}(1 - \alpha^2(x^2 + y^2)) \quad (\text{II-23})$$

inside the GRIN lens core for $\alpha^2(x^2 + y^2) \ll 1$, where α is the gradient constant based on the dopant of the lens. Equation (II-23) corresponds to an approximately parabolic refractive index profile as depicted in Figure II-4, where the numerical aperture NA defines the steepness of the parabolic decrease and refractive index difference between core and cladding:

$$NA = \sqrt{n_{core}^2 - n_{cladding}^2}. \quad (\text{II-24})$$

Here, n_{core} is the peak refractive index in the center of the GRIN lens and $n_{cladding}$ the refractive index of the cladding, similar to the definition of the numerical aperture of conventional fibers. In case of a parabolic refractive index profile, the paraxial ray equations (II-21) and (II-22) can be written as

$$\frac{d^2x}{dz^2} = -\alpha^2 x, \quad (\text{II-25})$$

$$\frac{d^2y}{dz^2} = -\alpha^2 y, \quad (\text{II-26}),$$

with the ray solutions

$$x(z) = \frac{\theta_{x0}}{\alpha} \sin(\alpha z) + x_0 \cos(\alpha z) \quad (\text{II-27})$$

$$y(z) = \frac{\theta_{y0}}{\alpha} \sin(\alpha z) + y_0 \cos(\alpha z) \quad (\text{II-28})$$

inside the core. The general ray path inside the GRIN lens is given by a sinusoidal function that depends on the initial position (x_0, y_0) and angles $(\theta_{x0}, \theta_{y0})$ of the incident rays as depicted in Figure II-4. The beams oscillate with a period of $2\pi/\alpha$ around the center which is called the pitch of the GRIN lens. Even though all rays in Figure II-4 inside the GRIN material follow different trajectories, the optical path length is the same due to the decreasing refractive index for larger r . In multimode graded-index fibers this can be used to decrease modal dispersion compared to step-index fibers.

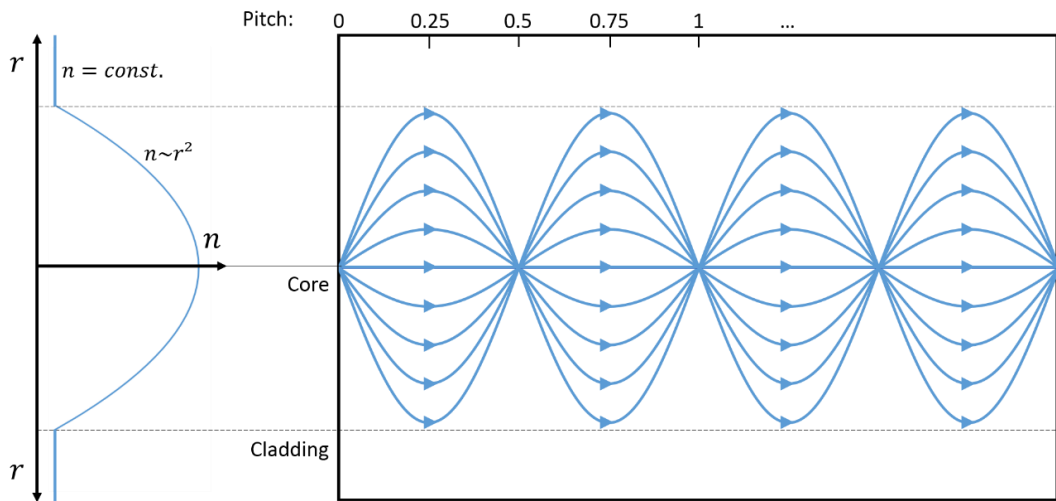


Figure II-4: Parabolic refractive index profile of a GRIN material (left) with the corresponding sinusoidal ray trace according to equations (II-27) and (II-28) and highlighted pitches.

Assuming a given set of input rays at the center of the GRIN lens, e.g. from a waveguide facet, it is possible to tailor the light rays at the output of the lens with the variation of the lens length, similar to conventional lenses. The pitch of the GRIN lens, defined as the number of full sinusoidal ray propagations inside the GRIN lens, defines the shape of the output beam after transmission of the GRIN lens. For a pitch < 0.25 , the GRIN lens creates a divergent set of output beams, while the beam is convergent for $0.25 < \text{pitch} < 0.5$. At a pitch of 0.25, the GRIN lens creates a collimated beam, and at 0.5, the output mirrors the input rays as depicted in Figure II-5.

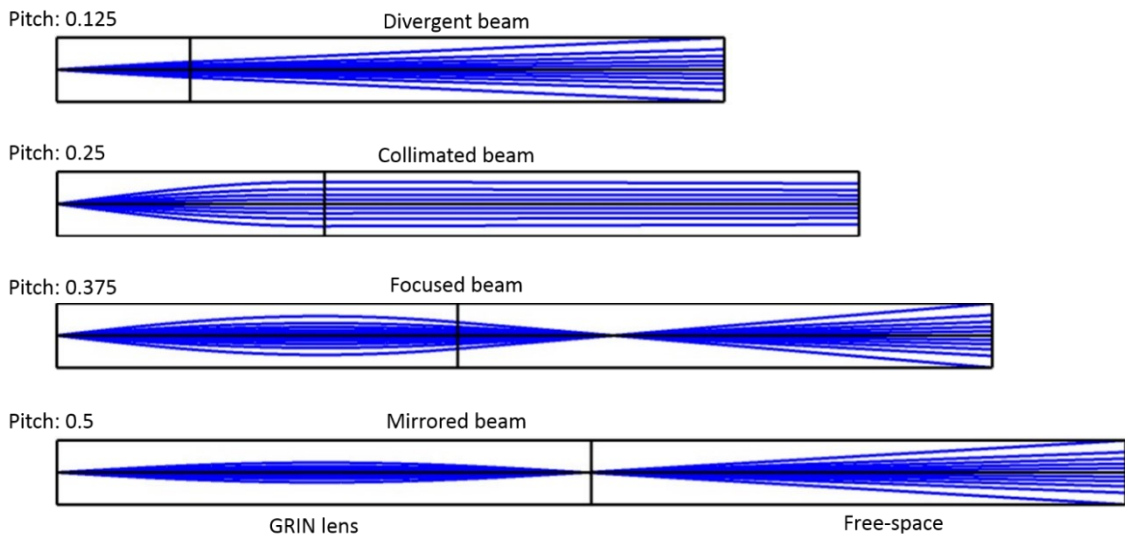


Figure II-5: Beam forming for differently pitched GRIN lenses that correspond to different lengths of the GRIN lenses based on ray optics.

From a practical point of view, it is convenient to calculate the length of the required GRIN lenses for a pitch of 0.25, as shown in Figure II-5. A pitch of 0.25 corresponds to a collimated beam with minimal beam divergence created from the divergent mode field of the waveguide/GRIN input interface. Depending on the waveguide geometry and the mode confinement of the PolyBoard, two types of GRIN lenses are fabricated from a commercially available graded-index fiber from Yangtze Optical Fibre and Cable (YOFC) with the fiber specifications and corresponding GRIN lens characteristics depicted in Table II-1:

Table II-1: Specifications of the graded-index fibers used for fabrication of GRIN lenses.

	High confinement GRIN lens	Low confinement GRIN lens
Numerical aperture	0.24	0.14
Core diameter	100 μm	105 μm
Cladding diameter	125 μm	125 μm
Core material composition	Ge/F doped silica glass	Ge/F doped silica glass
Cladding material composition	Pure silica	Pure silica
Gradient constant	0.0023 / μm	0.0013 / μm
0.25 pitch length	~495 μm	~830 μm
Maximum acceptance angle (from air)	14°	8°

It is noted that the solutions in this section are based on ray optics. While this is a reasonably accurate model for the light propagation in GRIN lenses, it does not consider any beam divergence inherent to Gaussian beams. It is also possible to solve the Helmholtz equation (equation (II-11)) for a varying refractive index $n(\vec{r})$ in order to calculate the optical modes that are guided within the GRIN lens and obtain a more accurate model of the free-space section. This can be done with an approximated approach based on quasi-plane waves traveling along the trajectory of optical rays, as shown in chapter 8 of [45]. However, the excitation of optical modes in the GRIN lenses is limited to the fundamental mode due to single-mode optical waveguides used in this work. Thus, the consideration of only ray optics inside the GRIN lenses provides an easy way to calculate the required lengths of GRIN lenses, and solutions of the Helmholtz equation do not offer additional

insights for this work. A more straightforward way to calculate not only the required lengths of the GRIN lenses but also the light propagation inside the free-space section, and the coupling efficiencies of the free-space section and the polymer waveguides are ABCD matrices for Gaussian beams to be introduced in the next section.

3. Transfer matrix analysis for Gaussian beam transmission in GRIN lenses

The previous section gave a general overview of the working principle of GRIN lenses based on ray optics. This approach already allows the calculation of required GRIN lens lengths to form different beams in the on-chip free-space section and explains the fundamental behavior of GRIN lenses. However, two things must be considered. As depicted in Figure II-5, a GRIN lens with a pitch of 0.25 creates a collimated parallel beam that stays collimated without any beam divergence due to the general properties of ray optics. Gaussian beams as a solution of the paraxial ray equation (II-20) on the other hand, have an inherent beam divergence inversely proportional to the beam waist (equation (II-17)). Even though optical beams created by the GRIN lenses are significantly larger than the optical mode field diameters (MFDs) of the polymer waveguides, with average beam diameters of approx. 80 μm , they are still relatively small. Thus, the beam divergence still plays a vital role in the maximum lengths of free-space sections that can be bridged. Secondly, the actual coupling efficiency from the waveguide modes into the propagating mode of the free-space section and back into the output waveguide must be estimated. One approach to calculate these is based on ray transfer (ABCD) matrices for Gaussian beams as described in [47].

ABCD matrices for Gaussian beams

ABCD matrices are a mathematical tool to track optical rays in a system. Like the paraxial wave and ray equation introduced in the previous sections, the paraxial approximation of ABCD matrices again requires all rays to propagate at small angles θ_i relative to the optical axis z . Each ray can be described by an offset r_i and the angle θ_i . An output ray $i + 1$ is related to the input ray i by

$$\begin{pmatrix} r_{i+1} \\ \theta_{i+1} \end{pmatrix} = \underbrace{\begin{pmatrix} A & B \\ C & D \end{pmatrix}}_S \begin{pmatrix} r_i \\ \theta_i \end{pmatrix}, \quad (\text{II-29}),$$

where the ABCD matrix S describes the i th optical element the light ray passes through. This concept can be expanded to Gaussian beams with the introduction of the complex beam parameter q_i that describes the Gaussian beam at a point along its propagation axis:

$$\frac{1}{q_i} = \frac{1}{R_i} - i \frac{\lambda}{\pi n \omega_i^2}, \quad (\text{II-30}),$$

where R_i is the radius of curvature and ω_i the radius of the beam. As mentioned in II.B.1, for a given λ and n only one parameter, e.g. the beam waist ω_0 is sufficient to describe a Gaussian beam. R_i depends on the distance z from the beam waist and the beam waist itself; thus it is possible to reconstruct the full Gaussian beam from the complex beam parameter. For a Gaussian beam parameter, the ABCD law can be written as

$$q_{i+1} = \frac{Aq_i + B}{Cq_i + D}. \quad (\text{II-31})$$

As shown in chapter 20 of [48], this expression can make use of the same ray matrices as equation (II-29). For example, the transmission in free-space is given by

$$\begin{pmatrix} A & B \\ C & D \end{pmatrix} = \begin{pmatrix} 1 & d \\ 0 & 1 \end{pmatrix}, \quad (\text{II-32})$$

with the transmission distance d . The ray matrix of a GRIN lens with length l and a parabolic refractive index profile as in equation (II-23) is described by

$$\begin{pmatrix} A & B \\ C & D \end{pmatrix} = \begin{pmatrix} \cos(\sqrt{2}\alpha l) & \frac{1}{\sqrt{2}\alpha n_0} \sin(\sqrt{2}\alpha l) \\ \sqrt{2}\alpha n_0 \sin(\sqrt{2}\alpha l) & \cos(\sqrt{2}\alpha l) \end{pmatrix} \quad (\text{II-33})$$

Subsequent substitution of these matrices into equation (II-31) allows calculating the optical modes inside the GRIN lenses, the free-space section, and thus the mode that will be coupled back into the waveguide after a free-space length of z_0 with a refractive index of n inside the free-space section. The model to calculate the radius of the optical mode ω_{GRIN2} (and R_{GRIN2}) that will be coupled back into the waveguide consists of an input beam waist ω_{WG0} (and $R_{WG0} = \infty$) that will be transferred through an input GRIN lens, a free-space section, and an output GRIN lens that couples the light back into the waveguide as depicted in Figure II-6.

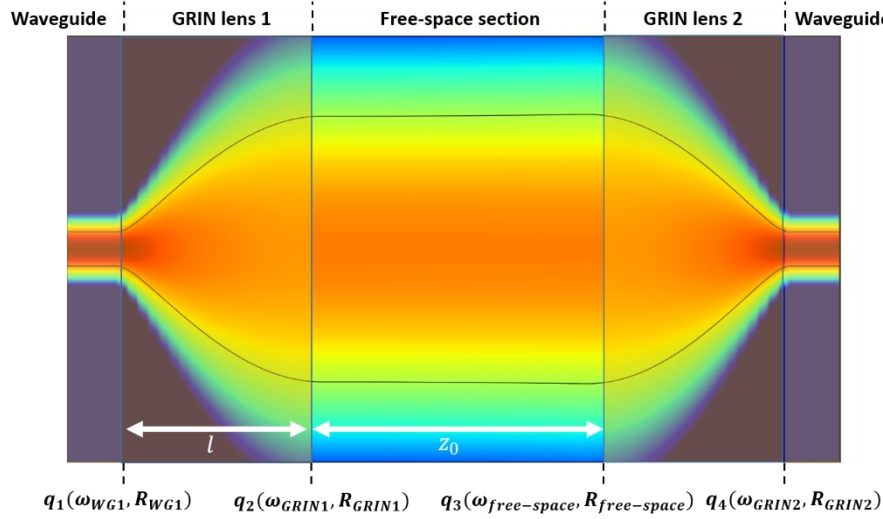


Figure II-6: Propagation model for ABCD matrices with marked positions of the complex beam parameters q_i at the different interfaces.

For GRIN lenses with a pitch of 0.25, the results after the different interfaces are [47]:

$$\omega_{GRIN1} = \frac{\lambda}{\sqrt{2}\pi\alpha n_0 n \omega_{WG1}} \quad (\text{II-34})$$

$$R_{GRIN1} = \infty \quad (\text{II-35})$$

$$\omega_{free-space} = \omega_{GRIN1} \left[1 + \left(\frac{\lambda z_0}{\pi n \omega_{GRIN1}^2} \right)^2 \right]^{1/2} \quad (\text{II-36})$$

$$R_{free-space} = z_0 \left[1 + \left(\frac{\pi n \omega_{GRIN1}^2}{\lambda z_0} \right)^2 \right]^{1/2} \quad (\text{II-37})$$

$$\omega_{GRIN2} = \frac{\lambda}{\sqrt{2}\pi\alpha n_0 n \omega_{GRIN1}} = \omega_{WG1} \quad (\text{II-38})$$

$$R_{GRIN2} = -\frac{1}{2n_0\alpha^2 z_0}. \quad (\text{II-39})$$

For ideal coupling, not only the beam diameter ω_{GRIN2} must match the input beam width ω_{WG1} , but also the radius of curvature should be equal or close to infinity. Whilst the first requirement is met for GRIN lenses with a pitch of 0.25, the second is not (cf. equation (III-39)). This is a result of the inherent divergence of Gaussian beams, such that only a free-space length of $z_0 = 0$ would

achieve perfect coupling. As this is clearly impractical, the pitch of the GRIN lenses must deviate from a pitch of 0.25 to obtain an ideal coupling efficiency for nonzero free-space lengths, as will be calculated later in chapter III.

The actual coupling efficiency η is calculated with an overlap integral for the incident electrical field E_{WG1} corresponding to the input mode of the waveguide and the optical mode resulting from the Gaussian beam E_{GRIN2} that can be calculated from ω_{GRIN2} and R_{GRIN2} [49]. The overlap integral can be calculated with

$$\eta = \frac{\left| \int_A E_{WG1} E_{GRIN2}^* dA \right|^2}{\int_A |E_{WG1}|^2 dA \int_A |E_{GRIN2}|^2 dA}. \quad (\text{II-40})$$

The nominator in this equation depicts the mode overlap, and the denominator is a normalization factor. The beam radius $\omega_{free-space}$ after transmission of the free-space section scales linearly with the free-space section length z_0 (equation (II-36)). For large z_0 , the beam radius $\omega_{free-space}$ becomes larger than the radius r_{GRIN} of the GRIN lens, which means that an increasing amount of power gets lost at the coupling interface between the free-space section and the second GRIN lens for an increasing z_0 . This can be taken into account with a pin hole transmission factor gained by integrating over the power within the radius, or aperture, of the GRIN lens

$$p_0 = 1 - e^{-\frac{2r_{GRIN}^2}{\omega_{free-space}^2}}, \quad (\text{II-41})$$

such that the total coupling efficiency becomes

$$\eta^* = p_0 \eta. \quad (\text{II-42})$$

For small free-space section lengths, this pinhole factor can be neglected since the transmitted Gaussian beam is smaller than the radius of the GRIN lens. However, at large free-space sections lengths, the beam divergence and p_0 become the dominant loss contribution. For this work, the radius r_{GRIN} is 62.5 μm .

The propagation of Gaussian beams with ABCD matrices for GRIN lenses and free-space that were introduced within this chapter forms an easy but effective tool to calculate mode overlap integrals that determine the coupling loss of on-chip free-space sections. Furthermore, they enable the calculation of different solutions for GRIN lens lengths beyond only collimating lenses. For example, the solutions for focusing lenses can be calculated as well, which play an essential role in second-harmonic generation to be introduced in II.D. Chapter III will use the considerations in this section and simulate on-chip free-space sections based on Gaussian beam transmission with concrete values for two different material systems and GRIN lens characteristics listed in Table II-1.

C. Nonreciprocal elements

One of the materials to be integrated with the on-chip free-space section described in the previous section are nonreciprocal elements, more specifically magneto-optic Faraday rotators required for optical isolators or circulators. Even though these are established components in free-space optics, the integration into PICs is challenging and still a field of active research with only a few demonstrators available. This section aims to give an overview about optical isolators and circulators, starting with a formal definition, the derivation of the Faraday effect, and an overview of state-of-the-art isolators and circulators in integrated photonics. At the end of the chapter, the concept of the integrated isolator and two different circulators developed within this work are described.

1. Theory of optical isolators and circulators

An optical isolator is a device that transmits light in one direction but blocks all light in the backward direction. Isolators are especially useful to protect lasers from unwanted optical feedback that might cause side modes in the resonator or even a coherence collapse. In more complex PICs, optical isolators can be used to block unwanted interactions or light routing between different components. The expanded version of the isolator is an optical circulator. A circulator comprises three or more ports, and instead of simply blocking the light in the backward direction, the light is routed from one port to the consecutive port. Since the initial port where the light was coupled in is always optically isolated in backward direction, an optical circulator also functions as an optical isolator. Circulators are of particular interest in fiber-based sensing systems, where the measurement requires a bidirectional measurement setup for measurement and detection, e.g. in optical coherence tomography or in fiber Bragg-grating based optical add-drop multiplexer or sensors [19, 20, 50].

Definition of an optical isolator and circulator

One way to find a general-purpose definition for optical isolators and circulators is based on scattering matrices that describe optical systems. Figure II-7 depicts the schematic of an optical isolator and circulator with incident powers P_{in}^i and the output powers P_{out}^i , such that the system is described by $\vec{P}_{out} = \tilde{S} \vec{P}_{in}$:

$$\vec{P}_{out} = \begin{pmatrix} S_{11} & S_{12} & S_{13} & \dots \\ S_{21} & S_{22} & S_{23} & \dots \\ S_{31} & S_{32} & S_{33} & \dots \\ \vdots & \vdots & \vdots & \ddots \end{pmatrix} \vec{P}_{in} \quad (\text{II-43})$$

Here, \tilde{S} is the scattering matrix with the coefficients s_{ij} that describe the power transfer from port j to port i .

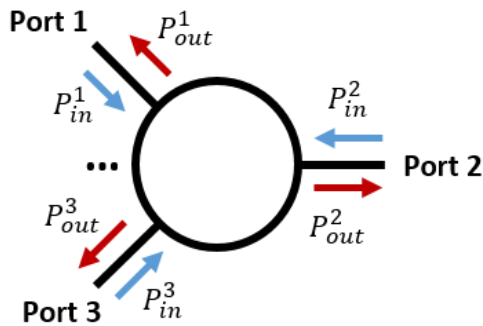


Figure II-7: Optical circuit with multiple ports and incident powers P_{in}^i and output powers P_{out}^i .

In the case of a perfect optical isolator or circulator, where all the power is transferred from one port to the consecutive port without any loss and infinite isolation, the transfer matrix can be written as

$$\vec{P}_{out} = \begin{pmatrix} 0 & 0 \\ 1 & 0 \end{pmatrix} \vec{P}_{in} \quad (\text{II-44})$$

for an optical isolator with two ports and for a circulator with four ports as

$$\vec{P}_{out} = \begin{pmatrix} 0 & 0 & 0 & 1 \\ 1 & 0 & 0 & 0 \\ 0 & 1 & 0 & 0 \\ 0 & 0 & 1 & 0 \end{pmatrix} \vec{P}_{in}. \quad (\text{II-45})$$

In a more general sense, taking loss and non-perfect isolation into account, optical isolators can be defined as components with an asymmetric scattering matrix, where $s_{ij} \neq s_{ji}$ is valid for at least one pair of coefficients, or $\tilde{S} \neq \tilde{S}^T$. The formal definition of an n -port optical circulator additionally requires all coefficients of the upper secondary diagonal to be larger than the coefficients of the lower secondary main diagonal or vice versa:

$$s_{i+1i} > s_{ii+1} \quad \wedge \quad s_{ii+1} > s_{i+1i} \quad (\text{II-46})$$

and optionally

$$s_{1n} > s_{n1} \quad \wedge \quad s_{n1} > s_{1n}, \quad (\text{II-47})$$

if the circulator also includes a connection between the first and the last port, which is usually not the case for optical circulators.

Lorentz reciprocity theorem

For a time-harmonic field, the third and fourth Maxwell equation from equation (II-3) and (II-4) are

$$\vec{\nabla} \times \vec{E} = -i\omega\mu\vec{H} \quad (\text{II-48})$$

$$\vec{\nabla} \times \vec{H} = -i\omega\epsilon\vec{E}, \quad (\text{II-49})$$

with two electromagnetic fields $\{\vec{E}^1, \vec{H}^1\}$ and $\{\vec{E}^2, \vec{H}^2\}$, originating from two different excitation states, both equations and can be written as

$$\vec{H}^2 \vec{\nabla} \times \vec{E}^1 + \vec{E}^2 \vec{\nabla} \times \vec{H}^1 = i\omega(\vec{E}^2 \epsilon \vec{E}^1 - \vec{H}^2 \mu \vec{H}^1) \quad (\text{II-50})$$

by dot multiplication of equation (II-48) and (II-49) for the excitation $\{\vec{E}^1, \vec{H}^1\}$ with \vec{H}^2 and \vec{E}^2 respectively and summation of both equations as described in [51]. Interchanging the primes and repeating the process yields:

$$\vec{H}^1 \vec{\nabla} \times \vec{E}^2 + \vec{E}^1 \vec{\nabla} \times \vec{H}^2 = i\omega(\vec{E}^1 \epsilon \vec{E}^2 - \vec{H}^1 \mu \vec{H}^2) \quad (\text{II-51})$$

A final subtraction of both equations results in

$$\begin{aligned} \vec{\nabla}(\vec{E}^1 \times \vec{H}^2 - \vec{E}^2 \times \vec{H}^1) \\ = i\omega(\vec{E}^2 \epsilon \vec{E}^1 - \vec{E}^1 \epsilon \vec{E}^2 + \vec{H}^2 \mu \vec{H}^1 - \vec{H}^1 \mu \vec{H}^2) \end{aligned} \quad (\text{II-52})$$

If μ and ϵ are symmetric tensors or scalars, the right-hand side of this equation is zero and the equation can be written as the Lorentz reciprocity theorem for a source-less system:

$$\vec{\nabla}(\vec{E}^1 \times \vec{H}^2 - \vec{E}^2 \times \vec{H}^1) = 0 \quad (\text{II-53})$$

It can be shown that the scattering matrix of a system where the Lorentz reciprocity theorem applies has to be symmetric [51]. Since optical isolators and circulators, by definition, require an asymmetric scattering matrix, reciprocity must not apply, which is why they are called nonreciprocal elements.

Two methods to break reciprocity include nonlinear materials, e.g. utilizing stimulated Brillouin scattering [52] and time-dependent modulation of the refractive index [53]. However, the most common approach, is the use of magneto-optic materials that exhibit asymmetric tensors ϵ and μ to break the reciprocity of Equation (II-53) and utilize the Faraday effect or a nonreciprocal phase

shift. These types of isolators and circulators will be described more thoroughly in the following sections.

2. Faraday effect and free-space isolators

The most common design of an optical isolator is based on magneto-optic materials that exhibit a strong Faraday effect. The Faraday effect describes a nonreciprocal polarization rotation for polarized light that is transmitted through a magneto-optic material parallel to an applied static magnetic field, where the polarization rotation β is linear to the magnetic field:

$$\beta = vBd. \quad (\text{II-54})$$

In this case, v is the Verdet constant and d the interaction length between the electromagnetic wave and the medium and B the magnetic flux of an applied static magnetic field.

In optically active materials with a helical molecular structure, an electromagnetic wave induces circulating currents that generate an electric dipole moment (a polarization density \vec{P}) proportional to the magnetic flux density \vec{B} induced by the electromagnetic field. Taking the electric flux density \vec{D} introduced in equation (II-5):

$$\vec{D} = \epsilon\vec{E} + \vec{P}, \quad (\text{II-55})$$

\vec{P} can then be expressed as

$$\vec{P} = i\epsilon_0\zeta\omega\vec{B} = -\epsilon_0\zeta\nabla \times \vec{E}. \quad (\text{II-56})$$

With a plane wave $\vec{E} = \vec{E}_0 e^{i\vec{k}\vec{r}}$ approach, equation (II-55) with the substitution (II-56) becomes

$$\vec{D} = \epsilon\vec{E} + i\epsilon_0\zeta\vec{k} \times \vec{E} = \epsilon\vec{E} + i\epsilon_0\vec{G} \times \vec{E}. \quad (\text{II-57})$$

The gyration vector \vec{G} , describes an optically active medium with spatial dispersion in this equation since the polarization density depends not only on the electric field but also on the wave vector \vec{k} (analog to temporal dispersion, where a medium's properties depend on ω) and \vec{D} is no longer parallel to \vec{E} . As shown in chapter 6 of [45], the normal modes of such a medium correspond to left and right circularly polarized waves $\vec{E}_{circular}$ with the refractive index

$$n_{+/-} = \sqrt{n_0^2 \pm G}, \quad (\text{II-58})$$

leading to

$$\vec{D} = \epsilon_0 n_{+/-}^{-2} \vec{E}_{circular}. \quad (\text{II-59})$$

If $G = 0$, the refractive index for both circularly polarized waves is equal, and both waves travel with the same velocity. For $G \neq 0$, a circular birefringence is induced that corresponds to a polarization rotation. In general, this is a reciprocal effect since the gyration vector is proportional to the wave vector $\vec{G} = \zeta\vec{k}$, where the sign depends on the propagation direction. Thus, the polarization rotation of an electromagnetic wave is reversed by subsequent forward and backward propagation.

For magneto-optic materials however the polarization density \vec{P} can be expressed as

$$\vec{P} = i\epsilon_0 \vec{B}_{static} \times \vec{E}, \quad (\text{II-60})$$

and as an analogy to optically active media, the magnetic flux density can also be expressed with the gyration vector:

$$\vec{G} = \gamma \vec{B}_{static} \quad (\text{II-61})$$

In contrast to the time varying magnetic flux density \vec{B} that induces optical activity in helical molecular structures, \vec{B}_{static} describes an applied static magnetic field parallel or anti-parallel to the motion of the electromagnetic wave. Thus, magneto-optic materials require an external magnetic field, hence the name. Since equation (II-56) does not depend on the wave vector, a reversal of the propagation direction does not reverse the sense of rotation of the polarization plane. In other words: in contrast to reciprocal polarization rotations, created in optically active media like liquid crystals, where the polarization rotation in forward and subsequent backward transition cancel each other out, the polarization rotation of the Faraday effect in forward and backward transmission are added up.

This enables an optical isolator design that comprises a 45° Faraday rotor in between two polarization filters with 45° crossed transmission axes as depicted in Figure II-8. The standard notations of transverse electric (TE) and transverse magnetic (TM) polarization are used to describe the isolator's working principle: electromagnetic waves with no electric field along the transmission direction of the waveguide and the electric field entirely in the transverse plane are transverse electric or TE polarized. Similarly, they are called TM polarized if there is no magnetic field along the transmission direction with the magnetic field entirely in the transverse plane. In free-space optics, these correspond to s-polarized waves (TE polarization) and p-polarized waves (TM polarization), where s-polarized light describes an electromagnetic field with the electric field parallel to the laboratory system, or in this case the plane of the waveguides. Accordingly, p-polarization describes an electromagnetic field with the magnetic field parallel to the waveguide plane. For simplicity, the terms TE and TM polarization will be used for both, propagation of electromagnetic waves through waveguides and free-space throughout this work.

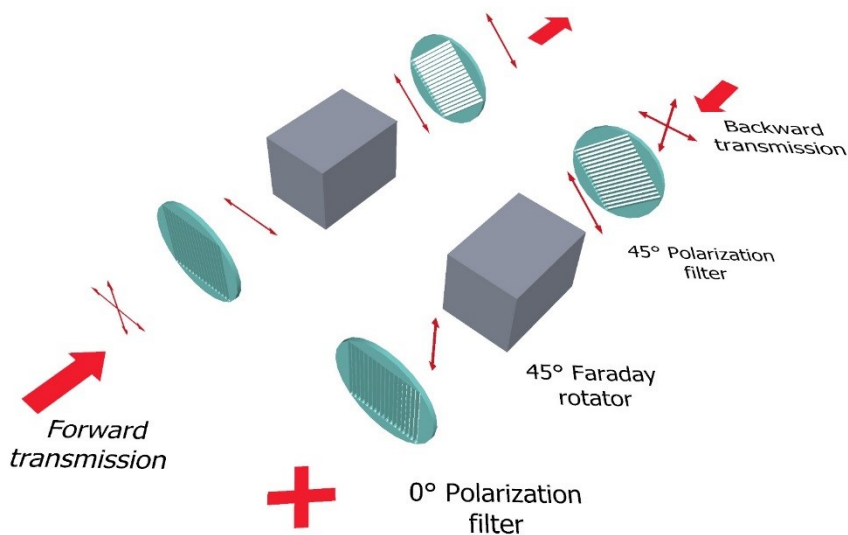


Figure II-8: Working principle of an optical isolator in forward and backward direction comprising of a 0° polarization filter, a 45° Faraday rotator, and a 45° polarization filter as described in the text.

Suppose an electromagnetic wave travels in forward direction through the isolator. In that case, TE polarized light passes the left polarization filter, its polarization state is rotated by 45° after

transmission of the Faraday rotator, and it can pass the right polarization filter. In backward direction, the intensity of both TE- and TM- polarized light is halved by partial absorption in the right polarization filter with a 45° transmission axis. After the nonreciprocal polarization rotation of the Faraday rotator, the axis of polarization is perpendicular to the transmission axis of the left polarization filter for both initial polarization states. Hence, backward propagating light is absorbed, preventing light transmission in the backward direction. In order to maintain TE (TM) polarization after transmission of the isolator, an optional 22.5° half-wave plate might be placed at the isolator's output.

This setup of an optical isolator is widely used in free-space optics to create bulk isolators at 1550 nm. Some of the most suitable magneto-optic materials for this approach are ferrimagnetic bismuth-doped rare earth iron garnets (BIG). BIGs can be grown as single crystals by liquid phase epitaxy (LPE) and have the composition $R_{3-x}Bi_xFe_{5-z}M_zO_{12}$, where R can be substituted for a rare earth element and M = Al, Ga, Si, Ge [54]. The advantages of BIGs over other materials include the strong Faraday rotation of up to 93 deg/mm, low insertion loss (<0.05 dB) at 1550 nm, and the ability to latch the material in a magnetically saturated single domain without an applied bias field [55]. Hence, they do not require an external magnetic field for the Faraday rotation. The latter is achieved by a low demagnetization energy compared to the energy of magnetic domain walls which makes the creation of new magnetic domains energetically unfavorable, similar to a permanent magnet. The integrated isolator developed within this work follows the working principle of a free-space isolator as depicted in Figure II-8. It makes use of BIGs as Faraday rotators, as will be described in the following sections after a short introduction of alternative concepts of integrated isolators and circulators.

3. Optical isolators and circulators in integrated photonics

Key performance specifications of optical isolators and circulators are the insertion loss (IL) and the isolation, defined as the difference between backward and forward IL. Besides these values, high optical return loss (ORL) is also essential to avoid intrinsic back reflections at the isolator structure itself. Good performance in only one of the first-mentioned parameters is not sufficient. An isolator or circulator that features low insertion loss but also low optical isolation or vice versa high optical isolation but also high insertion loss would not be suitable for any application. To take this into account, a unitless figure of merit (*FOM*) is introduced within this work as an additional parameter to assess isolator performance:

$$FOM = \frac{\text{Peak isolation ratio [dB]}}{\text{Insertion loss [dB]}} \quad (\text{II-62})$$

The higher the value, the better the performance. Since the isolation ratio also depends on the insertion loss, the chosen figure of merit favors devices with low IL. For example, the best performing standalone free-space isolators following the design shown in Figure II-8 feature insertion as low as 0.22 dB and typical isolations of 43 dB [56], resulting in $FOM = 195$. Fiber coupled isolators following a similar isolator setup achieve equal isolation ratios, but slightly higher insertion loss of 0.55 dB resulting in $FOM = 78$ [57]. Polarization-independent fiber-coupled free-space circulators have a $FOM = 50$ with isolations of 40 dB and typical insertion loss of 0.8 dB [58]. These values will serve as a reference to rank some of the following isolators in integrated photonics.

As previously mentioned, optical isolators and circulators must break the Lorentz reciprocity (equation (II-53)). Like in free-space optics, magneto-optic materials are also the most common approach in literature to achieve nonreciprocity for integrated optical isolators and circulators. Even though waveguide integrated Faraday rotators have been reported in [59] and [24], most

designs rely on a nonreciprocal phase shift effect (NRPS). In contrast to Faraday rotators where the light travels parallel (or anti-parallel) to the magnetic field, rotating the polarization, a NRPS occurs when the light travels perpendicular to the magnetic field in a magneto-optic material which alters the phase of the electromagnetic wave. This enables isolator and circulator designs based on interferometric devices like Mach-Zehnder interferometers (MZIs) [25, 28, 59] or microring resonators (MRRs) [23, 60] that were all demonstrated in silicon photonics except for [28], which is fabricated in GaInAsP/InP. As with free-space Faraday rotators, the best performing magneto-optic materials are Bi or Ce doped yttrium iron garnets (YIGs) that can be wafer bonded heterogeneously [23] or deposited [25] for monolithic integration. Even though state of the art isolators in SiP reported good optical isolations beyond 30 dB, this approach has two significant drawbacks. Firstly, the strong YIG absorption of up to \sim 60 dB/cm results in an overall higher loss. In [23], this was solved with a very small footprint of only 70 μ m yielding a loss of 2.3 dB. However, the MRR character of this device greatly limits the isolation bandwidth. The second major drawback is the polarization-dependent isolation of the reported devices. The NRPS requires a considerable mode overlap between the traveling mode in the waveguide and the magneto-optic (MO) material. MO deposited on top of the waveguide yields a high mode overlap with TM polarization and low overlap for TE polarization and vice versa for a sidewall deposition. Thus, the reported devices do not block an arbitrary polarization state but are polarization-dependent in contrast to free-space isolators. An overview of different reported integrated isolators and circulators in terms of isolation and insertion loss together with the figure of merit introduced in (II-62) is given in Figure II-9. The highest *FOM* reported (23.9 for [61]) is still two times smaller than for a fiber-coupled free-space circulator which has the lowest *FOM* of the commercially available devices.

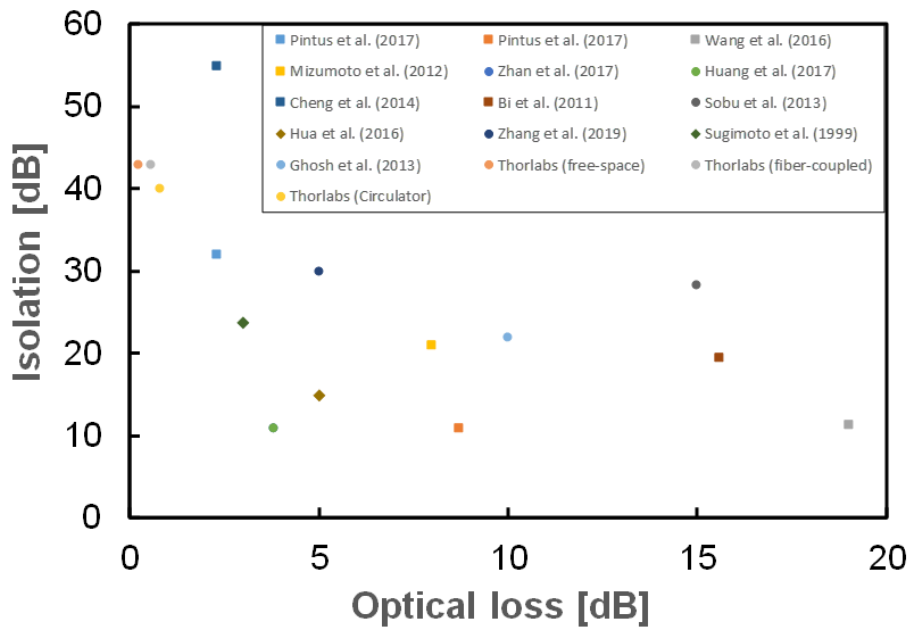


Figure II-9: Isolation and insertion loss cross-map of reported integrated isolators and circulators in literature together with commercially available free-space isolators and circulators from Thorlabs [23–28, 56–64].

4. Isolator and circulator designs in this work

Concept of an integrated isolator within this work

Considering the remarkable performance of free-space isolators and the possibility to create on-chip free-space sections in the PolyBoard, the integration of a free-space isolator as a whole is a straightforward and promising approach to realize integrated isolators that outperform other proposed designs in integrated photonics. Figure II-10 depicts a design for the integration of a free-space isolator in the PolyBoard. The device consists of embedded single-mode waveguides coupled to GRIN lenses to create an on-chip free-space section. A separately assembled isolator that follows the working principle described in Figure II-8 is placed in the free-space section.

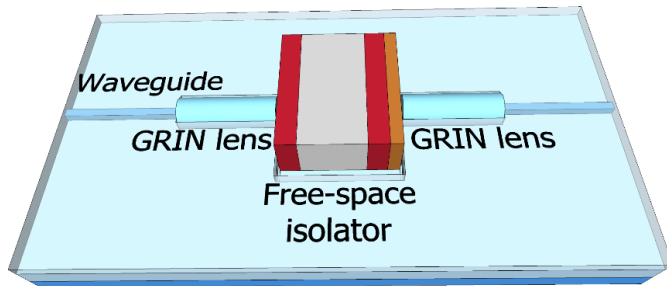


Figure II-10: Proposed scheme for an integrated isolator based on integrating a free-space isolator, as depicted in Figure II-8, in an on-chip free-space section. In order to maintain TE polarization for TE input, an additional half wave plate is bonded at the output of the free-space isolator.

To test the optical isolator during operation in a more complex PIC, it is also co-integrated with a tunable DBR laser. Due to their sensitivity to unwanted optical feedback, the co-integration of lasers and optical isolators is highly beneficial for the laser performance, since isolators stabilize the operation of the laser. Furthermore, the PolyBoard DBR laser is one of the standard building blocks of the platform mainly targeting applications in Telecom and Daracom. Until now it always required an external optical isolator within the housing of the laser or a fiber based optical isolator. The PolyBoard DBR laser comprises a tunable Bragg-grating, phase shifter, and a coupled InP gain element as depicted in Figure II-11. Chapter IV.A.3 will explain the working principle of the laser in more detail.

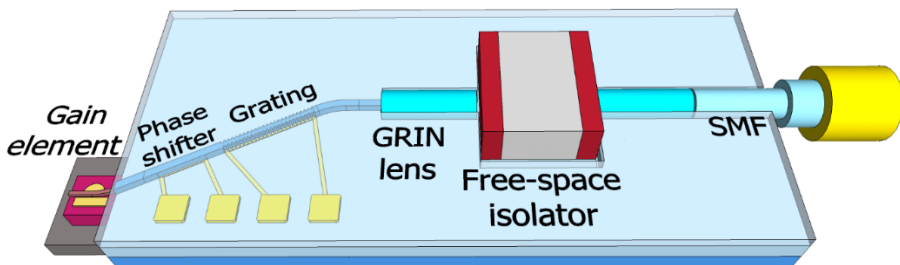


Figure II-11: Schematic layout of a tunable distributed Bragg-reflector laser with integrated optical isolator and direct fiber-to-chip coupling via a U-groove. The DBR laser comprises an InP gain element, a Bragg grating, and a phase shifter.

Concept of an integrated circulator based on nonreciprocal polarization rotation

The design of a polarization-independent circulator requires two on-chip free space sections both equipped with a -45° Faraday rotator and 22.5° half wave plate. A polarization beam splitter at the input and output finalize the design. The schematic design is depicted in Figure II-12 and the working principle in Figure II-13.

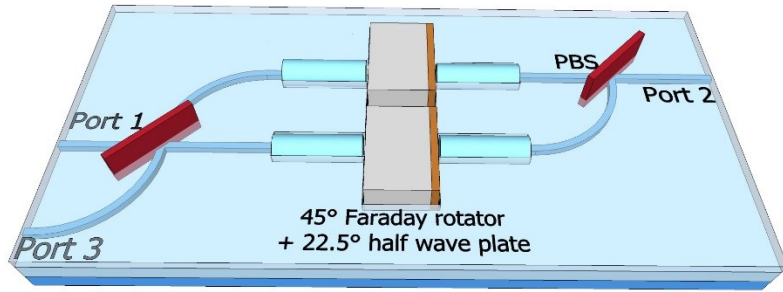


Figure II-12: Schematic design of the proposed circulator consisting of an input and output polarization beam splitter (PBS) and two free-space sections with inserted Faraday rotator and a half-wave plate.

Starting from port 1, TE polarized light is transmitted through the PBS in the lower arm, while TM polarization is reflected into the upper arm of the circulator. In forward transmission (from left to right), the combination of a -45° Faraday rotator and 22.5° half-wave plate induces a nonreciprocal polarization rotation, and TE polarization in the lower arm becomes TM polarization and vice versa in the upper arm. The second PBS combines both polarizations that are now switched and guides them to port 2. In backward transmission, TE and TM polarization are again split at the right-hand side PBS and guided through the free-space sections, and the polarization state is maintained in both arms. Thus, both polarizations are blocked for transmission to port one and instead guided to port three at the left PBS.

The Faraday rotators are weak permanent magnets that maintain their magnetization state without the necessity of an external magnetic field. However, using a strong magnetic flux (>50 mT at room temperature), it is possible to reverse the polarity of the magnetization and Faraday rotation. A reversed Faraday rotation also reverses the nonreciprocal polarization rotation of the Faraday rotator and HWP inside the free-space section depicted in Figure II-12. For a 45° FR and 22.5°HWP, TE and TM polarized light maintain their polarization state in forward direction (from left to right), and the polarization is reversed from TE to TM and TM to TE in backward direction. For a -45° Faraday rotator the polarization is reversed in forward and maintained in backward direction. Consequently, light coupled into port 2 is either transmitted to port 1 or port 3, depending on the magnetization state of the Faraday rotators. Thus, it is possible to reverse the light circulation and use the circulator as a latching switch since the Faraday rotators maintain their magnetization (and the switch configuration) and only require an initial magnetic field during active switching (Figure II-13).

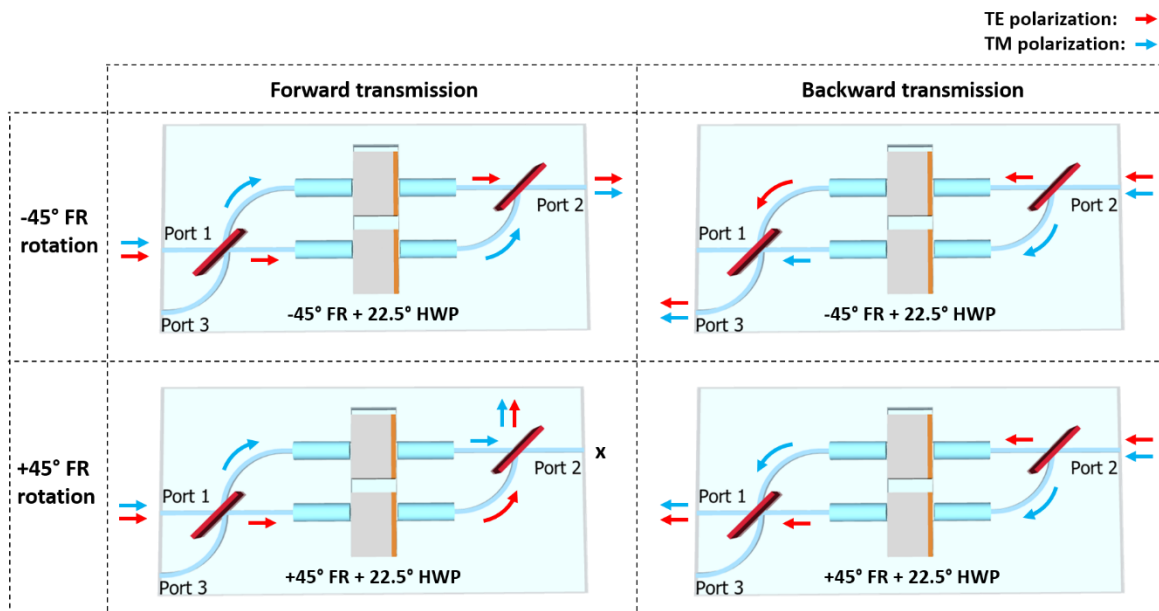


Figure II-13: Working principle of the optical circulator depicted in Figure II-12. For a -45° Faraday rotation (FR), light travels from port 1 to port 2 to port 3. A $+45^\circ$ Faraday rotation reverses the transmission direction, and light travels from port 2 to port 1.

Concept of an integrated circulator based on a nonreciprocal phase shift

The previous circulator design is similar to commercially available free-space circulators that utilize birefringent walk-off crystals, Faraday rotators, and HWPs. Another design exclusive to integrated photonics is based on a Mach-Zehnder interferometric structure with two multimode interference couplers first demonstrated in [59] with silica-based waveguides. Like the first circulator, it comprises two optical paths with an on-chip free-space section with inserted Faraday rotator and a HWP but instead of PBSs for polarization splitting and combining, it uses MMIs for phase-sensitive beam splitting and combining. Additionally, a phase shifter and a variable optical attenuator are placed in each interferometer arm to stabilize the optical phase and minimize the imbalance in both arms. The schematic design is depicted in Figure II-14.

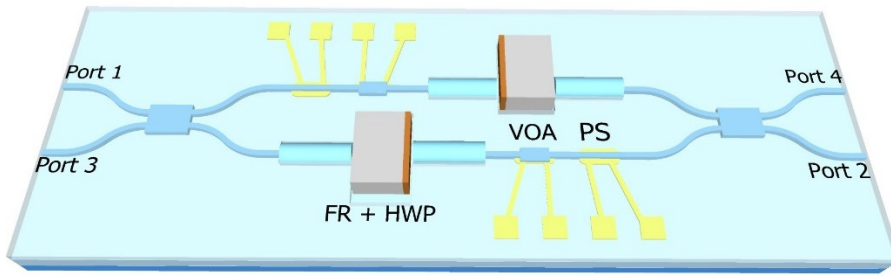


Figure II-14: Four-port Mach-Zehnder-based circulator that comprises of two free-space sections with inserted Faraday rotator (FR) and half-wave plate (HWP) and a variable optical attenuator (VOA) and phase shifter (PS) in each arm.

The working principle of the PBS circulator from Figure II-12 is based on a nonreciprocal polarization rotation as described in Figure II-13. The MZI circulator utilizes a nonreciprocal phase shift in forward and backward direction. Like the PBS circulator, the integrated Faraday rotator and HWP in each arm induce a nonreciprocal polarization rotation, but also a nonreciprocal phase shift. In the PBS circulator, this phase shift is not used since the working principle is based on the polarization of light. However, in the MZI circulator, this can be utilized due to the working principle of MMIs.

An easy formalism to describe this phase shift induced by a nonreciprocal polarization rotation is the Jones calculus. In the Jones calculus, the polarization state of an electromagnetic wave is described by a two-dimensional Jones vector that propagates through optical elements described by 2×2 matrices as described in chapter 8 of [65]. The Jones vector \vec{J} for a plane wave electric field is given by

$$\begin{pmatrix} E_x(z, t) \\ E_y(z, t) \end{pmatrix} = \underbrace{\begin{pmatrix} E_{x_0} e^{i\phi_x} \\ E_{y_0} e^{i\phi_y} \end{pmatrix}}_{\vec{J}} e^{i(kz - \omega t)}, \quad (\text{II-63})$$

where E_{i_0} describes the amplitude in x and y direction and ϕ_i contains the phase information. Here, TE polarized light is described by a $\begin{pmatrix} 1 \\ 0 \end{pmatrix}$ vector and TM polarized light by a $\begin{pmatrix} 0 \\ 1 \end{pmatrix}$ vector. The matrices for a half-wave plate and a Faraday rotator are given by

$$M_{HWP} = e^{-\frac{i\pi}{2}} \begin{pmatrix} \cos(2\theta) & \sin(2\theta) \\ \sin(2\theta) & -\cos(2\theta) \end{pmatrix} \quad (\text{II-64})$$

$$M_{Faraday} = e^{-\frac{i\pi}{2}} \begin{pmatrix} \cos(\sigma) & -\sin(\sigma) \\ \sin(\sigma) & \cos(\sigma) \end{pmatrix}, \quad (\text{II-65})$$

where $\sigma = 45^\circ$ is the Faraday rotation and $\theta = \pm 22.5^\circ$ the optical axis of the HWP. The upper MZI circulator comprises a -22.5° HWP and a 45° Faraday rotator, while the lower arm consists of a 45° Faraday rotator and a 22.5° HWP. The multiplication of the elements describes transmission through these elements according to the order of propagation. For example, forward transmission through the upper arm of the MZI circulator with an HWP and a Faraday rotator is given by

$$\begin{aligned} \begin{pmatrix} E_x(z, t) \\ E_y(z, t) \end{pmatrix}_{\text{final, upper arm}} &= (M_{Faraday} \cdot M_{HWP}) \begin{pmatrix} E_x(z, t) \\ E_y(z, t) \end{pmatrix}_{\text{initial, upper arm}}. \end{aligned} \quad (\text{II-66})$$

Table II-1 depicts the Jones matrices in forward and backward direction of the lower and upper arm of the MMI for a -22.5° HWP in the upper arm and a 22.5° HWP in the lower arm together with a 45° faraday rotator as depicted in Figure II-14.

Table II-2: Jones matrices for a -22.5° HWP and 45° Faraday rotator in the upper arm and a 22.5° and 45° Faraday rotator in the lower arm of the MZI circulator.

	Forward transmission	Backward transmission
Upper arm	$\begin{pmatrix} -1 & 0 \\ 0 & 1 \end{pmatrix}$	$\begin{pmatrix} 0 & 1 \\ 1 & 0 \end{pmatrix}$
Lower arm	$\begin{pmatrix} -1 & 0 \\ 0 & 1 \end{pmatrix}$	$\begin{pmatrix} 0 & -1 \\ -1 & 0 \end{pmatrix}$

From Table II-2 two things are apparent. First, the Jones matrix in both arms is an identity matrix in forward transmission, meaning both arms maintain their polarization state. The negative sign in the first matrix entry indicates that TE polarization experiences a phase shift of π in both arms. In backward transmission, an antisymmetric matrix corresponds to a nonreciprocal polarization rotation from TE \rightarrow TM and TM \rightarrow TE. This behavior also explains the operation of the PBS-based circulator in Figure II-13. Secondly, a phase shift is introduced in backward transmission between both arms since the first antisymmetric matrix is positive and the second negative. This nonreciprocal phase shift between both arms in combination with the MMIs that switch their

output port according to the input light's phase relation is the MZI circulator's underlying mechanism. A 2x2 MMI introduces a phase shift of π between both outputs, which means that the initial polarization in the upper and lower arm for a mixed TE and TM polarization state is given by

$$\begin{pmatrix} E_x(z, t) \\ E_y(z, t) \end{pmatrix}_{\text{upper arm}} = \begin{pmatrix} E_{x_0} e^{i\phi_x} \\ E_{y_0} e^{i\phi_y} \end{pmatrix} e^{i(kz - \omega t)} \quad (\text{II-67})$$

and

$$\begin{pmatrix} E_x(z, t) \\ E_y(z, t) \end{pmatrix}_{\text{lower arm}} = - \begin{pmatrix} E_{x_0} e^{i\phi_x} \\ E_{y_0} e^{i\phi_y} \end{pmatrix} e^{i(kz - \omega t)} \quad (\text{II-68})$$

respectively for light entering port 1 [66]. In forward direction, both electromagnetic waves maintain their phase relation (first column in Table II-2) in the upper and lower arm. They are combined in the second MMI and guided towards the lower port, port 2, of the circulator. In backward direction, the induced phase shift of the MMI is canceled by the phase shift of HWP and Faraday rotator (second column in Table II-2) and guided to the lower port, port 3, instead of port 1. Thus, it can be shown with the Jones calculus that light inside the circulator travels from port 1 to port 2 to port 3 to port 4 and from port 4 back to port 1.

D. Nonlinear elements

Besides nonreciprocal elements for isolators and circulators described in the previous section, this work also demonstrates second-harmonic generation in the PolyBoard. After introducing the nonlinear wave equation and a model for SHG, Boyd's and Kleinmann's theory for SHG with focused Gaussian beams is briefly discussed within this section. Furthermore, periodic poling for phase matching in nonlinear crystals is introduced, and conversion efficiency values for state-of-the-art integrated SHG sources in literature are reported.

1. Nonlinear polarization density and nonlinear wave equation

In the first section of this chapter, Maxwell's third and fourth equation in a medium (equation (II-3) and (II-4)) with

$$\vec{D} = \epsilon_0 \vec{E} + \vec{P}(\vec{E}) \quad (\text{II-69})$$

were introduced, where the polarization density \vec{P} can be defined as the sum of the electric dipole moments induced by an electric field in a medium. Thus, it describes the response of a medium to an interaction with the electromagnetic field. A linear dielectric medium is represented by a linear response of the medium to the electric field. In II.C.2, \vec{P} was used to describe the linear response of a magneto-optic medium to an electromagnetic field, resulting in the Faraday effect. In contrast, nonlinear media are defined by their nonlinear response that can result either from the individual dipole moments of the material or the number density of the dipoles. Since electric fields of light are typically small compared to interatomic electric fields, the response of the medium to the electric field can be approximated by the Taylor expansion:

$$\vec{P} = \epsilon_0 \chi^{(1)} \vec{E} + \underbrace{\chi^{(2)} \vec{E}^2 + \chi^{(3)} \vec{E}^3 + \dots}_{\vec{P}_{NL}} \quad (\text{II-70})$$

Here, $\chi^{(i)}$ describes the i th-order susceptibility of the medium. The first term represents the linear response of the medium that dominates for small electric fields, whereas the second term, third

term, etc. describe the second-order, third-order nonlinear response summarized as \vec{P}_{NL} . For simplicity, anisotropy, dispersion, and inhomogeneity are ignored in this consideration.

Nonlinear Wave equation

In Equations (II-7) and (II-8) the wave equation for an electromagnetic field was obtained from Maxwell's equations to derive the Gaussian beam solution in the paraxial approximation. In this case \vec{P} was assumed to be proportional to the electric field. Considering a nonlinear response of \vec{P} , like in equation (II-70), the wave equation can be written as

$$\underbrace{\nabla^2 \vec{E} - \frac{n^2}{c_0^2} \frac{\delta^2 \vec{E}}{\delta t^2}}_{\text{Linear wave equation}} = 0 + \underbrace{\mu_0 \frac{\delta^2 \vec{P}_{NL}}{\delta t^2}}_{\text{Nonlinear part}}, \quad (\text{II-71})$$

known as the nonlinear wave equation (derivation in chapter 19 of [45]). In general, the nonlinear wave equation is a nonlinear partial differential equation that can be physically interpreted as the electromagnetic wave propagating in a linear medium, where the nonlinear term acts as a radiating source. Considering only the second-order nonlinearity term

$$\vec{P}_{NL} = X^{(2)} \vec{E}^2 \quad (\text{II-72})$$

and assuming an electric field comprising of two optical frequencies ω_1 and ω_2 described by

$$\vec{E} = \vec{E}_1 e^{-i\omega_1 t} + \vec{E}_2 e^{-i\omega_2 t} + c.c., \quad (\text{II-73})$$

where *c. c.* is the complex conjugates of the first two terms, the \vec{P}_{NL} can be rewritten as:

$$\begin{aligned} \vec{P}_{NL} \sim & \vec{E}_1^2 e^{-i2\omega_1 t} + \vec{E}_2^2 e^{-i2\omega_2 t} + 2\vec{E}_1 \vec{E}_2 e^{-i(\omega_1+\omega_2)t} \\ & + 2\vec{E}_1 \vec{E}_2 e^{-i(\omega_1-\omega_2)t} + |\vec{E}_1|^2 + |\vec{E}_2|^2 + c.c. \end{aligned} \quad (\text{II-74})$$

Hence, the nonlinear polarization density is proportional to terms with the frequency components $2\omega_1$, $2\omega_2$, $\omega_1+\omega_2$, $\omega_1-\omega_2$ and a DC signal corresponding to $|\vec{E}_1|^2 + |\vec{E}_2|^2$ term. Processes involving second-order nonlinearity are called three-wave mixing and include second-harmonic generation, sum-frequency generation, difference-frequency generation, and optical rectification.

2. Second-harmonic generation

For degenerate pump frequencies $\omega = \omega_1 = \omega_2$, \vec{P}_{NL} has a source term of frequency 2ω resulting in second-harmonic generation, and equation (II-74) simplifies to

$$\vec{P}_{NL} \sim \vec{E}_1^2 e^{-i2\omega_1 t} + |\vec{E}_1|^2 + c.c. \quad (\text{II-75})$$

Thus, the nonlinear medium acts as a radiating source that creates an electromagnetic field at twice the pump light frequency. However, this nonlinear polarization density does not take the phase of the incident light into account. In a more general consideration, the phase relation of the incident electrical fields also plays a role, and the electrical field in equation (II-73) for a single frequency field can be written as

$$\vec{E} = \vec{E}_1 e^{i(\vec{k}\vec{x} - \omega_1 t)} + c.c., \quad (\text{II-76})$$

where \vec{k} is the wave vector and \vec{x} is the position of the electric field, which again results in a nonlinear polarization density of

$$\vec{P}_{NL} \sim \vec{E}_1^2 e^{i(2\vec{k}_1 - 2\omega_1 t)} + |\vec{E}_1|^2 + c.c. \quad (\text{II-77})$$

Taking the nonlinear wave equation (II-71) for the second harmonic 2ω with \vec{P}_{NL} and asserting the slowly varying envelope approximation, negligible loss, and an electrical field of the second harmonic much smaller than the pump field, the nonlinear wave equation can be simplified to

$$\vec{\nabla} \vec{E}_{2\omega} \sim \vec{E}_\omega^2 e^{i(\Delta\vec{k}\vec{x} - \omega_1 t)} + c.c., \quad (\text{II-78})$$

with the phase-matching condition $\Delta\vec{k} = \vec{k}_{2\omega} - 2\vec{k}_\omega$. This equation can be solved by integration and written in terms of optical intensity $I = \frac{n}{2} \sqrt{\frac{\epsilon_0}{\mu_0}} |E|^2$ as shown in chapter 2.2 of [67]:

$$I_{2\omega} = \frac{2\omega^2 d_{eff}^2 l^2}{n_{2\omega} n_\omega^2 c^3 \epsilon_0} \left(\frac{\sin\left(\frac{1}{2} \Delta k l\right)}{\frac{1}{2} \Delta k l} \right)^2 I_\omega^2. \quad (\text{II-79})$$

In this formula, the three-dimensional description of \vec{E} was simplified to the one-dimensional case resulting in scalars for the position and the wave vector. In equation (II-79), l denotes the interaction length of the nonlinear medium, $n_{2\omega}$ the refractive index of the second harmonic, n_ω the refractive index of the incident field and d_{eff} the effective nonlinear coefficient, which is the scalar form of the $\chi^{(2)}$ tensor in the one-dimensional case. Formula (II-79) is a general description of the second harmonic intensity that can be used as a rule of thumb to estimate the conversion efficiency $\eta = I_{2\omega}/I_\omega$ for second-harmonic generation. The intensity of the second harmonic scales quadratically with d_{eff} , a material property of the nonlinear medium, the interaction length l and pump intensity I_ω . Thus, the conversion efficiency scales linearly with the pump intensity. Since the intensity is defined as power per cross-sectional area, the best conversion efficiency is achieved by focusing the highest possible power to the smallest possible area with a long interaction length in a medium with a high nonlinear coefficient. The Δk term in equation (II-79) describes the phase-matching condition. For perfect phase matching it becomes equal to 1, which is due to material dispersion in a medium usually not the case. An approach to optimize phase matching is quasi-phase-matching (QPM) via periodic poling that will be discussed in section 4.

3. Boyd-Kleinman condition

The previous chapter describes SHG for plane waves and equation (II-79) offers a good intuition about the different parameters involved in SHG, especially the phase matching condition. However, the electric field in space is usually localized, requiring the electric field's description by a Gaussian beam. Boyd and Kleinman [30] derived a formula for the conversion efficiency of a Gaussian beam similar to the plane wave solution in (II-79). In [30] they showed that the conversion efficiency for a Gaussian beam in terms of optical power is described by

$$P_{2\omega} = \frac{2\omega^2 d_{eff}^2 l k_\omega}{\pi n_{2\omega} n_\omega^2 c^3 \epsilon_0} P_\omega^2 h(\sigma, B, \xi), \quad (\text{II-80})$$

which can also be derived from the nonlinear wave equation and the nonlinear polarization density for a Gaussian beam. Here, $h(\sigma, B, \xi)$ is given by the non-elementary integral

$$h(\sigma, B, \xi) = \frac{1}{4\xi} \iint_{-\xi}^{\xi} \frac{e^{i\sigma(\tau-\tau')} e^{-B^2(\tau-\tau')}}{\xi(1+i\tau)(1-i\tau')} d\tau d\tau', \quad (\text{II-81})$$

that can only be solved numerically. The parameters in this equation are the focusing parameter $\xi = l/b$, the walk-off parameter $B = \theta\sqrt{lk_\omega}/2$ and $\sigma = b\Delta k/2$ with the Gaussian beam confocal parameter b , the walk-off angle θ , and the substitute $\tau^{(i)} = 2(z^{(i)} - f)/b$ with the focal point f , based on Boyd's and Kleinman's approach to solving the wave equation from an observer's point of view z outside the crystal and the radiating source z' inside. Like the phase-matching term in (II-79), $h(\sigma, B, \xi)$ has to be maximized for efficient SHG. Values of $h(\sigma, B, \xi)$ are plotted in Figure II-15 for an approximated solution derived by Chen and Chen [68], where $\sigma = 0$ is assumed for perfect phase matching ($\Delta k = 0$).

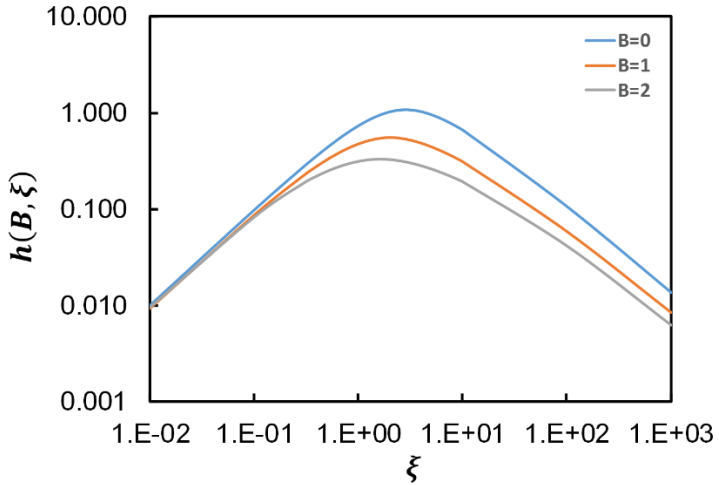


Figure II-15: Numerical approximation for the solution of the non-elementary integral $h(\sigma, B, \xi)$ depending on the confocal parameter ξ and the walk-off parameter B .

For zero walk-off ($B = 0$), the maximum conversion efficiency is at a focusing parameter of $\xi = 2.84$, known as the Boyd Kleinman condition for optimal focusing. In general, optimizing this value is not too critical, with broad tolerances between $1.52 < \xi < 5.3$ still covering 90% of the efficiency. The zero walk-off assumption is generally not valid for crystals with birefringent critical phase matching due to the spatial walk-off of the focusing beam for the extraordinary polarization. Still, it holds for noncritical phase matching e.g. the later introduced quasi-phase-matching. Overall, the Boyd Kleinman condition limits the efficiency of focusing inside the crystal for Gaussian beams. This lies within the different Gouy phase shifts of the pump beam and the second harmonic due to the nonlinear polarization density that induces an increasing phase mismatch. Since the Gouy phase is larger for stronger focusing, this results in an increasing phase mismatch and thus lower conversion efficiency.

The derived formulas for the second harmonic for a plane wave approach and a Gaussian beam are similar concerning the different parameters. However, one crucial difference besides the non-elementary integral in the Boyd Kleinman solution is the dependency of the second harmonic on the length l of the crystal. The second harmonic intensity scales quadratically with the length for the plane-wave solution and only linearly for the Gaussian beam solution. This can be explained by the inherent beam divergence of Gaussian beams, which results in a continually decreasing beam intensity, affecting the conversion efficiency. In contrast, the intensity of a plane wave is constant. Both approaches assume a constant pump field corresponding to low conversion efficiencies.

At high conversion efficiencies, pump depletion has to be considered and the overall conversion efficiency is diminished with respect to the equations (II-79) and (II-80). Using a Green's-function analysis together with a perturbation theory approach as described in [69, 70], the following solution for the second-harmonic power of a Gaussian beam can be derived:

$$P_{2\omega} = K P_\omega^2 h(\sigma, B, \xi) - K^2 P_\omega^3 h_2(\sigma, B, \xi) + K^3 P_\omega^4 h_3(\sigma, B, \xi) + \dots \quad (\text{II-82})$$

The first term in this equation equals equation (II-80), with the fractional term abbreviated as K. With pump depletion, additional higher-order terms diminish the overall conversion efficiency. This work uses a continuous-wave laser source and a femtosecond laser source to pump a nonlinear crystal. For the CW source with a few milliwatts of output power, equation (II-80) is sufficient to describe the conversion efficiency. With a peak output power of a few kilowatts, pump depletion is not negligible and equation (II-82) is more accurate for the description of SHG.

It is noteworthy that the second harmonic has the same confocal parameter as the fundamental beam but with a reduced waist of $w_{2\omega} = \frac{w_\omega}{\sqrt{2}}$ or half the effective mode area, later of interest for the coupling efficiency of second-harmonic Gaussian beams into GRIN lenses. This smaller waist can be explained by the magnitude of the nonlinear polarization density being proportional to the square of the electric pump field, which for a Gaussian beam again results in a Gaussian beam but with a smaller radius.

4. Phase-matching with periodic poling

In equation (II-79), the intensity of the second harmonic follows a squared *sinc*-function of the phase-matching condition

$$\Delta\vec{k} = \vec{k}_{2\omega} - 2\vec{k}_\omega \quad (\text{II-83})$$

plotted in Figure II-16. For efficient SHG, the difference between the pump and the SH wave vectors must be zero or close to zero.

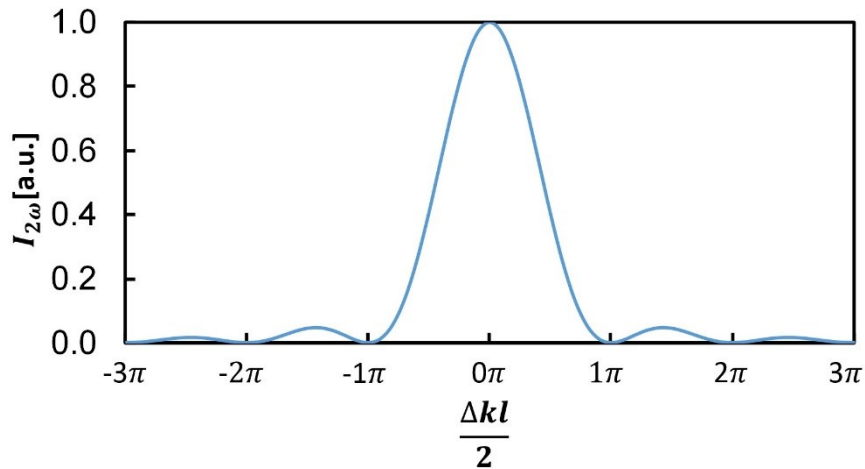


Figure II-16: Intensity of the second harmonic depending on the phase-matching condition Δk . With an increasing phase mismatch, the second harmonic power drops significantly.

In a nonlinear crystal without any phase matching, this is usually not the case due to dispersion, which leads to contributions of the second harmonic from different positions in the crystal with a continuously varying phase relation. If the phase mismatch created by a crystal length of L_C is smaller than π , SH waves from different points of the interaction length interfere constructively. If it is larger than π , the electromagnetic fields start to interfere destructively with amplitude contributions of previously created SH waves. This results in a diminished net output power of the second harmonic, as depicted in Figure II-16. L_C is called the coherence length of the crystal [71], defined as

$$L_C = \frac{\pi}{\Delta k}. \quad (\text{II-84})$$

One way to avoid a dispersion-related phase mismatch is birefringent phase matching. In birefringent phase matching, the crystal orientation (critical phase matching) or temperature (noncritical phase matching) can be used to achieve phase matching. A second method described by Armstrong et al. is a periodic sign reversal of the nonlinear susceptibility $\chi^{(i)}$ inside the crystal, known as periodic poling or quasi-phase-matching [72]. A QPM crystal allows a small phase mismatch between pump and SH within the coherence length, but whenever a reversal of energy flow due to an increasing phase mismatch would occur, $\chi^{(i)}$ and thus, the nonlinear coefficient utilized for SHG is reversed. This ensures a maximized SH at the output of the crystal. Figure II-17 depicts the SH intensity from equation (II-79) for a plane wave depending on the crystal length for different phase matching techniques.

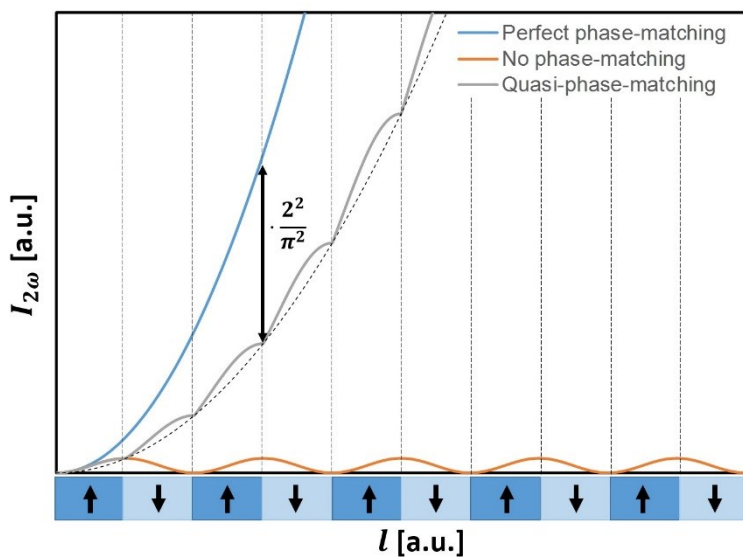


Figure II-17: Quasi-phase-matching in a periodically poled nonlinear crystal with highlighted sign reversal of the nonlinear coefficient, compared to perfect phase-matching and no phase-matching at all. The efficiency of QPM compared to ideal phase-matching is reduced by $2^2/\pi^2$.

Figure II-17 shows that for QPM, the effective nonlinear coefficient d_{QPM} given by

$$d_{QPM} = \frac{2}{\pi m} d_{eff}, \quad (\text{II-85})$$

is reduced by $2/\pi$ compared to perfect phase matching [71] since a small phase mismatch is always allowed between both electromagnetic fields. Here, m is the phase-matching order. Even though the nonlinear coefficient is reduced for QPM compared to perfect phase matching, QPM can utilize coefficients with a higher nonlinearity, where the pump and second harmonic wave have the same polarization. This is usually not the case in birefringent phase matching and is referred to as type 0 phase matching. For example, in lithium niobate birefringent phase matching utilizes the $d_{31} = 4.35 \text{ pm/V}$ coefficient, whereas QPM uses the $d_{33} = 27 \text{ pm/V}$ tensor entry [73]. The period length of a QPM crystal, defined as the length of two consecutive domains with a reversed sign of the nonlinear coefficient, is given by twice the crystal coherence length

$$\Lambda = 2mL_C, \quad (\text{II-86})$$

used to calculate the required domain width and period length of a QPM crystal. Here, m again is the phase-matching order. Due to higher order phase matching m , one crystal can support multiple

nonlinear interactions with only one poling period. This will be observed for the SHG measurements in V.D.3, where also higher-order frequency conversions occur.

The most common fabrication method for periodically poled crystals is ferroelectric domain engineering, as described in [74]. In ferroelectric domain engineering, a strong electric field is applied to reverse the domains according to the period length with the help of patterned electrodes at the crystal surface.

5. Materials for second-harmonic generation

Materials used for SHG exhibit no inversion symmetry and a high nonlinear coefficient. Typical nonlinear crystals include beta-barium borate (BBO), potassium titanyl phosphate (KTP), or lithium niobate (LN). While BBO and KTP are primarily used in free-space setups, LN can also be utilized to inscribe waveguides for integrated SHG sources. Other materials with a high $\chi^{(2)}$ for waveguide fabrication include AlN and Si_3N_4 [75]. Conversion efficiencies in literature are either reported as total efficiencies in % or as relative efficiencies in %/W. The latter, favoring low pump power sources, is often used in integrated photonics. Some noteworthy publications for integrated devices and free-space setups are listed below:

- The highest %/W conversion efficiency was achieved in [76] with 250,000 %/W. Lu et al. used a high Q microring resonator in lithium niobate with a total conversion efficiency of 15 % to achieve this value.
- In [36], Jankowski et al. demonstrated a conversion efficiency of 50 % for a 6 mm long periodically poled nanophotonic lithium niobate waveguide for SHG from 2050 nm to 1025 nm with a femtosecond pulsed laser.
- Several publications on SHG in AlN are available with the highest conversion efficiency of 12 % achieved by Guo et al. in 2016 with a high Q-factor microring resonator. This corresponds to a 2500 %/W conversion efficiency with a continuous wave laser from around 1550 nm to 775 nm [77].
- Even though Si_3N_4 has no inversion symmetry, Lu et al. demonstrated up to 22 % SH efficiency (2500 %/W) for a photo-induced $\chi^{(2)}$ in high Q microring resonators for a continuous wave laser from 1550 nm to 775 nm [75].
- A conversion efficiency of 36 % was achieved for a single pass 40 mm ppLN bulk crystal by Sané et al. [78].
- In a free-space double resonant cavity, a conversion efficiency of 52 % was achieved for a ppLN bulk crystal in [79].
- For a femtosecond pulsed laser pumped ppLN bulk crystal, conversion efficiencies of 83 % were reported in [80].

In this work, periodically poled Mg:O doped lithium niobate crystals are used for SHG fabricated by Coversion¹ for frequency conversion from 1540 nm to 770 nm. The crystals have a length of 1 mm and the highest nonlinear coefficient of $\chi^{(2)}$ for this material is $d_{33} = 25 \text{ pm/V}$. This corresponds to a typical effective nonlinear coefficient of $d_{QPM} = 14 \text{ pm/V}$ for the periodically poled crystal. The period length calculated with Equation (II-86) for first-order phase-matched SHG with a 1540 nm pump source and an Mg:O doped lithium niobate crystal at room temperature is $19.1 \mu\text{m}$, which is also the periodicity stated by Coversion. To calculate the period length, $k_i = \frac{2\pi n(\lambda_i)}{\lambda_i}$ with the Sellmeier equation for Mg:O doped lithium niobate in the Appendix A.1 was used.

¹ <https://www.coversion.com/en/>

Fundamentals

The crystals will be inserted into an on-chip free-space section with collimating and focusing lenses that have a focusing parameter of $\xi_{collimated} = 0.1$ and $\xi_{focused} = 3.3$ respectively (see Figure II-15). This corresponds to maximized h parameters of $h_{collimated} = 0.1$ and $h_{focusing} = 1.06$. In other words using focusing lenses for SHG should be roughly ten times as efficient as as collimated lenses. Following Equation (II-80), a conversion efficiency of 0.07 %/W should be expected for the focusing lenses. Figure II-18 depicts a schematic layout of the chip used for the integration of the ppLN crystal. Similar to the free-space section used to integrate an optical isolator in Figure II-10, it comprises an input and output waveguide with a GRIN lens-created free-space section in between. For chip characterization, cleaved standard single-mode fibers for 1550 nm are coupled directly to the input and output waveguide and fixed with glue.

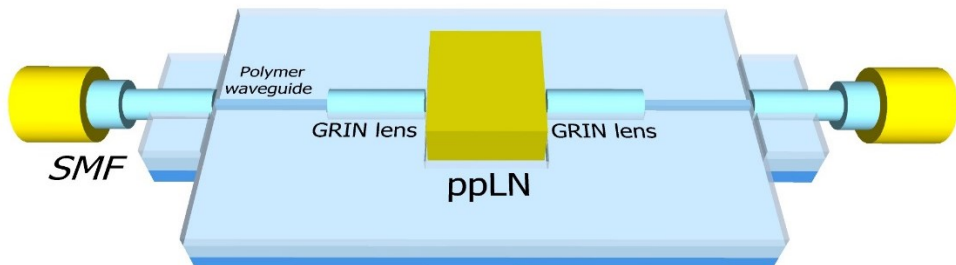


Figure II-18: Schematic layout of the polymer PIC for second-harmonic generation. The device consists of an on-chip free-space section with an inserted ppLN crystal. For better handling, an input and an output cleaved SMF-28 are coupled and glued to the polymer waveguides.

III. Simulation

In II.B a model for the on-chip free-space sections based on the propagation of Gaussian beams with ABCD matrices was derived. This chapter uses the approach to calculate the coupling loss of free-space sections based on GRIN lenses with two different numerical apertures and two waveguide geometries. The first section calculates the optical modes of the polymer waveguides that are coupled to the GRIN lenses. These are used afterwards to calculate the overall coupling loss of different free-space sections regarding the free-beam section's propagated length and the GRIN lens length.

A. Optical modes in polymer waveguides

The polymer waveguides from which the Gaussian mode is launched into the free-space section comprise a higher refractive index core material embedded in a polymer cladding. In this work, two different waveguide geometries with two different core refractive indexes are used. The first waveguide has a cross-section of $3.2 \times 3.2 \mu\text{m}^2$ with a core refractive index of $n_{core} = 1.48$ embedded in a cladding with $n_{cladding} = 1.45$. The second waveguide geometry has a cross-section of $7.3 \times 7.3 \mu\text{m}^2$ and a core refractive index of $n_{core} = 1.455$ embedded in the same cladding material. Based on these values, the beam propagation solver of Fimmwave is used to calculate the optical modes of both waveguides at 1550 nm. In addition to the quadratic cross-section with a width of $3.2 \times 3.2 \mu\text{m}^2$, an inversely tapered waveguide with the same height but reduced width of $0.8 \times 3.2 \mu\text{m}^2$ is simulated. The different geometries with their corresponding mode field diameters are depicted in Figure III-1.

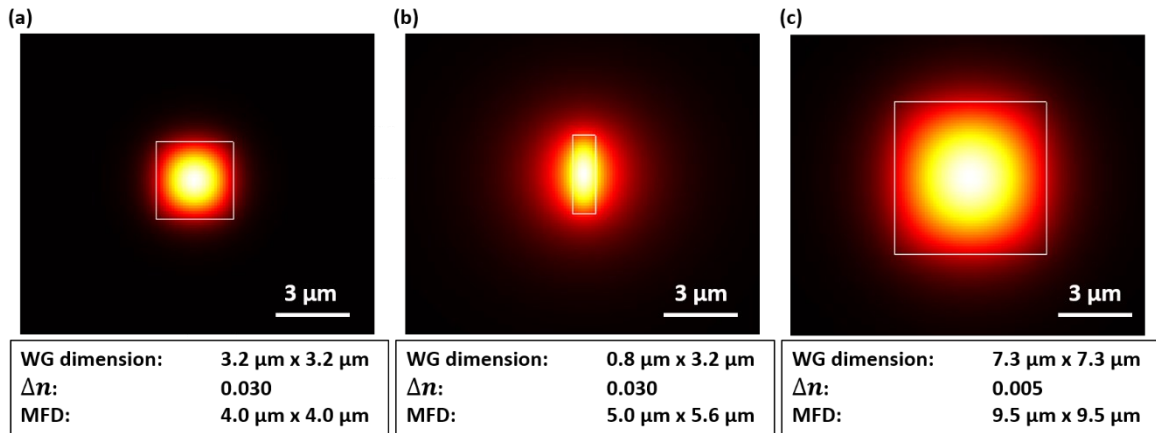


Figure III-1: Simulated mode field diameters (MFD, $1/e^2$) of three waveguide geometries and their corresponding waveguide (WG) dimension at 1550 nm.

The mode field diameters, calculated as $1/e^2$ values, for different geometries range between $4 \mu\text{m} \times 4 \mu\text{m}$ for the $\Delta n = 0.030$ waveguide without taper and $9.5 \mu\text{m} \times 9.5 \mu\text{m}$ for $\Delta n = 0.005$. The latter one being close to the MFD of a standard single-mode fiber with a MFD of $10.4 \mu\text{m}$. A $0.8 \mu\text{m}$ inversely tapered waveguide enlarges the MFD of the $\Delta n = 0.030$ waveguide to $5.0 \mu\text{m} \times 5.6 \mu\text{m}$. Since larger mode field diameters increase the alignment tolerances, the inversely tapered waveguide is used for the $\Delta n = 0.030$ material system instead of the non-tapered waveguide for the following coupling calculations.

B. Simulation of on-chip free-space sections

The on-chip free-space section comprises an input waveguide coupled to a GRIN lens followed by the free-space section to insert optical bulk crystals. Finally, a second GRIN lens couples the light back into the output waveguide. Based on the Gaussian beam propagation with ABCD matrices and overlap integrals introduced in II.B, it is possible to calculate the coupling loss of the on-chip free-

space section for incident optical modes of the polymer waveguides calculated in the previous section. For waveguides with high confinement ($\Delta n = 0.030$), the materials to be inserted are Faraday rotators ($n = 2.31$) with polarization filters for optical isolators or Faraday rotators with HWPs for optical circulators. These waveguides offer the smallest bend radii and other optical functionalities like tunable DBR lasers that will be co-integrated within this work. On the other hand, low confinement waveguides with $\Delta n = 0.005$ offer a better coupling efficiency to single-mode fibers, beneficial to increase the conversion efficiency of SHG. Thus, it is used to integrate ppLN crystals with a refractive index of $n = 2.21$ at 1550 nm. In the analysis, the free-space section length and input/output GRIN lens lengths (with equal lengths for both lenses) are varied to calculate the coupling efficiency. As listed in Table II-1, there are two different GRIN lenses with a numerical aperture of 0.14 and 0.24 available. Since $\Delta n = 0.030$ waveguides have a small mode field diameter and a large beam divergence at the waveguide facet, they are combined with the $NA = 0.24$ GRIN lenses of a larger acceptance angle. Accordingly, the $\Delta n = 0.005$ waveguides will be paired with the $NA = 0.14$ GRIN lenses due to the smaller beam divergence. All optical crystals within this work have an anti-reflective coating and the effective refractive index of the GRIN lenses matches very well with the polymer waveguides and the index-matching glue used to fix the crystal and the lenses. Thus, all losses due to Fresnel reflection and also material absorption are neglected within this chapter. The latter will be discussed later within the analysis of the different PICs.

The coupling efficiency of nonreciprocal elements

The results for integrating RIG crystals (Faraday rotators) are shown as a color-coded two-dimensional coupling efficiency plot in Figure III-2, with the GRIN lens length variation on the y-scale and the RIG crystal length on the x-scale.

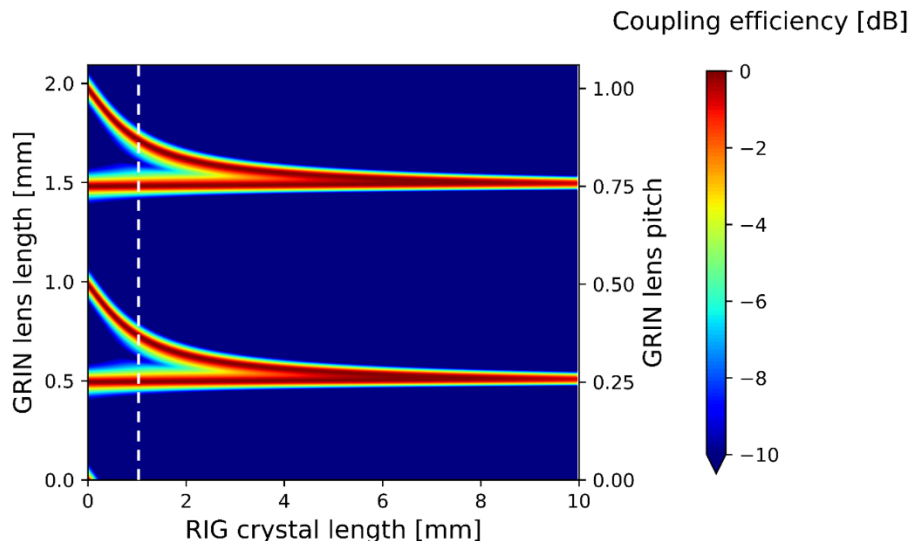


Figure III-2: Simulated 2D coupling efficiency for a RIG crystal inside a free-space section with variation of the RIG crystal and GRIN lens length. The dashed line represents the cross-section from Figure III-3, corresponding to a RIG crystal with a length of 1 mm.

There are four solutions for maximum coupling efficiency at low crystal lengths that converge into two for increasing crystal lengths. For a crystal length of 0 mm (GRIN lens back to back coupling), these correspond to the GRIN lens pitches 0.25, 0.5, 0.75 and 1, introduced in II.B.2. For even longer GRIN lens lengths, this pattern would repeat with the optical beam oscillating over an increasing number of sinusoidal periods inside the GRIN lens. The upper branch of the bifurcation corresponds to an intensely focused beam that results in a beam waist with high confinement. For increasing

free-space lengths, the ability to strongly focus the beam together with a good coupling efficiency decreases, and the upper and lower branch converge into a solution for a nearly collimated beam. In theory, free-space sections with a length of up to 10 mm with a coupling efficiency below 1 dB can be achieved for perfect alignment in this material system. This coupling efficiency is achieved for a GRIN lens length of 520 μm . It is mainly limited by the beam divergence and an increasing curvature (or phase mismatch) of the Gaussian beam at the coupling interface back into the polymer waveguide. For comparison, the coupling efficiency in the lower-left corner of Figure III-2 corresponds to a free-space section without lenses that can be used to integrate thin-film filters up to a length of $\sim 19 \mu\text{m}$ for coupling loss below 1 dB. For the integration of RIG materials, only collimated free-space sections are of interest. In contrast to focused beams, one GRIN lens length corresponding to a pitch slightly larger than 0.25 can cover a large variety of different free-space section lengths in collimated beams. A core application for the RIG material is the integration of optical free-space isolators with a total length of $\sim 1 \text{ mm}$. Figure III-3 depicts the coupling efficiency for a fixed free-space length of 1 mm.

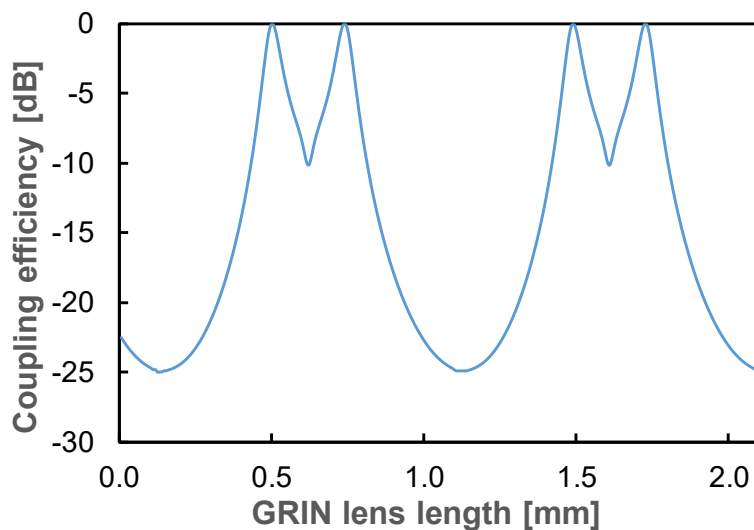


Figure III-3: Coupling efficiency for a 1 mm long free-space isolator crystal depending on the GRIN lens length.

It is noted that the isolator comprises not only the Faraday rotator with a refractive index of 2.31 but also two polarization filters and a HWP with a refractive index of $n \approx 1.5$. Therefore, the results shown in Figure III-3 differ slightly from the 2d map in Figure III-2, where a free-space section filled only with RIG material was assumed. An optimal coupling loss of less than 0.1 dB is achieved for GRIN lens lengths of 500 μm for lenses with a numerical aperture of $NA = 0.24$. This corresponds to a pitch slightly larger than 0.25. Within $\pm 15 \mu\text{m}$ fabrication tolerances of the GRIN lenses, the coupling loss is less than 1 dB.

The coupling efficiency of nonlinear elements

Similar to Figure III-2, the coupling efficiency for a SHG free-space section filled with MgO:LN ($n = 2.13$) depending on the GRIN lens length and the free-space section length is depicted in Figure III-4. Here, a refractive index difference of $\Delta n = 0.005$, and MFDs of 9.4 μm were set for the polymer waveguides at 1550 nm and a $NA = 0.14$ was chosen for the GRIN lenses.

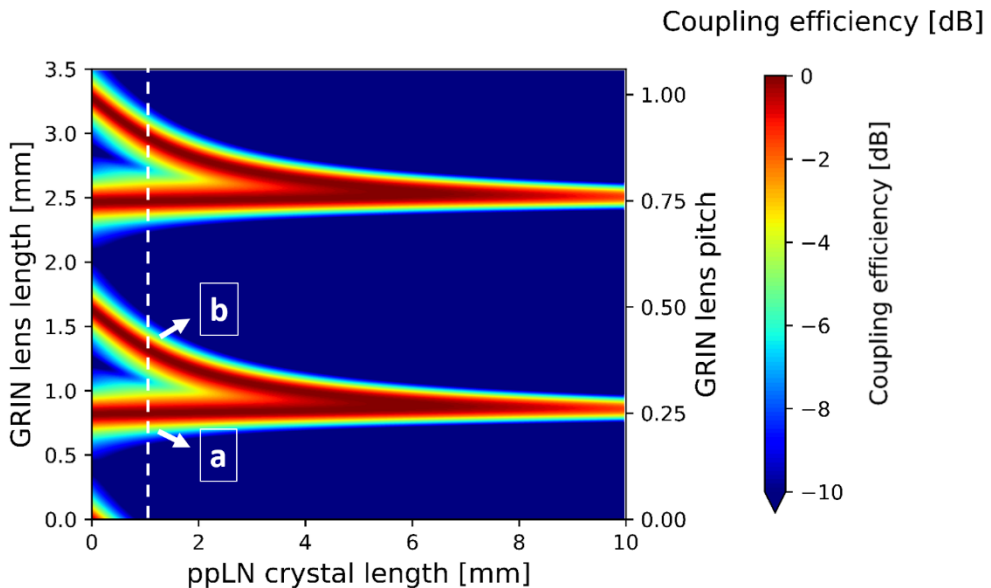


Figure III-4: Simulated 2D coupling efficiency for a ppLN crystal inside a free-space section with a variation of the ppLN crystal and GRIN lens length. The dashed line represents the cross-section from Figure III-5, and the highlighted positions (a) and (b) are depicted as a radial intensity distribution in Figure III-6.

Free-space sections up to a length of 8.2 mm can be covered with loss below 1 dB, according to Figure III-4. This value is slightly smaller than for the previously simulated free-space section in Figure III-2, where more than 10 mm with less than a dB of loss could be bridged. This is due to the slightly larger beam waist of 42 μm that is created by the $NA = 0.24$ GRIN lenses compared to the 38 μm of the $NA = 0.14$ GRIN lenses. According to Equation (II-17), a larger beam waist reduces the beam divergence, which is the limiting factor of the theoretical maximum of achievable lengths of free-space sections. Furthermore, for the RIG material the beam divergence is additionally reduced by the slightly higher refractive index compared to lithium niobate.

For a fixed crystal length of 1 mm, the GRIN lens length is plotted in Figure III-5. Most efficient coupling is achieved for GRIN lens lengths of 840 μm with less than 0.1 dB loss and a 1 dB loss fabrication tolerance of $\pm 30 \mu\text{m}$ for a collimated beam. For a focusing beam, equally good coupling efficiencies can be achieved for a GRIN lens length of 1330 μm within the same fabrication tolerances.

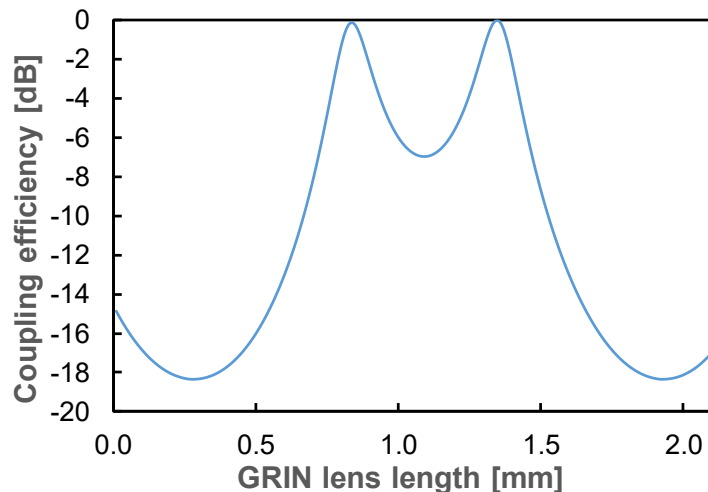


Figure III-5: Coupling efficiency for a 1 mm long ppLN crystal depending on the GRIN lens length.

Simulation

The two solutions for a 1 mm ppLN crystal, highlighted in Figure III-4, are depicted as cross-sectional intensity distributions in Figure III-5. The collimated beam has a 38 μm beam waist inside the free-space section, while the focusing lenses create a beam waist of 6 μm . The latter beam waist corresponds to a confocal parameter of 150 μm and a 3.3 ratio from crystal length to confocal parameter close to the Boyd Kleinman condition of 2.84 introduced in II.D.3.

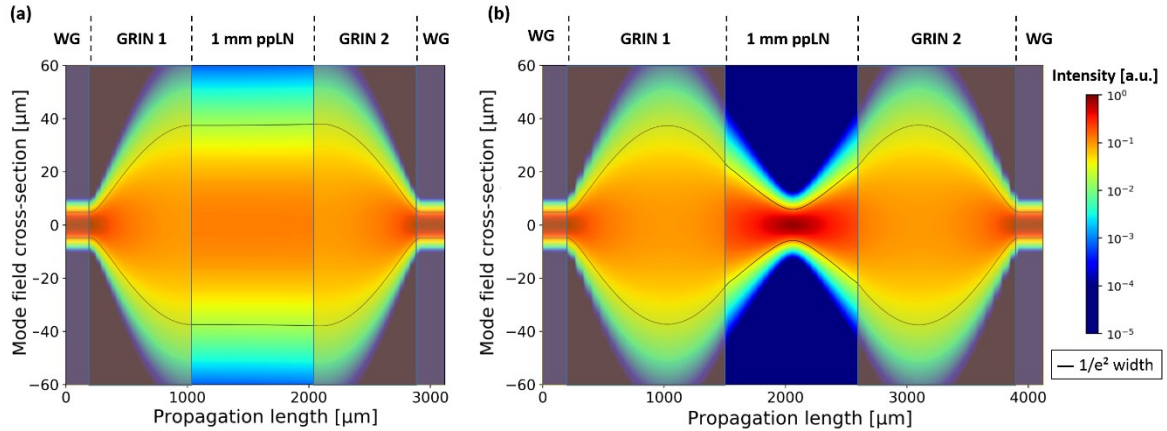


Figure III-6: Radial intensity distribution for a free-space length of 1 mm with ppLN crystal inserted and a GRIN lens length of 840 μm (a) and 1330 μm (b) at a wavelength of 1550 nm, corresponding to the parameter combinations [a] and [b] in Figure III-4.

The coupling efficiencies calculated in Figure III-4 and Figure III-5 correspond to the coupling efficiency at 1550 nm that describes the general behavior of the free-space section. However, for SHG the coupling efficiency of the second harmonic back into the waveguide is crucial. As described in section II.D.3, the waist of the second harmonic is related to the pump beam by $\omega_{\text{pump}} = \sqrt{2}\omega_{\text{SH}}$ with matching phase fronts. Starting from the SH created in the free-space section, this enables the calculation of the coupling efficiency back into the waveguide similar to the previous analyses. Since the polymer waveguides are single-mode and thus the Gaussian pump beam is in the fundamental TEM_{00} mode, the created SH is also created in the TEM_{00} mode. However the output polymer waveguide designed for 1550 nm is multimode at 775 nm. Thus, the SH can also couple in higher-order modes. The simulated coupling efficiency into the two fundamental modes of the waveguide at 775 nm is less than 0.1 dB for both the collimated and the focusing beam, yielding a similar loss than for 1550 nm. Due to dispersion, the 0.25 pitch length of the GRIN lenses is slightly longer at lower wavelengths, requiring 5 μm longer lenses from 1550 nm down to 775 nm. Still, this effect is negligible and within the fabrication tolerances of the GRIN lenses.

Alignment offsets for on-chip free-space sections

The previous two simulation sections are based on paraxial Gaussian beam transmissions that enable the calculation of coupling efficiencies with only little complexity involved. This covers the case of perfect alignment and no consideration of interface reflections. The latter can be neglected because all interfaces are covered with index-matching glue, and interfaces with a high refractive index (the nonlinear and nonreciprocal materials) are coated with an anti-reflection coating. However, alignment tolerances are still critical. The GRIN lenses fabricated from a GRIN fiber exhibit an intrinsic core to cladding offset, and also the polymer U-grooves have a depth variation across the fabricated wafers. To determine the alignment tolerances, simulations with Zemax's physical optics propagation method using the underlying methods described in [81], were carried out. The results are depicted in Figure III-7. Simulations include an offset corresponding to a U-groove that was etched too deep or too shallow and a rotational tilt along the input facet of the output lens.

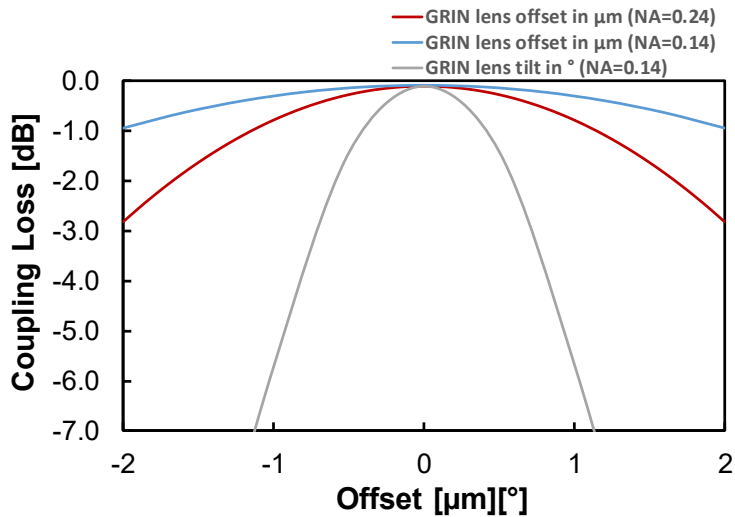


Figure III-7: Simulation of a GRIN lens alignment offset that corresponds to a U-groove that was etched too deep or too shallow for a numerical aperture of 0.24 with $\Delta n = 0.030$ waveguides (red curve) and $NA = 0.14$ GRIN lenses with $\Delta n = 0.005$ waveguides (blue curve). Additionally, a tilt of the output GRIN lens was simulated for $\Delta n = 0.005$ GRIN lenses (grey).

For a numerical aperture of 0.24, and $\Delta n = 0.030$ polymer waveguides, coupling losses of 0.8 dB within a vertical offset of $\pm 1 \mu\text{m}$ are achievable compared to the 0.1 dB for a zero offset. In comparison, $\Delta n = 0.005$ waveguides with $NA = 0.14$ GRIN lenses and a $\pm 1 \mu\text{m}$ tolerance yield coupling losses of 0.4 dB. The higher alignment tolerances of the $NA = 0.14$ lenses result from the larger mode field diameter of 9.5 μm of the $\Delta n = 0.005$ compared to the $\Delta n = 0.030$ waveguides with a MFD of 4.0 μm . An angular offset of $\pm 1^\circ$ with respect to the optical axis corresponds to a coupling loss of 6 dB. Even though a tilt offset of $\pm 1^\circ$ is much more critical than a vertical offset of $\pm 1 \mu\text{m}$, a rotational offset of the GRIN lenses can be reduced and neglected since the bottom surface of the U-grooves are used to align the GRIN lenses parallel to the polymer waveguides with a negligible rotational error.

IV. Fabrication

The hybrid integration platform PolyBoard was already briefly introduced in II.A, where an overview of the platform's different optical functionalities was given. The first part of this chapter will provide an overview of the technical aspects of the PolyBoard and the waveguide and U-groove fabrication methods. Since the fabrication of both waveguides and U-grooves that hold the GRIN lenses used for the on-chip free-space sections were already established prior to this work, these aspects will be covered only in short detail. Besides free-space sections, other optical functionalities used in this work include thin-film filter slots for the insertion of polarization beam splitters, thermo-optic components like variable optical attenuators, phase shifters, and a tunable DBR laser that will also be described briefly. The second part of this chapter elaborates on the fabrication of GRIN lenses from a graded-index fiber established within this work. Lastly, the preparation of suitable materials for the on-chip free-space section is described. This includes the bonding process of free-space isolators and Faraday rotators plus half-wave plates and preparation of the ppLN crystals for SHG.

A. The PolyBoard

The PolyBoard is a hybrid integration platform that comprises polymer waveguides with a higher refractive index material embedded in a cladding polymer with a low refractive index. The standard fabrication process of the PolyBoard includes an electrode layer a few microns beneath the waveguide layer, used for thermo-optic components like tunable gratings, phase shifters, or variable optical attenuators. Additionally, U-grooves and etched slots are used for fiber coupling, creating the on-chip free-space sections and inserting thin-film filters. Overall, the combination of buried electrodes, U-grooves plus filter slots, and waveguides requires a set of five lithographic masks in the fabrication process for the 4" wafer technology. Three masks are required to fabricate the U-grooves and one each for the buried electrodes and the waveguide layer. There are four different core materials and one cladding material available for the waveguide layer, as listed in Table IV-1, commercially available in the ZPU line from ChemOptics Inc.

Table IV-1: Refractive index values for the cladding material, the four different core materials and the corresponding refractive index difference between core and cladding at 1550 nm. The standard waveguide geometries for single-mode waveguides at 1550 nm and their corresponding (Gaussian $1/e^2$) mode field diameter are listed below.

	$n_{cladding}$	$n_{core005}$	$n_{core011}$	$n_{core020}$	$n_{core030}$
n	1.45	1.455	1.461	1.470	1.480
Δn	-	0.005	0.011	0.020	0.030
Cross-section	-	$7.3 \times 7.3 \mu\text{m}^2$	$6.0 \times 6.0 \mu\text{m}^2$	$3.5 \times 3.5 \mu\text{m}^2$	$3.2 \times 3.2 \mu\text{m}^2$
MFD	-	$9.5 \times 9.5 \mu\text{m}^2$	$7.2 \times 7.2 \mu\text{m}^2$	$4.7 \times 4.7 \mu\text{m}^2$	$4.0 \times 4.0 \mu\text{m}^2$
Bend radius		14.0 mm	4.0 mm	3.0 mm	1.3 mm

Depending on the application, there are waveguides with a refractive index difference between 0.005 and 0.03 available. The refractive index $\Delta n = 0.005$ offers large mode field diameters that match the MFD of SMFs very well and allow fiber coupling with low loss ($\Delta n = 0.005$) down to 0.2 dB per interface. While the $\Delta n = 0.005$ material system does not allow any waveguide bends due to high waveguide bending loss, the $\Delta n = 0.030$ material system is most versatile in its applications. It offers the smallest bends in the PolyBoard platform at the cost of higher fiber coupling and thin-film filter loss due to the smaller waveguide mode field diameters. The two other refractive indexes offer a trade-off between the two mentioned ones, and they are of particular interest for smaller wavelengths since the waveguide width for single-mode condition scales with the wavelength [45]. Thus, structures at low wavelengths get increasingly small and challenging to fabricate in $\Delta n = 0.030$.

As already mentioned, $\Delta n = 0.030$ is the material system of choice for the integration of nonreciprocal elements since it also offers the co-integration of other functionalities like a tunable laser or waveguide bends required for the circulator. In contrast, $\Delta n = 0.005$ offers low fiber coupling loss beneficial for high conversion efficiencies in nonlinear optics.

1. Waveguide fabrication

For the waveguide fabrication, polymer layers are deposited as liquid resin with a spin coater, and subsequently UV cured and hard-baked. After deposition of the bottom cladding, the waveguide layer polymer is deposited, etched to the thickness according to Table IV-1, and structured with a photolithographic process. Waveguide patterning involves the deposition of a titanium mask and reactive ion etching of the waveguide structures. After removal of the Ti mask, a top cladding is deposited, resulting in buried polymer waveguides. A schematic fabrication process of the waveguides is shown in Figure IV-1.

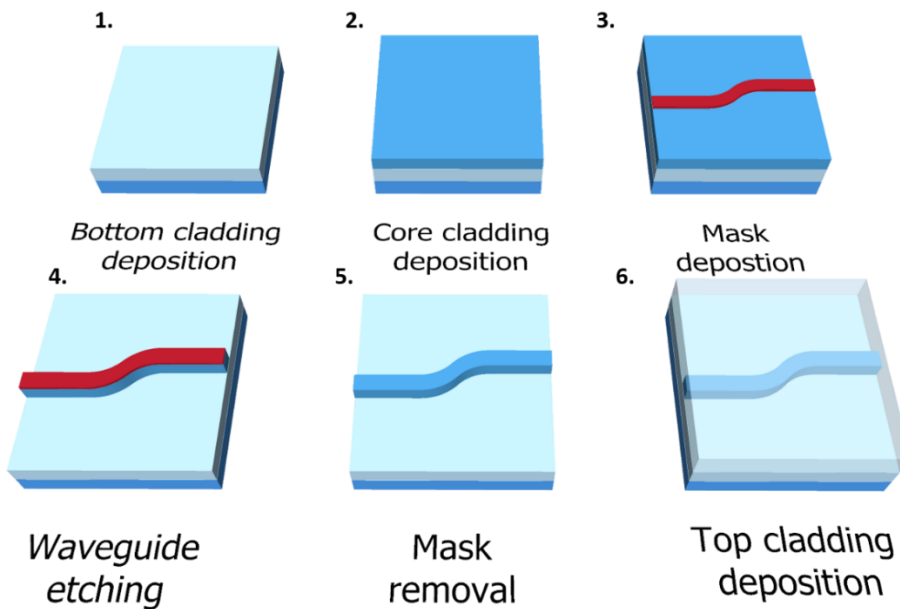


Figure IV-1: Waveguide fabrication process of the PolyBoard. First, the bottom cladding and core material are deposited (1. and 2.). After structuring the waveguides with a Ti mask and reactive ion etching (3. And 4.), the Ti mask is removed, and the top cladding is deposited.

2. U-groove fabrication and GRIN lens alignment

U-groove fabrication requires three additional photolithographic steps besides the waveguide lithography. It comprises a supporting surface at the bottom designed to level the GRIN lens center with the waveguide center; thus, the height difference between the bottom surface and the waveguide center is 62.5 μm . Two etched sidewalls with a distance slightly smaller than the 125 μm GRIN lens diameter are used to clamp and fix the lens in the lateral dimension. The schematic layout of a fabricated U-groove and a picture of a U-groove cross-section are depicted in Figure IV-2.

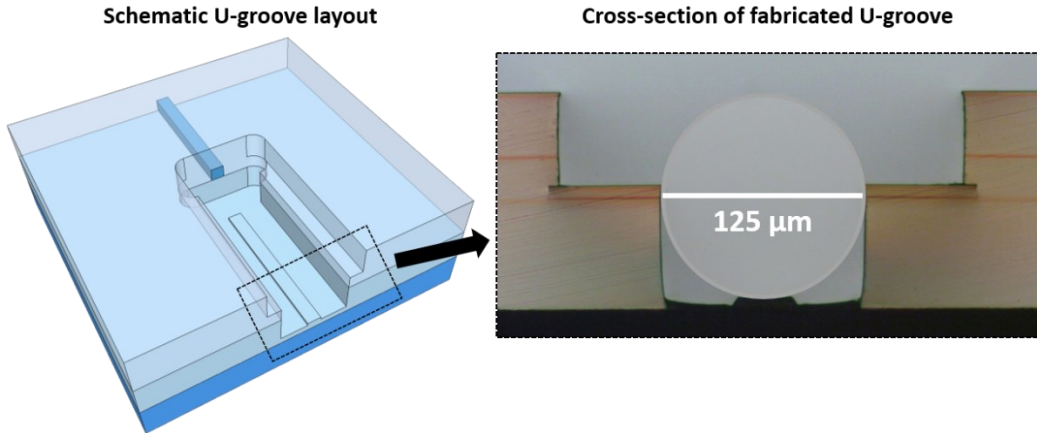


Figure IV-2: Schematic layout of a U-groove to insert GRIN lenses and single-mode fibers (left). Right: cross-section of a fabricated U-groove with an indicated position of a GRIN lens.

Insertion and alignment of the GRIN lenses inside the U-grooves is done with a tweezer under an optical microscope. The U-grooves provide the horizontal and vertical precision that the GRIN lenses are coupled to the waveguides when the lenses are aligned with the U-grooves' bottom surface, which can be achieved by applying a small amount of force on the lenses. Application of this force is possible with a micromanipulator during an active alignment where the transmitted signal is maximized if the lenses are aligned correctly in the U-groove. In general however, the pre-alignment under the microscope is sufficient, and the additional micromanipulator adjustment is not required, enabling a passive alignment of the lenses. Nonlinear crystals are inserted parallel to the etched edges inside the free-space section, while optical isolators are rotated by a 4° angle to increase the optical isolation. Alignment of the optical materials is also done with a micromanipulator. After the alignment, all components are fixed with a UV curing glue with a refractive index of 1.46 at 1550 nm, close to the effective index of the polymer waveguides and the GRIN lenses.

3. Additional optical functionalities

Besides the U-grooves used for GRIN lens alignment and the integration of optical crystals and waveguides, several other building blocks are required. This includes thin-film filters to integrate polarization beam splitters for the PBS circulator, phase shifters and optical attenuators for the MZI circulator, and a tunable DBR laser for the co-integration with the optical isolator. All additional building blocks will be covered in short detail within this section.

Thin-film filters

Collimated on-chip free-space sections can span up to a few millimeters with the help of GRIN lenses according to the results from chapter III. However, it is also possible to create small slots with unguided free-space sections to insert thin-film filters. Due to the lack of collimating optics, the slots are limited to the width of a few microns without significantly increasing loss due to an increasing beam divergence. This is also shown in Figure III-2 and Figure III-4 of chapter III and indicated by the bright part in the lower-left corner of both plots: when no lenses are used, free-space sections of up to 20 μm can still be bridged with propagation loss of around 1.1 dB for $\Delta n = 0.030$ waveguides. The TFF slots are etched inside the polymer waveguides similar to the deep etching process of the U-grooves, and are used to insert thin-film filters for spectral and polarization filtering or polarization rotation. The polarization can be rotated with commercially available HWPs based on birefringent polyimide films. Filtering of polarization and wavelength is done with thin-film filters that consist of dielectric layer stacks deposited on a polymer film. Typical polymer layers for TFFs are 4 μm thick, with a 8.3 μm thick layer stack of up to a few hundred alternating layers of

Fabrication

SiO_2 and TiO_2 . The layer design and deposition is done at the Laserzentrum Hannover. After deposition, the filters are cut into smaller pieces and removed from the substrate, ready to be inserted into the filter slot. Figure IV-3 depicts a schematic layout of a PBS slot with inserted filter.

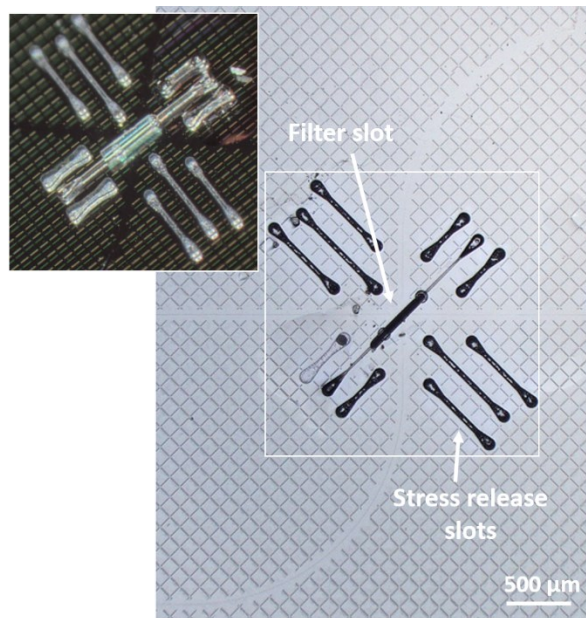


Figure IV-3: Assembled polarization beam splitter thin-film filter in an etched PolyBoard slot with two input and two output ports.

Electrode layers for thermo-optic elements

The polymers used for waveguide fabrication have a thermo-optic coefficient of $-10^{-4}/\text{K}$, meaning that the effective refractive index of the waveguides is temperature-dependent. This can be used to build thermo-optic components ranging from simple phase shifters and MMI-based variable optical attenuators to Y-branch switches or tunable Bragg-gratings. Thermal energy is deployed with buried Au/Ti electrodes beneath the waveguide layer. The phase shifter electrode is placed beneath the waveguide, as depicted on the right-hand side in Figure IV-4. Two air trenches are placed next to the waveguide and the electrode to increase the thermal isolation, enhancing the heater efficiency.

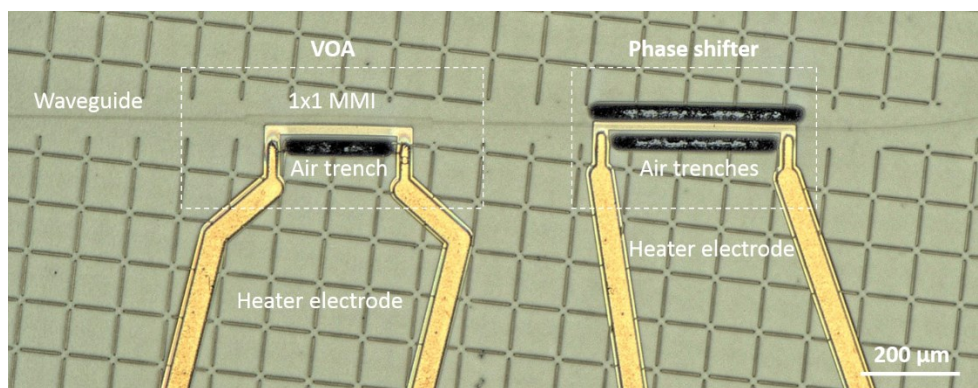


Figure IV-4: Micrograph of a variable optical attenuator consisting of a 1x1 MMI with a buried heater electrode (left) and a phase shifter (right).

For a phase shifter length of 400 μm, a temperature increase of $\sim 28 \text{ K}$ is required for a phase shift of π . This temperature increase is achieved for electrical currents of 10 mA in the electrode. The

Fabrication

optical attenuator consists of a 1×1 MMI with a buried electrode that has an offset to the center of the MMI. Heating induces an asymmetric refractive index distribution inside the multimode interference section that gradually increases the coupling loss back into the single-mode depending on the temperature as described in [82]. The right part of Figure IV-4 depicts a VOA consisting of a 1×1 MMI with the buried heating electrode. Peak attenuations that can be achieved with the VOAs are 19 dB for an applied current of 37.5 mA.

Tunable DBR laser

One of the most used PolyBoard building blocks is a hybrid integrated tunable distributed Bragg-reflector laser consisting of an active indium phosphide gain section, coupled to a polymer waveguide with integrated phase shifter and a tunable Bragg grating. Figure IV-5 depicts a schematic layout of the tunable DBR laser together with a micrograph of a fabricated device. The InP-waveguide is butt-coupled to the polymer chip with an AR coating against polymer at the InP waveguide facet. Angled waveguides between polymer and InP additionally reduce any back reflections that might occur at the coupling interface. The optical cavity of the laser is formed by a broadband high-reflective (HR) coating at the rear facet of the InP gain element and a corrugated waveguide Bragg grating on the polymer side. The Bragg grating acts as a wavelength selective mirror that only reflects a narrow linewidth of the broad gain spectrum as depicted in Figure IV-5c. Similar to the phase shifter design, a heater electrode enables tuning of the Bragg grating which enables the selection of different longitudinal modes of the laser cavity and therefore wavelength tuning. The phase shifter additionally enables tuning of the longitudinal modes inside the cavity, which improves the side mode suppression ratio and allows fine tuning of the laser wavelength.

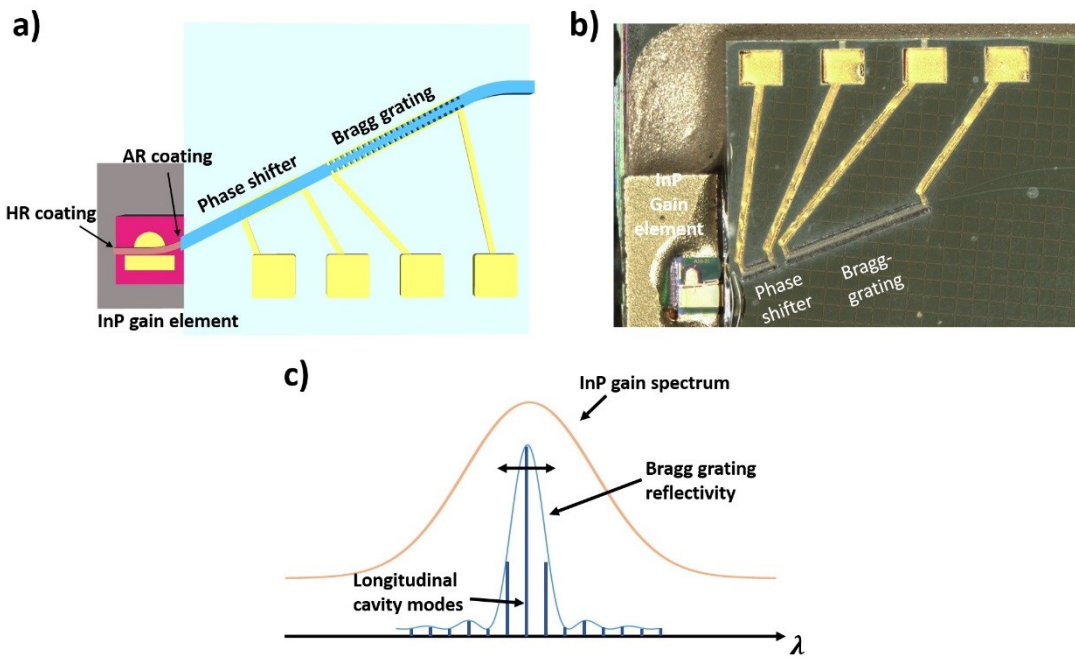


Figure IV-5: Schematic layout of the DBR laser comprising an InP gain element with high-reflective (HR) coated back facet and anti-reflective (AR) coated front facet coupled to a polymer chip consisting of a thermo-optic phase shifter and Bragg grating. The fabricated device is depicted in b) with the working principle explained in c) as described in the text.

The reflectivity of the Bragg grating is around 25 % and typically output powers of a few milliwatts can be achieved with this laser design, depending on the gain element size. The standard tuning range is 20 nm for a linewidth of a few hundred kilohertz. Overall, the tunable DBR laser is a complex building block that is covered only in short detail within this work. More about the general

working principle, applications and different design variations can be found in [83]. Within this work the DBR laser will be integrated together with the isolator.

B. GRIN lens fabrication

Typical applications for commercially available GRIN lenses include fiber coupling of laser diodes and photodetectors, fiber-to-fiber coupling or fiber collimators [84, 85], and endomicroscopic applications [86]. The diameters of GRIN lenses for these primarily fiber-based applications are in the range of 1 mm – 2 mm, and the smallest commercially available diameters range down to 250 µm. However, this is still two times as large as the diameter of a SMF and the diameter of the PolyBoard U-grooves. In principle, it would be possible to use GRIN lenses with a 250 µm diameter, but this would require a significant amount of technology development in the PolyBoard fabrication process regarding the co-integration of two differently sized U-grooves for SMFs and GRIN lenses. Since there are no commercially available GRIN lenses that fit the already existing SMF U-grooves with a diameter of 125 µm, a fabrication process for GRIN lenses was developed within this work. The fabrication is based on a lapping and polishing process of graded-index fiber pieces shortened to the required length and subsequently polished on both facet sides. A schematic of the fabrication process is shown in Figure IV-6.

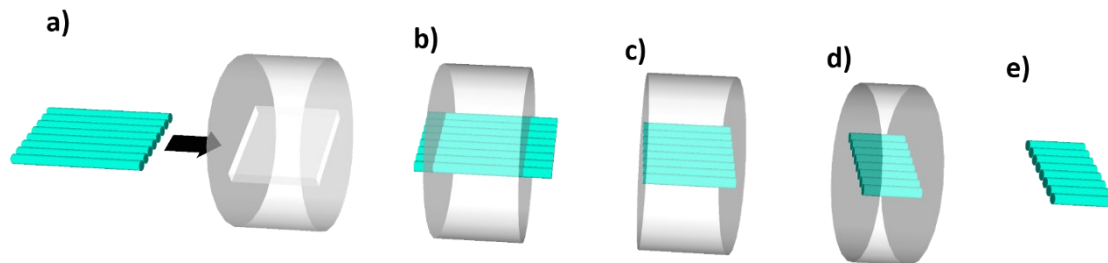


Figure IV-6: Schematic fabrication process of the GRIN lenses. After insertion and fixation in a 3d printed mold (a) and (b)), the lenses are shortened to the targeted length and polished on both sides (c) and d)). As a final step, the lenses are removed from the 3d mold, separated, and cleaned (e).

The fabrication process is as follows: a batch of a few hundred GRIN fiber pieces is fixed and glued in a 3d printed mold. The mold facets are then parallelized in an Al_2O_3 lapping process, and the GRIN facets of the first side are polished with a diamond suspension ranging from 1 µm down to 0.1 µm diamond grain size. Afterwards, the mold is fixed on a carrier with the polished side facing towards the carrier. Following the simulations of chapter III, the batch of GRIN fibers is shortened to the required length and the second facet side is polished. An optional anti- or high-reflective coating can be applied to the block at this stage. Generally, this is not required since the refractive index of the lenses matches very well with the polymer waveguides and the index-matching glue. The final block is then resolved in acetone to remove the lenses from the mold, and the lenses are ready for usage after final cleaning in a ultrasonic bath. GRIN lens facets after the final polishing step and a mold with an array of polished lenses and applied high reflective coating is depicted in Figure V-14.

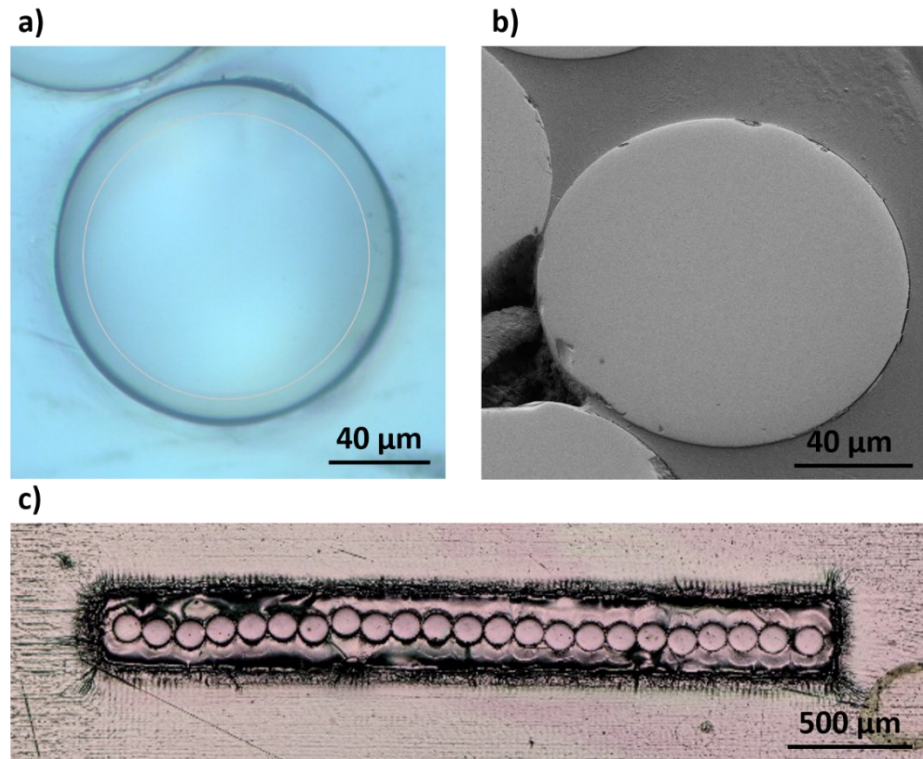


Figure IV-7: a) Microscopic image of a GRIN lens facet after the final polishing step with highlighted interface between core and cladding. b) Scanning electron microscope image of a polished GRIN lens facet. c) 3D printed slot with an array of high-reflective coated GRIN lenses.

Three different types of GRIN lenses are used in this work. For the GRIN lenses with a numerical aperture of 0.24 used for the $\Delta n = 0.030$ waveguides, the targeted length is 500 μm . For the $\Delta n = 0.005$ waveguides, the targeted GRIN lens length of the $NA = 0.14$ lenses is 840 μm for the collimating lenses and 1330 μm for the focusing lenses. Figure IV-8 depicts a lens from each batch with a length scale. The length of the 500 μm and 840 μm lenses is well within the targeted length specifications with $500 \mu\text{m} \pm 10 \mu\text{m}$ and $840 \mu\text{m} \pm 10 \mu\text{m}$. Due to a measurement error, the 1330 μm lenses are slightly shorter than targeted with an average value of $1285 \mu\text{m} \pm 20 \mu\text{m}$.

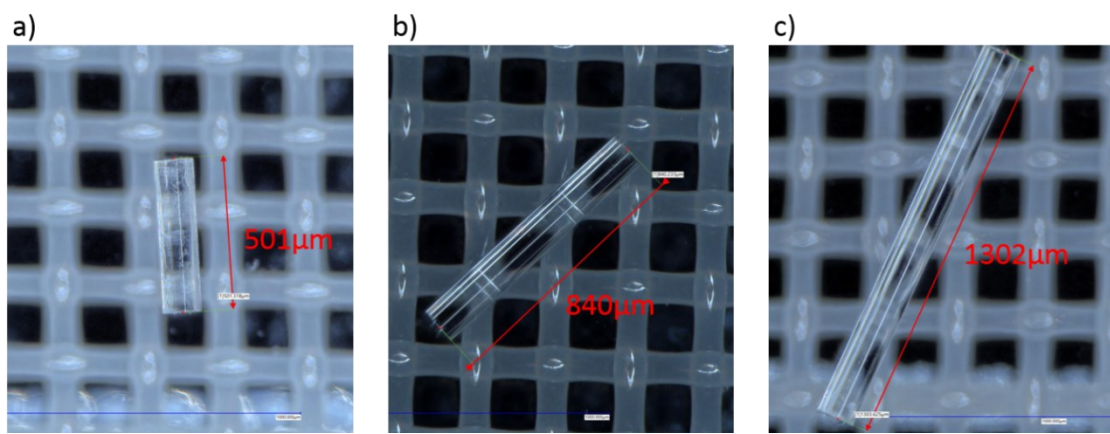


Figure IV-8: Fabricated GRIN lenses from each batch. (a) targeted 500 μm GRIN lens length with $NA = 0.24$, (b) targeted GRIN lens length of 840 μm with $NA = 0.14$, (c) targeted GRIN lens length of 1330 μm with $NA = 0.14$.

C. Preparation of nonreciprocal and nonlinear materials

The optical crystals to be integrated include nonreciprocal materials for optical isolators and circulators and nonlinear materials for SHG. All materials to be integrated are commercially available, and the requirements include:

- Small footprint: the length of materials in the free-space section is limited to materials with a maximum optical transmission length of 5-10 mm in accordance with the simulation results in III.B.
- Low insertion loss: the integration of on-chip free-space sections with low loss (<<1 dB) offers an easy integration method for optical materials. In order to keep the advantage over other integration methods, e.g. bonding of magneto-optic materials in silicon photonics, the optical materials also require low loss in terms of material absorption.
- Entirely usable material aperture: the GRIN lenses are fixed and aligned on the supporting surface of the U-grooves that also support inserted crystals. Therefore, the optical beam transmits the inserted material at the lower edge of the aperture. This requires total magnetization in the whole magneto-optic material, including the crystal edges close to the surface, and periodic poling of nonlinear crystals covering the entire transmittable aperture. Furthermore, diced materials require low chipping at the edges.

1. Nonreciprocal elements

The Faraday rotators required for optical isolators and circulators are bismuth-doped rare earth iron garnets as described in II.C, commercially available by II-VI Inc. They exhibit a strong Faraday effect that achieves a 45° polarization rotation at a thickness of 485 µm without the requirement of an external magnet and low insertion loss of <0.05 dB. To reduce back reflections and transmission loss, they are anti-reflection (AR) coated against polymer on both sides. In optical isolators, these are paired with polarization filters from Codixx AG with a thickness of ~220 µm and intrinsic insertion loss of <0.2 dB. The polarization filters provide a polarization extinction ratio of >40 dB that matches the <0.5° error of Faraday rotation provided by the Faraday rotators to achieve an overall optical isolation of >40 dB. To maintain TE polarization after isolator transmission in forward direction, an additional half-wave plate with a thickness of 91 µm is bonded at the output side of the isolator. Both the polarization filters and the HWPs refractive index match the refractive index of the polymer waveguides and thus need no AR coating. This sums up to a total thickness of ~1000 µm and overall insertion loss of 0.4 dB for the optical isolator. Integrated circulators require a Faraday rotator bonded to a HWP without the need for polarization filters. All components are bonded together as 11 x 11 mm² slabs and diced into smaller pieces as depicted in Figure IV-9 for the free-space isolator. With a 10 x 10 dicing grid and a 0.2 mm thick dicing blade, every bonded slab yields 121 isolators with an aperture of 0.9 mm x 0.9 mm. Chipping at the edges is within 10 – 15 µm, which is well outside the beam aperture of the GRIN lenses.

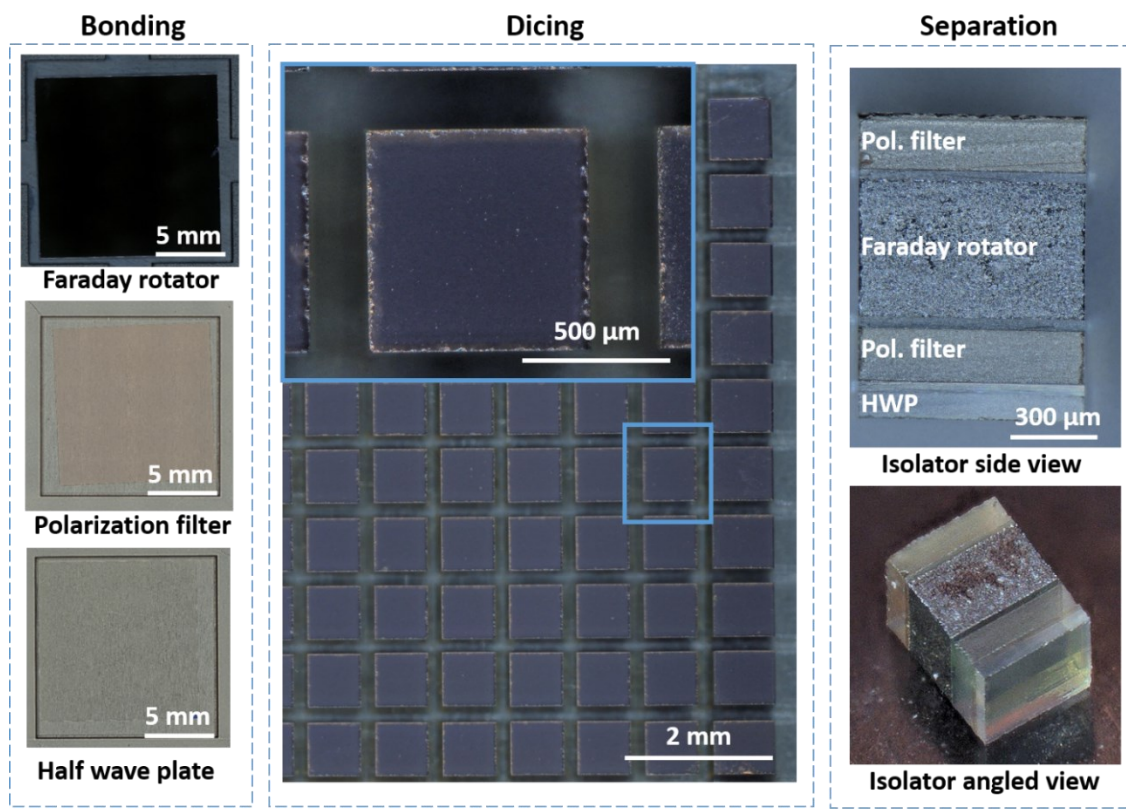


Figure IV-9: Left: $11 \times 11 \text{ mm}^2$ Faraday rotators, polarization filters, and half-wave plates. Center: bonded and diced free-space isolators. Right: cross-section and side view of an isolator.

2. Nonlinear elements

Periodically poled lithium niobate crystals for SHG with a length of 1 mm are purchased from Coversion Ltd, AR coated against polymer and diced into smaller pieces as depicted in Figure IV-10. In contrast to the nonreciprocal elements, one purchased crystal only yields three separated crystals for the PolyBoard integration. The surface of the ppLN crystals is etched to make the periodic poling with a period length of $19.1 \mu\text{m}$ visible. For type-0 phase matching, the polarization of the pump light must be aligned with the thickness of the crystal, which corresponds to on-chip TM polarization if the poling is visible from the top view.

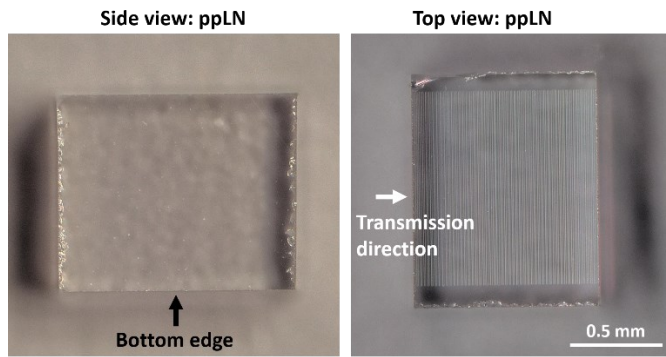


Figure IV-10: Side and top view of a ppLN crystal for the PolyBoard insertion. The side view shows the input facet of the crystal, with almost no visible chipping at the upper and lower crystal edge. In the top view image, the mask used for periodic poling is still visible.

V. Results

The previous chapters described the fundamentals behind the integration of nonreciprocal and nonlinear elements into a polymer photonic integrated circuit, derived optimal free-space section designs for the integration of different materials, and explained the fabrication and preparation techniques for the devices. Overall, four different designs for an isolator, two circulators, and a second-harmonic generation source were proposed in chapter II. Before characterization of these, free-space sections filled with index-matching glue instead of bulk crystals and resonant cavity designs are characterized in section V.A to measure fundamental properties of the on-chip free-space sections. Afterwards, the integrated isolator depicted in Figure II-10 is characterized as a standalone device and co-integrated with a DBR laser (Figure II-11). The optical circulator is fabricated based on the polarization beam splitter design, schematically depicted in Figure II-12, and the Mach-Zehnder interferometric design, as illustrated in Figure II-14. The results are shown in V.C. In V.D, the second-harmonic generation source based on the ppLN integration as depicted in Figure II-18 is characterized.

A. On-chip free-space sections

1. Glue-filled free-space sections

Overview

Three free-space sections with a free-space length of 1 mm are characterized before the insertion of nonlinear or nonreciprocal materials into the on-chip free-space section. This helps to test the fabricated GRIN lenses' quality and verify the theoretical model derived in II.B and III. To avoid back reflections at the GRIN lens facets that would create a Fabry-Pérot resonator, the whole free-space section is filled with index-matching glue. Figure V-1 depicts such a polymer chip with inserted GRIN lenses and applied glue.

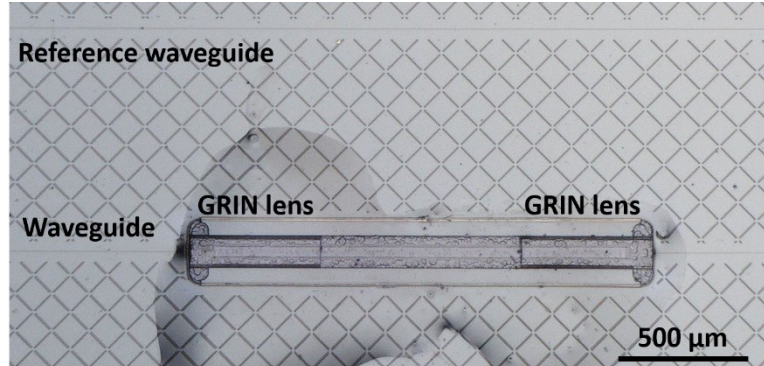


Figure V-1: On-chip free-space section with inserted GRIN lenses filled up with index-matching glue.

The three chips are fabricated in the $\Delta n = 0.030$ refractive index material system equipped with $NA = 0.24$ GRIN lenses.

Measurements

The chip in Figure V-1 is measured with input and output lensed fiber with a spot size diameter of 6 μm . Figure V-2 shows the optical transmission and excess loss measurements for three such free-space sections together with an adjacent reference waveguide. The transmission measurements include fiber-to-chip coupling loss of 1 dB per facet for each input and output coupling interface.

Results

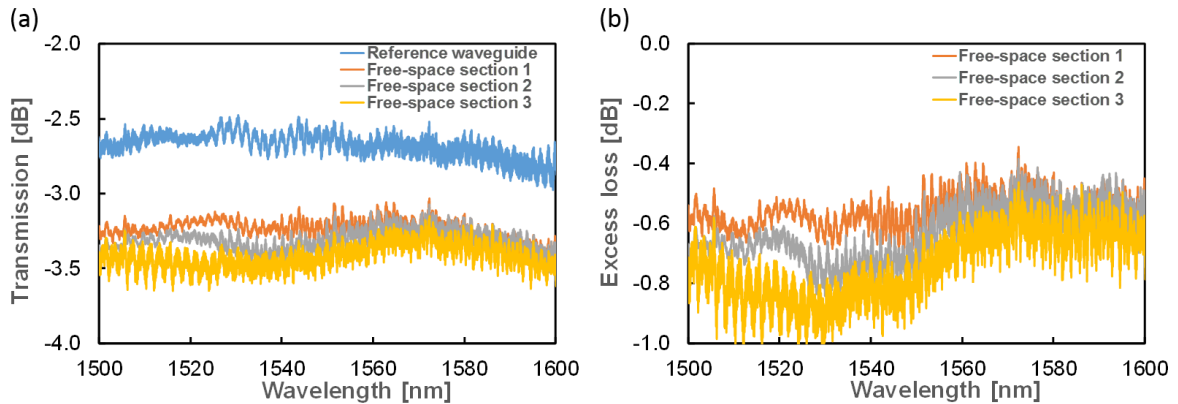


Figure V-2: Optical transmission for three free-space sections with a length of 1 mm and a reference waveguide.

At 1550 nm, insertion loss of $2.6 \text{ dB} \pm 0.1 \text{ dB}$ for the reference waveguide and average loss of $3.3 \text{ dB} \pm 0.2 \text{ dB}$ for the three free-space sections were measured. This corresponds to excess loss of $0.7 \text{ dB} \pm 0.2 \text{ dB}$ with respect to the reference waveguide. The excess loss is obtained by subtracting the insertion loss of the reference waveguides from the insertion loss of the free-space sections. Minimal loss is observed in the range of 1560 nm to 1600 nm with calculated excess loss of $0.6 \text{ dB} \pm 0.2 \text{ dB}$. The spectral oscillations in all measurements are caused by the waveguide-air interfaces from the measurement with lensed fibers that create a weak Fabry-Pérot interferometer.

Discussion

According to the theoretical model in Figure III-7 in III.B, total loss of less than 0.1 dB are calculated for perfectly aligned 500 μm GRIN lenses with a numerical aperture of 0.24 and $\Delta n = 0.030$ waveguides for the on-chip free-space section. This coupling loss simulation includes the GRIN lens-waveguide interfaces and the propagation in the free-space section, but not the absorption loss of the index-matching glue. The glue would add 0.5 dB/mm to the simulated value for a theoretical coupling loss of 0.6 dB. This absorption loss value was provided by Panacol, the distributor of the Vitralit-glue used within this work. The on-chip free-space section measurements in Figure V-2 yield excess loss values of $0.7 \text{ dB} \pm 0.2 \text{ dB}$ at 1550 nm and $0.6 \text{ dB} \pm 0.2 \text{ dB}$ at 1580 nm for a free-space section of 1 mm filled with index-matching glue. In order to compare the excess loss measurement to the simulation, 0.14 dB have to be added to the excess loss values since the reference waveguide measurement is simply subtracted from the insertion loss measurement of the free-space section. Adding 0.14 dB to the excess loss takes into account that the reference waveguide is 2 mm longer than the two waveguides in the optical path of the free-space section with an additional waveguide propagation loss of 0.7 dB/cm. Thus, the measured coupling loss of the free-space section are $0.84 \text{ dB} \pm 0.20 \text{ dB}$ at 1550 nm. This includes the GRIN lens/waveguide interfaces, the propagation in the free-space section, and 0.5 dB absorption loss of the glue. Neglecting all other possible loss sources, e.g. facet defects or imperfections inside the GRIN lenses, the additional loss of $0.24 \pm 0.2 \text{ dB}$ corresponds to a U-groove offset of $0.5 \mu\text{m} \pm 0.2 \mu\text{m}$ that is in good accordance with the etching precision of the U-groove (see Figure III-7). Across a 4" wafer, around 60% of all U-groove depths are within 0.5 μm deviation of the target value. Thus, taking glue absorption and the GRIN lens misalignment due to U-groove-depth-variation into account, the measurements are in good agreement with the theoretical model derived earlier.

2. Fiber-coupled free-space sections

Overview

The second device characterized in this section comprises a U-groove connected to the chip edge without input waveguide. Instead, a standard single-mode fiber is coupled directly to the free-space section as depicted in Figure V-3.

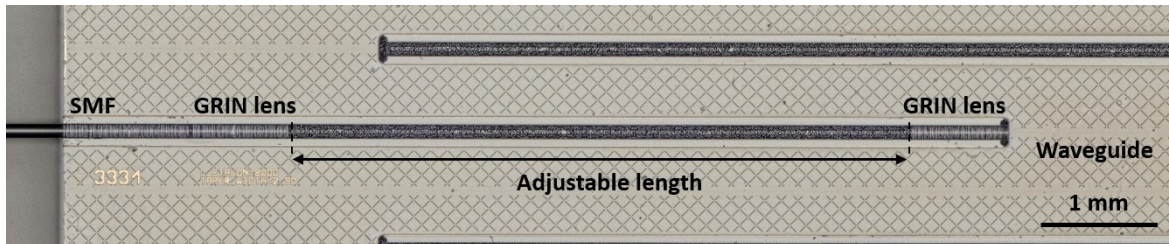


Figure V-3: On-chip free-space section coupled directly to a single-mode fiber (SMF). The length of the free-space section can be varied by pushing the left GRIN further into the free-space section. The image was taken before applying the index-matching glue.

This is also how fiber-to-chip coupling is achieved for the tunable DBR laser with an integrated isolator in section V.B.2. Since no input waveguide is required, this reduces the number of coupling interfaces from the input SMF to the free-space section without any waveguide interfaces. In addition, it also provides a simple way to characterize the propagation loss inside the free-space section and the overall loss for different lengths of free-space sections. This is done by measuring the insertion loss for a fixed length and subsequent reduction of the length of the free-space section by pushing the GRIN lens and SMF further into the free-space section as depicted in Figure V-3. These measurements are taken with glue that is not yet cured and therefore fluid. Different lengths of free-space sections ranging from 0 mm to almost 5 mm are characterized with this method. This chip is fabricated in a $\Delta n = 0.011$ material system with equipped $NA = 0.14$ GRIN lenses.

Measurements

The fiber-coupled free-space section is measured with a coupled SMF at the input and a lensed fiber at the output. Figure V-4 depicts the measurement results with a simulated curve derived by the theoretical model of the free-space section from II.B and III. Since the simulation model only considers the coupling from the polymer waveguide to the free-space section into the SMF and not the coupling loss from the polymer waveguide to the lensed fiber, all additional losses not related to the free-space section were subtracted from the measurements. This includes 1 dB coupling loss from the lensed fiber and waveguide propagation loss of 0.5 dB for a 7 mm long waveguide between the free-space section and the waveguide facet to the lensed fiber. This allows a direct comparison of the measurement and simulation results. An absorption loss of 5 dB/cm was assumed for the index-matching glue inside the free-space section for the simulation model.

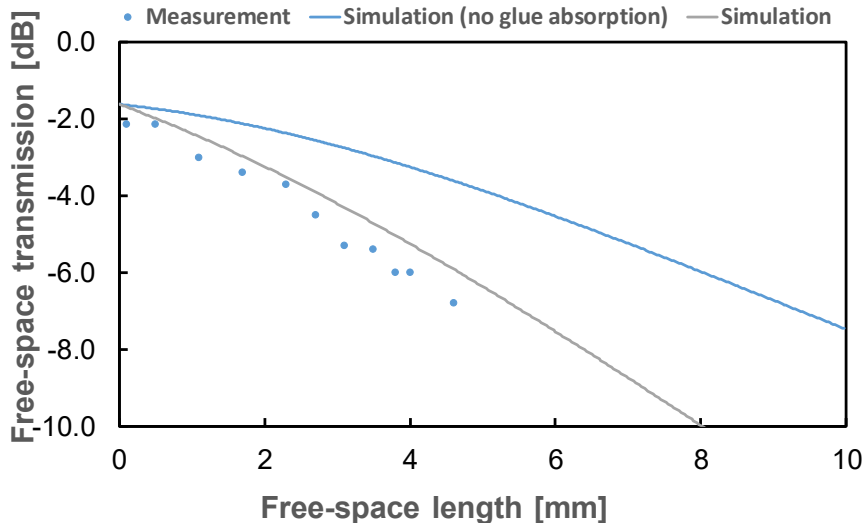


Figure V-4: Free-space transmission measurements depending on the free-space section length together with simulated values. The first simulation does not consider any additional absorption from the glue. In the second simulation, an absorption loss of 5 dB/cm was assumed for the glue.

For back-to-back aligned GRIN lenses with a space of only 0.2 mm between both lenses, transmission losses of 2.2 dB inside the free-space section were measured. This value gradually increases up to 6.8 dB for a free-space length of 4.6 mm.

Discussion

The overall slightly higher values for the measurements compared to the simulation can be explained with small misalignments of the GRIN lenses, but the simulation in Figure V-4 fits the measurement data very well. The higher values of the measurement and simulation curve in Figure V-4, compared to the simulations in III.B where values below 1 dB are measured, can be explained with the asymmetric coupling interface. In III.B, the mode field diameter for the input and output waveguide are identical. At the same time, the results from Figure V-4 are obtained for an input SMF with a mode field diameter of 10.4 μm and an output waveguide with a MFD of 6.8 μm . Thus, overall higher loss are expected. One significant loss contribution in this measurement is the high absorption of ~ 0.5 dB/mm from the index-matching glue. Especially for longer free-space lengths, one-third of the total loss can be attributed to the index-matching glue. Materials with lower absorption, e.g. ppLN crystals with an absorption of < 0.01 dB/cm, improve the overall loss of free-space sections, to be demonstrated for the ppLN integration in section V.D. An additional possibility to reduce the loss of the free-space section besides the integration of low-loss materials is the GRIN lens length optimization. The GRIN lenses for the measurements in Figure V-4 have a fixed length of 840 μm . However, the 2D coupling efficiency plots of Figure III-2 and Figure III-4 in chapter III show a slight curvature for optimized coupling efficiency, indicating that longer free-space sections also require slightly longer GRIN lenses. For example, optimal coupling for the 10 mm free-space length is achieved with 875 μm long GRIN lenses instead of the 840 μm lenses, the latter being the ideal GRIN lens length for 1 mm long free-space sections. Overall, the derived model of the free-space section matches very well with the measurement data. Therefore, the transfer matrix analysis for Gaussian beam transmission in II.B.3 offers an accurate model to describe the free-space sections.

3. Resonant cavity design

Overview

In the last set of test measurements before characterization of functional devices, the GRIN lenses are coated with a reflective coating to build a resonant cavity. The targeted reflectivity for these measurements is 80%, with the coated GRIN lens facets facing toward the waveguides and not the free-space section, as highlighted in Figure V-5. Facing the coating towards the waveguides helps to stabilize the resonator, as will be discussed later. The space between both GRIN lenses is 1.475 mm for the first and 2.920 mm for the second GRIN lens resonator. In both cases the free-space section is filled with air.

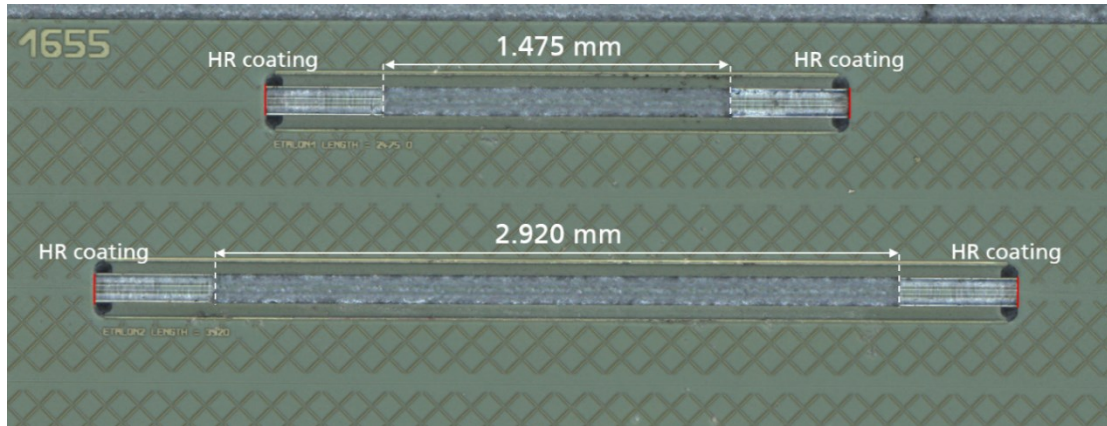


Figure V-5: Free-space sections with a free-space length of 1.475 mm (upper etalon) and a free-space length of 2.920 mm. In both cases the GRIN lenses have a length of 500 μm .

Measurements

The GRIN lens resonators are measured with an input and output lensed fiber. In order to determine the intrinsic resonator loss and the actual reflectivity of the GRIN lens coating, an Airy transmission function A_{trans} (see Appendix VI.2) is fitted to the data. Figure V-6a depicts the measurements for the GRIN lens resonator with a free-space length of 1.475 mm in between both GRIN lenses. A modulation depth of $12.1 \text{ dB} \pm 0.2 \text{ dB}$, a reflectivity of $R = 80 \% \pm 5 \%$ and intrinsic resonator loss of $L_{ORTL} = 2.6 \text{ dB} \pm 0.4 \text{ dB}$ were derived from the Airy fit model. The calculated free-spectral range is $FSR = 50.1 \text{ GHz} \pm 0.1 \text{ GHz}$. Similarly, the resonator with a free-space length of 2.920 mm is depicted in Figure V-6b. For this measurement, a modulation depth of $9.6 \text{ dB} \pm 0.2 \text{ dB}$, a reflectivity of $R = 80 \% \pm 5 \%$ and intrinsic resonator loss of $L_{ORTL} = 4.0 \text{ dB} \pm 0.4 \text{ dB}$ are obtained. The calculated free-spectral range is $FSR = 34.2 \text{ GHz} \pm 0.1 \text{ GHz}$. It is noted that due to the measurement with lensed fibers a weak second Fabry-Pérot resonator between the waveguide facets and the GRIN lens coatings with a free-spectral range corresponding to the waveguide length is created. This creates a wavelength beating visible in Figure V-6. To take this into account, a superposition of two Airy functions for each measurement, one for the actual resonator and one for the waveguide resonances is used to fit the data. The asymmetric shoulders in the spectrum in Figure V-6a were neglected for the Airy-fit in order to get a better fit of the peak itself. The shoulders origin most likely from a non-perfect polarization adjustment during the measurement.

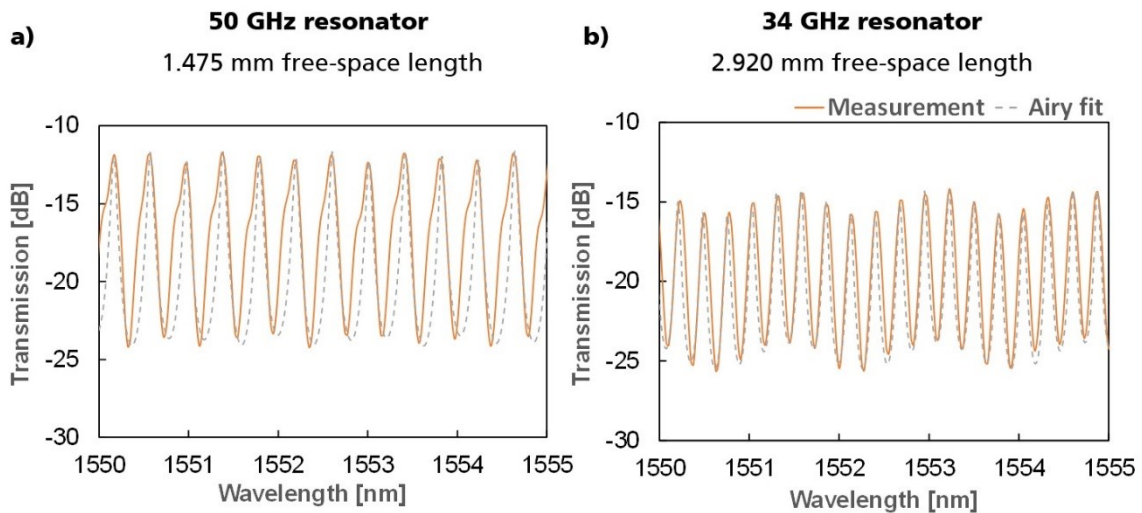


Figure V-6: Spectral measurement of a resonant cavity formed by two HR coated GRIN lenses, with a free-space length of 1.475 mm and 2.920 mm between both lenses.

Discussion

The GRIN lens resonator characterized in this work is build up with the reflective coating facing towards the waveguides (outer coating) and not the free-space section as indicated in Figure V-5. Even though a coating facing towards the free-space section (inner coating) might be the more obvious approach. However, an inward-facing coating will always result in an unstable resonator due to beam divergence of Gaussian beams. Stable resonator designs must fulfill the inequality

$$0 \leq \left(1 + \frac{L}{R_1}\right) \left(1 - \frac{L}{R_2}\right) \leq 1, \quad (\text{V-1})$$

described in chapter 4 of [87]. Here, L is the resonator length, thus the free-space section length plus the length of both GRIN lenses and R_i is the radius of curvature of the Gaussian beams at the left and right GRIN lens interfaces, facing towards the free-space section (see Equation (II-15)). In case of reflective coatings on the inner sides of the GRIN lenses, R_1 will always be positive and R_2 always negative due to the reflection on a plane surface and beam divergence of Gaussian beams.

Thus, $\left(1 + \frac{L}{R_1}\right) \left(1 - \frac{L}{R_2}\right)$ becomes larger than 1, indicating an unstable resonator. If the coating is on the outer side, the GRIN lenses can be designed to create a Gaussian beam with negative R_1 (positive R_2). In this case the inequality can be smaller than 1 (larger than 0) and the resonator is stable. It is noted that the sign of the first resonator term in Equation (V-1) is changed from negative to positive compared to 4.4-2 in [87], since it is adjusted to the radius of curvature of Gaussian beams in equation (II-15). Figure V-7 visualizes both resonator cases and explains the previous mathematical explanation visually.

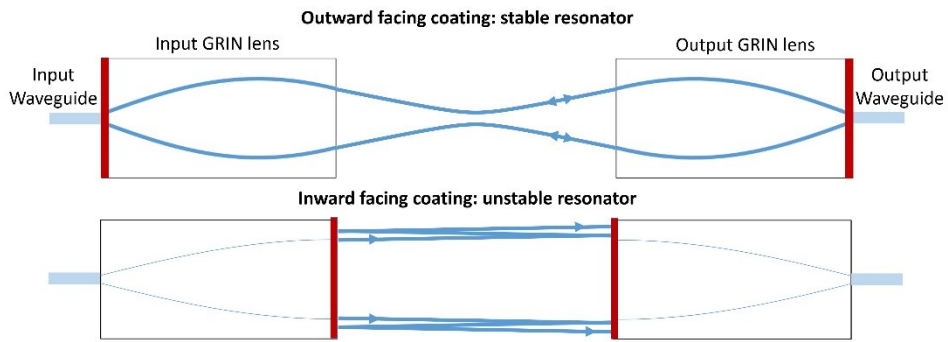


Figure V-7: Visualization of the resonator stability described in the text. The thick blue line describes the Gaussian beam radius of the resonator mode. For an outward facing coating, the GRIN lenses act as curved mirrors that refocus the optical beam with every roundtrip. The inward facing coating results in a continuously expanding beam, thus an unstable resonator.

For the shorter GRIN lens resonator, intrinsic resonator loss of $2.6 \text{ dB} \pm 0.4 \text{ dB}$ with a coating reflectivity of $80\% \pm 5\%$ are measured and calculated with the Airy fit, resulting in a modulation depth of $12.1 \text{ dB} \pm 0.2 \text{ dB}$. The calculated $FSR = 50.1 \text{ GHz} \pm 0.1$ is in good accordance with the targeted value of 50.0 GHz. The Finesse for the resonator, defined as the ratio between FSR and full width half maximum ($FWHM$) of the transmission peaks is 2.7 ± 0.3 . In comparison, the Finesse of an ideal resonator without any intrinsic loss and a reflectivity of 80 % would be 14.1, or roughly five times larger. This is partially due to the asymmetric peak side-modes visible in Figure V-6b, most likely originating from a non-perfect polarization adjustment, but mostly related to the intrinsic resonator loss.

The longer GRIN lens resonator yields loss of $4.0 \text{ dB} \pm 0.4 \text{ dB}$, a modulation depth of $9.6 \text{ dB} \pm 0.2 \text{ dB}$ and a free-spectral range of $34.2 \text{ GHz} \pm 0.1 \text{ GHz}$, again close to the targeted value of 34.0 GHz. The higher loss of the longer free-space section can be explained with a deviation from the ideal length of the GRIN lenses for a longer free-space section, similar to the free-space length variation measurements. GRIN lenses with a length of 500 μm were used for both resonators, but for the 2.92 mm long free-space section, the ideal length would be 515 μm , contributing around 1.0 dB to the resonator loss. Additionally, an increase in free-space length also leads to tighter alignment tolerances.

The current round trip loss of 2.6 dB are already a promising first result for a GRIN lens resonator integrated into a PIC, but a further loss reduction would be greatly beneficial for the resonator performance. The inwards facing facets of the GRIN lenses are not anti-reflection coated against air, meaning an additional AR coating would suppress unwanted internal reflections inside the resonator and reduce loss from internal reflections. This would reduce the loss per GRIN lens-to-air interface by 0.15 dB, or 0.6 dB per resonator roundtrip to roundtrip loss of 2.0 dB. Further improvements could be achieved by reducing angular errors during facet polishing in the GRIN lens fabrication. Suppose free-space sections are used for transmission only, e.g. for the integration of optical isolators. In that case, angular errors are negligible because the refractive index of the GRIN lenses and the surrounding index-matching glue match very well. However, if the lenses are used as reflective interfaces for a resonator, a small angular tilt can already greatly affect the stability of a resonator similar to a tilted mirror in a normal resonator. By reducing this angular facet error, together with an additional AR coating, roundtrip loss well below 1.0 dB can be expected. The transmission measurements in Figure V-2 indicate it should be possible to reduce the loss below 1.0 dB since free-space section loss of $0.84 \text{ dB} \pm 0.20 \text{ dB}$ (corresponding to half a roundtrip) were measured, including the intrinsic 0.5 dB loss of the index-matching glue.

Results

Even though the GRIN lens resonator measurements carried out in this section are only a small part of this work, they are among the most promising perspectives for future developments and improvements of the on-chip free-space section. The possibility of building on-chip resonators with GRIN lenses offers many additional applications for the on-chip free-space sections. Besides the already demonstrated wavelength locking in [44], one of the most obvious applications is a resonant cavity design for second-harmonic generation, further discussed in V.D.4. It could also be used to build passive Q-switched mode-locked lasers with the integration of active gain media and saturable absorber mirrors (SAMs) into the free-space section [88]. Furthermore, spectroscopy applications like cavity ring-down spectroscopy also make use of resonant cavities [89]. GRIN lenses have already been used to improve the stability of optical resonators in [90]. However to the best of our knowledge, the fabrication of a stable resonator using only coated GRIN lenses has not been demonstrated yet apart from this work.

B. Integrated optical isolator

1. Stand-alone isolator

Overview

Before integration with a tunable laser, the optical isolator, schematically shown in Figure II-10, is built up as a standalone device as depicted in Figure V-8. The standalone isolators consist of straight input and output waveguides inversely tapered towards the GRIN lenses to enlarge the mode field diameter and reduce the alignment tolerances as simulated in III. In order to test the influence of the angle of the free-space isolator onto the optical isolation, the isolator can be rotated inside the free-space section between 0° and 4°. Due to the high refractive index of the Faraday rotator, an angled isolator requires an offset between the input and output waveguide of the free-space section to compensate for the beam offset. For example, a 4° angled free-space isolator requires a 13 μm waveguide offset.

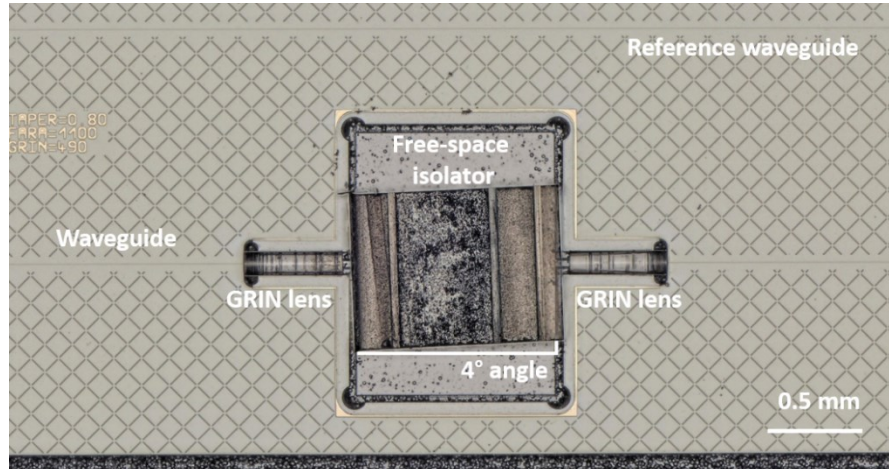


Figure V-8: Integration of a free-space isolator before applying index-matching glue. The isolator is inserted into a free-space section formed by two GRIN lenses coupled to the polymer waveguides.

Measurements

The stand-alone integrated isolator is characterized by measuring the optical transmission in forward direction for TE polarized light (the input polarization filter blocks TM polarized light) and backward direction for TE and TM polarized light. The measurement results are depicted in Figure V-9 together with the transmission of a straight adjacent reference waveguide. The device is

Results

measured with 6 μm spot size lensed fibers at the input and output that contribute 1.0 dB coupling loss per facet.

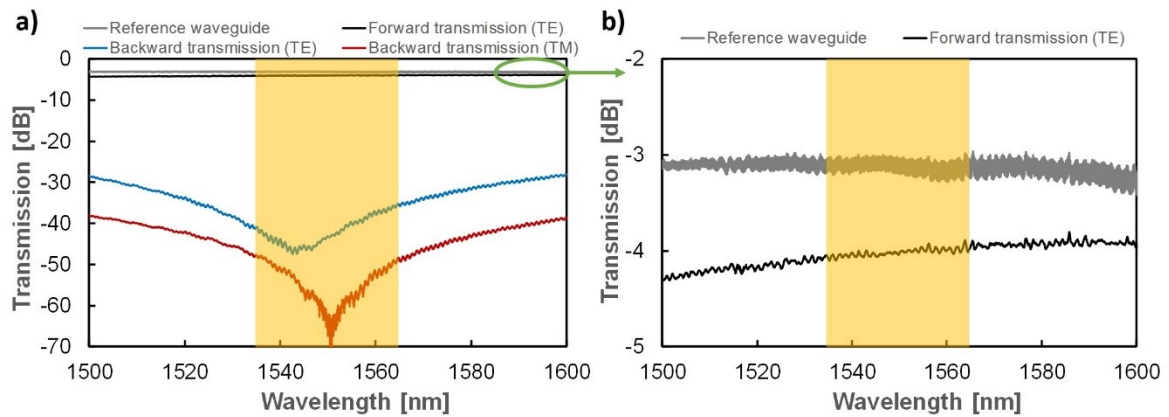


Figure V-9: a) Forward TE and backward TE/TM transmission of a 4° angled integrated optical isolator with a reference waveguide and highlighted C-band. b) Forward TE transmission with adjusted axis scale.

The excess loss with respect to the adjacent reference waveguide is 0.8 dB at 1550 nm and the device has a peak isolation of >44 dB at 1544 nm for TE polarization and >60 dB for TM polarization, both calculated with respect to forward TE transmission. The isolation bandwidth across the C-band spanning from 1530 nm to 1565 nm is 32 dB for TE polarization and 42 dB for TM polarization. A good indication that the isolation works as expected is also visible in the reduced spectral oscillations of Figure V-9(b) of the isolator measurement compared to the reference waveguide. Since the measurement was taken with lensed fibers, the waveguide-to-air interfaces create a weak Fabry-Pérot for the reference waveguide. For the waveguide including the isolator, the back reflections and, therefore the resonator modes, are mostly suppressed. The spectral optical isolation is depicted in Figure V-10.

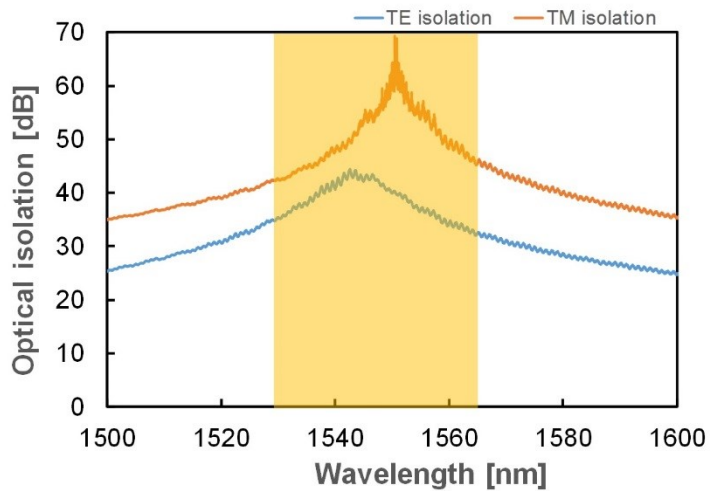


Figure V-10: Optical isolation for TE and TM polarization with highlighted C-band.

The higher isolation for TM isolation with respect to TE is due to the HWP at the isolator output. TE polarized light is rotated into the transmitting axis of the right polarization filter, while TM polarized light is rotated into the blocking axis of the polarization filter. Thus, it gets blocked at both polarization filters while TE polarized light is blocked only by the left polarization filter. Since the minimal optical isolation (in this case TE isolation) defines the overall optical isolation in a system with random polarization rotations, e.g. in a standard single-mode fiber, the lower TE values define and limit the overall optical isolation values for the isolator.

Results

The polarization filters inside the free-space isolator suppress the polarization partially by absorption and partially by reflection. Due to partial reflectivity, the polarization filters form a Fabry-Pérot resonator, and the light circulates between both polarization filters. To prevent a resonator effect that limits the achievable isolation, the results in Figure V-9 are obtained for a 4° angled isolator that destabilizes the cavity between the polarization filters and additionally reduces back reflections at the interfaces. The influence of the isolator angle is depicted for four angles between 0° and 4° in Figure V-11.

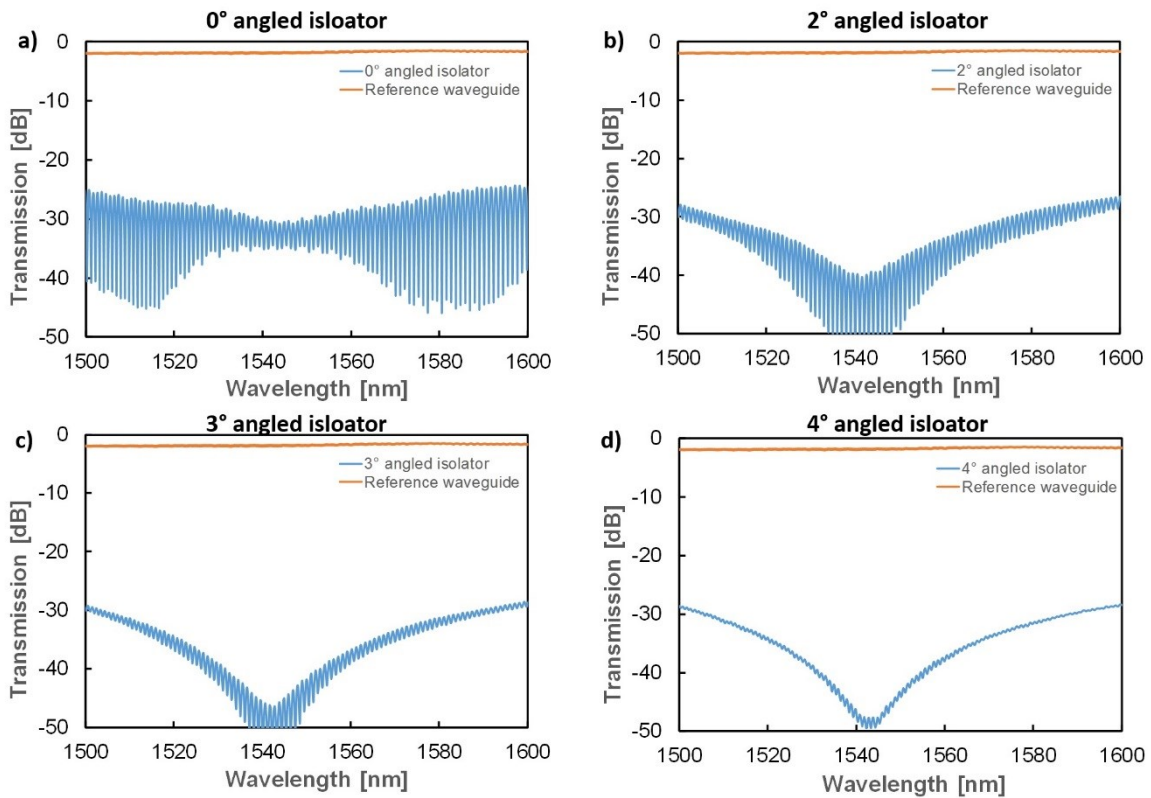


Figure V-11: Influence of the isolator angle on optical transmission in backward direction with a 0° angled isolator and 27 dB peak isolation (a), a 2° angled isolator and 36 dB isolation (b), a 3° angled isolator (42 dB isolation) and a 4° angled isolator. With increasing angle, the spectral oscillations vanish and the optical isolation increases.

The optical peak isolation improves from 27 dB, 36 dB, 42 dB up to 44 dB with an increasing angle. Angling the free-space isolator results in a beam offset that is caused by the high refractive index Faraday rotator. This must be compensated with an offset between input GRIN lens and output GRIN lens and thus, also the polymer waveguides to obtain optimal coupling efficiencies.

The measurement results in Figure V-9 depict the best device that was measured in terms of insertion loss and isolation ratio. However, typical isolators might yield slightly worse performance. Figure V-12 depicts the excess loss of a dozen different assembled isolator chips. The average loss of these devices is $1.5 \text{ dB} \pm 0.5 \text{ dB}$. Even though there are a few statistical outliers, most devices exhibit excess loss below 1.5 dB at 1550 nm. Discarding the three assembled devices with $>1.5 \text{ dB}$ excess loss, this value improves to $1.2 \text{ dB} \pm 0.2 \text{ dB}$, which can be considered the typical excess loss value of the integrated isolator.

Results

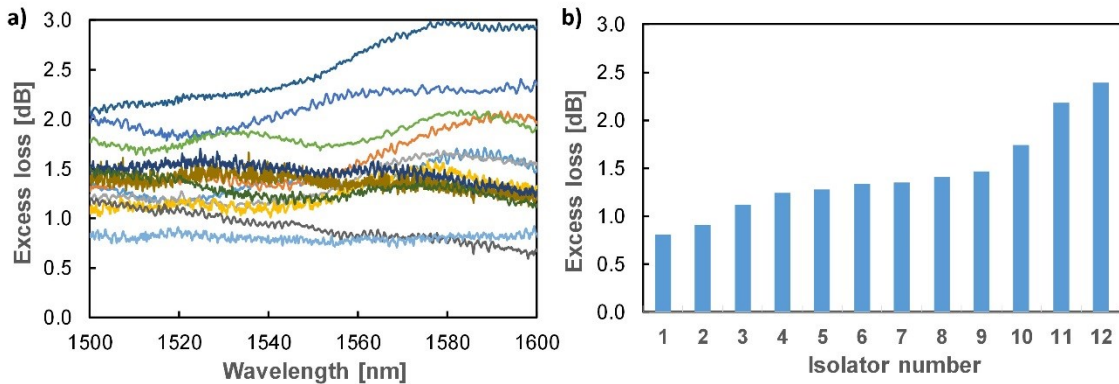


Figure V-12: Spectrum of the excess loss calculated with respect to their corresponding adjacent reference waveguides for a dozen integrated isolators and a histogram of the excess loss at 1550 nm.

Discussion

Typical peak isolations for the integrated isolators that can be achieved with the presented isolator design are >44 dB with an isolation bandwidth of >30 dB across the C-band. These values can be achieved very reliably due to the use of commercially available materials for the free-space isolator inserted into the on-chip free-space section, resulting in a yield close to 100 %. Thus, the optical isolation is also unaffected by deviations in the PolyBoard fabrication or the manual assembly process. In terms of excess loss, the best devices achieved values below 1 dB excess loss with respect to a reference waveguide. Considering average assemblies with excess loss below 1.5 dB, corresponding to a yield of ~75%, the typical excess loss is $1.2 \text{ dB} \pm 0.2 \text{ dB}$. Loss variations arise primarily from the manual assembly and deviations in the fabrication process, e.g. the depth of the etched U-grooves for the GRIN lens alignment or the GRIN lens length during GRIN lens fabrication. As mentioned in IV.C.1, the inserted free-space isolator inhibits intrinsic loss of <0.4 dB, leaving $0.6 \text{ dB} \pm 0.2 \text{ dB}$ to $0.8 \text{ dB} \pm 0.2 \text{ dB}$ caused by the on-chip free-space section, depending on the quality of the assembly. This includes coupling loss from the polymer waveguides to the GRIN lenses due to lens misalignment and additional losses from the interfaces filled with index-matching glue.

In section II.C.3, a figure of merit (*FOM*) defined as the ratio between the optical isolation and the insertion loss was introduced to compare different isolator designs in integrated optics. In this work, a *FOM* of 55 for the best performing isolator and typical values between 31 and 44 were achieved for the integrated isolators. As a comparison, the highest *FOMs* for an integrated isolator in literature are 14 and 24 reported by Pintus et al. and Cheng et al. [23, 61]. Figure V-13 depicts the two-dimensional plot of insertion loss and optical isolation from Figure II-9 with the addition of this work's isolator. In terms of insertion loss, only commercially available free-space isolators outperform the isolator demonstrated in this work, with values of 0.2 dB and 0.6 dB, while the optical isolation is equally good.

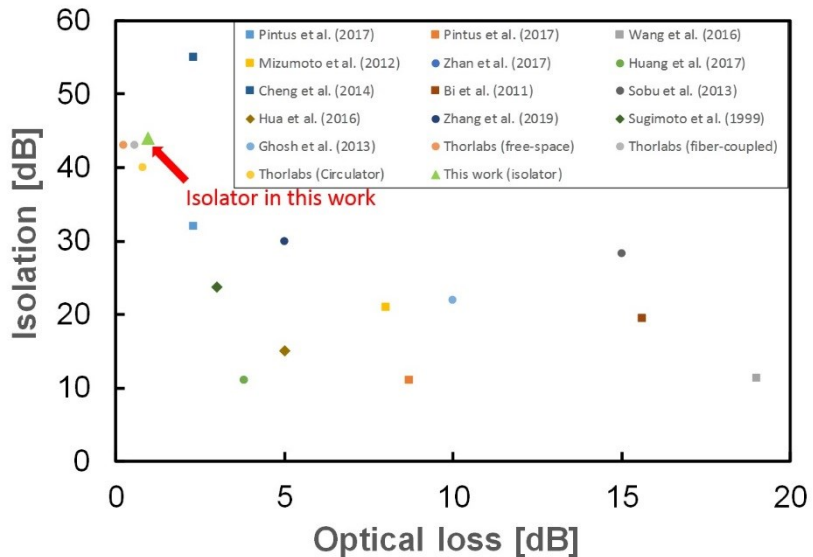


Figure V-13: Literature overview of isolator performance in terms of optical isolation and insertion loss with the isolator's added values from this work.

2. Isolator integration with a tunable DBR laser

Overview

The tunable laser co-integrated with the optical isolator consists of an InP gain section with a high reflection (HR) coated back facet and a thermo-optic Bragg-grating and phase shifter at the polymer side as described in IV.A.3. The free-space section output of this device is coupled directly to a SMF instead of a polymer waveguide. Figure V-14 depicts the assembled tunable laser with an integrated isolator that is mounted on a submount, according to the design proposed in Figure II-11 in II.C.4.

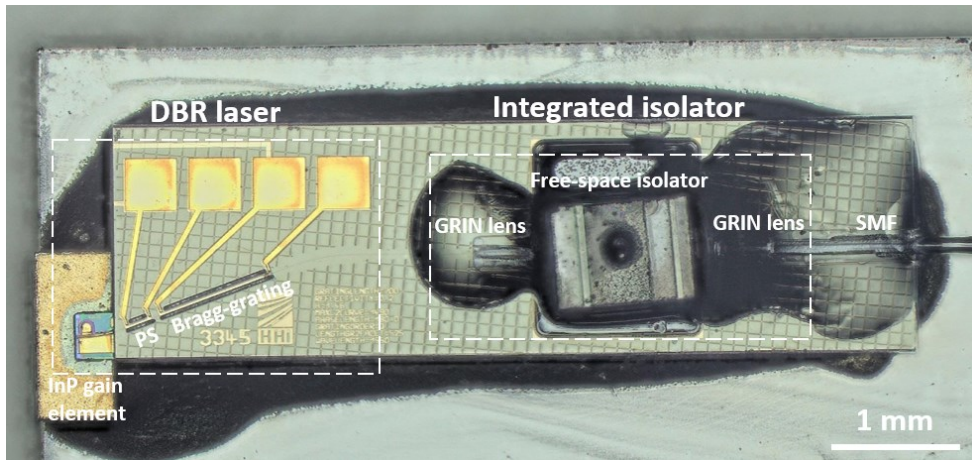


Figure V-14: Assembled tunable DBR laser with an integrated free-space isolator coupled directly to a single-mode fiber. The DBR laser consists of an indium phosphide gain element coupled to the polymer chip with a waveguide inscribed thermo-optic Bragg grating and a thermo-optic phase shifter (PS). The output GRIN lens on the right-hand side is coupled directly to a SMF.

Including the tapered waveguides inside the polymer, the optical isolator has a footprint of $3 \times 1 \text{ mm}^2$. The tunable laser with an integrated isolator has a total footprint of $7 \times 2 \text{ mm}^2$. This includes the $0.3 \times 0.3 \text{ mm}^2$ InP gain element on a submount. The chip is fabricated in the $\Delta n = 0.03$ refractive index material system.

Measurements

Similar to the characterization of the stand-alone isolator, the tunable laser with integrated isolator is first characterized as a bare polymer chip without coupled gain element, but with already coupled output fiber, enabling the direct characterization of the polymer chip with integrated isolator. The input waveguide of the polymer chip has a 17.8° angled waveguide to reduce back reflections at the polymer/InP interface. Accordingly, the device is measured with a $\sim 27^\circ$ angled lensed fiber on the input side due to the air/polymer interface. As a reference, a polymer chip with similar grating and phase shifter parameters but without isolator is measured with an angled lensed fiber on the left and a cleaved fiber at the output side. The measurement results in forward and backward direction are depicted in Figure V-15.

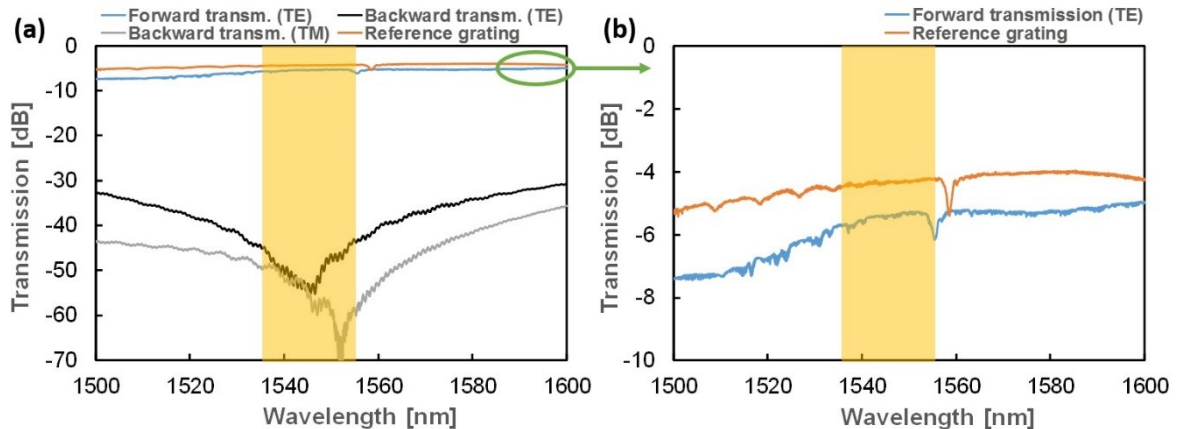


Figure V-15: (a) Forward and backward transmission of the tunable laser polymer chip with integrated isolator and coupled output fiber, measured before coupling the gain element. (b) Forward transmission with a reference grating and adjusted axis scale. The dips in both spectra are caused by the reflection of the polymer Bragg grating. The highlighted area corresponds to the tuning range of the DBR laser.

The measured excess loss (with respect to the reference grating) for the isolator is 1.0 dB at 1550 nm with a peak isolation of >47 dB and an isolation of >38 dB across the 17 nm tuning bandwidth of the laser. Besides low excess loss and high isolation, an integrated isolator should also yield low back reflections or high optical return loss to enable good isolation of the laser. The measured ORL is depicted in Figure V-16 together with the reference grating.

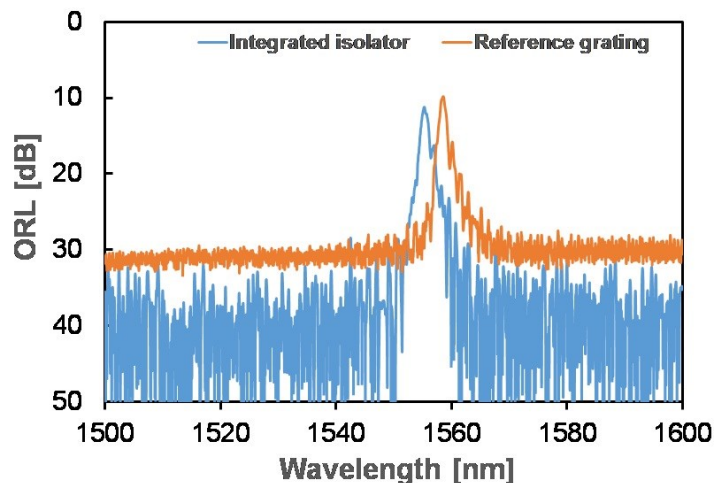


Figure V-16: Optical return loss measurement of the PolyBoard chip with integrated isolator and the reference grating chip.

Results

The devices are measured with an AR-coated input lensed fiber that contributes ORL of \sim 36 dB, that were subtracted from the measurement. Since the input fiber is angled, the back reflections of the input facet are negligible. At the output side of the reference grating, immersion oil with a refractive index of 1.51 between the waveguide and fiber facet correspond to an ORL signal of \sim 32 dB, calculated with Fresnel's equations (chapter 6 in [45]). Thus the immersion oil is the major contribution of back reflections in the reference grating. The ORL of the integrated isolator are lower, indicating that the angled free-space isolator does not contribute additional back reflections, while additionally blocking any reflections that might occur behind the isolator.

After this preliminary characterization, an InP gain element on submount is coupled to the polymer chip, and the output power and tuning range of the laser is measured. The results are depicted in Figure V-17. For a gain current of 100 mA, a fiber-coupled output power of 5.6 mW and continuous tuning over 17 nm is demonstrated.

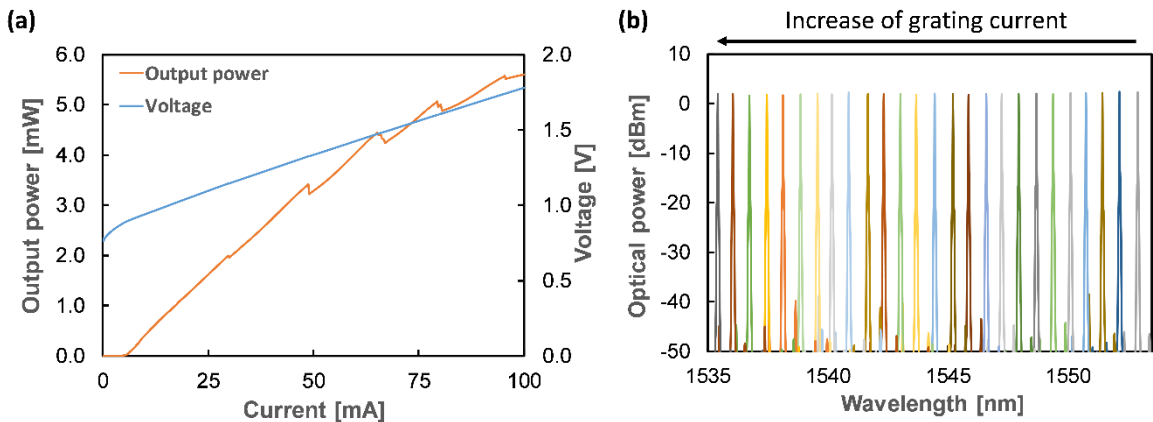


Figure V-17: (a) P-I curve of the laser measured at the fiber output. (b) Demonstrated tuning of the laser across a bandwidth of 17 nm. Different colors correspond to different tuning currents of the Bragg grating.

To verify the functionality of the isolator during laser operation, a transmission experiment with 10 Gbit/s non-return-to-zero (NRZ) direct modulation of the gain element is performed. The measurement setup is depicted in Figure V-18.

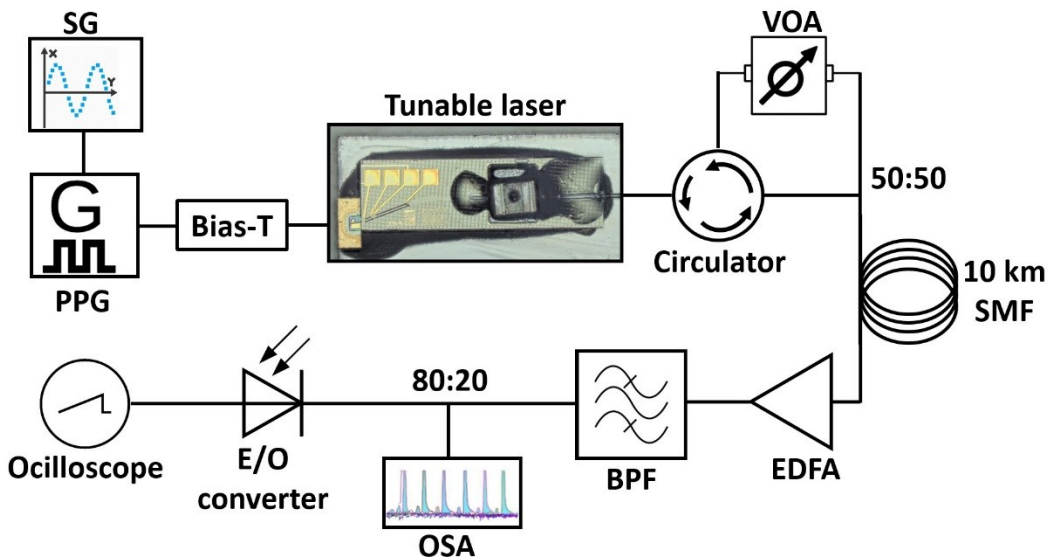


Figure V-18: Schematic layout of the 10 Gbit/s measurement setup with optical feedback. The 10 Gbit/s modulation created with a signal generator (SG) and a pulse pattern generator (PPG) is applied to the DC-biased gain element. A feedback loop with variable optical attenuator (VOA) returns up to -10 dB of optical feedback to the tunable laser with

Results

integrated isolator. After a 10 km fiber link, an erbium-doped fiber amplifier (EDFA) with bandpass filter (BPF), the signal is detected and visualized with an optical spectrum analyzer (OSA) and an oscilloscope.

The 10 Gbit/s NRZ bit pattern is generated by a 10 GHz signal from a signal generator and a pulse pattern generator. The modulated signal with a peak to peak voltage of 500 mV is applied to the DC biased gain element. The isolator is tested by introducing controlled optical feedback created via a fiber-based optical circulator and a 3 dB coupler. Half of the optical power is transmitted through the fiber link for the transmission experiment, while the other half is fed back into the tunable laser via a variable optical attenuator and the optical circulator. In total, the feedback loop consisting of a circulator, 3 dB coupler, VOA, and the coupled SMF of the PIC corresponds to a loop length of ~ 5 m and adjustable maximum feedback of up to -10 dB. This maximum value of -10 dB also takes the fiber-to-chip coupling loss of ~ 1.5 dB into account. After the fiber link with a length of 10 km, the signal is amplified with an erbium-doped fiber amplifier (EDFA). After an inline power monitor, the optical signal is converted into an electrical signal and visualized with an oscilloscope. An optical spectrum analyzer for monitoring the optical spectrum during laser modulation is placed after a 20:80 splitter between the EDFA and the inline power monitor. As a reference, the measurements were also carried out with a tunable laser without an optical isolator. Eye diagrams for no optical feedback, optical feedback of -20 dB, and maximum optical feedback of -10 dB are depicted in Figure V-19. In this instance, no optical feedback means that the fiber-based feedback loop's optical feedback is less than -50 dB.

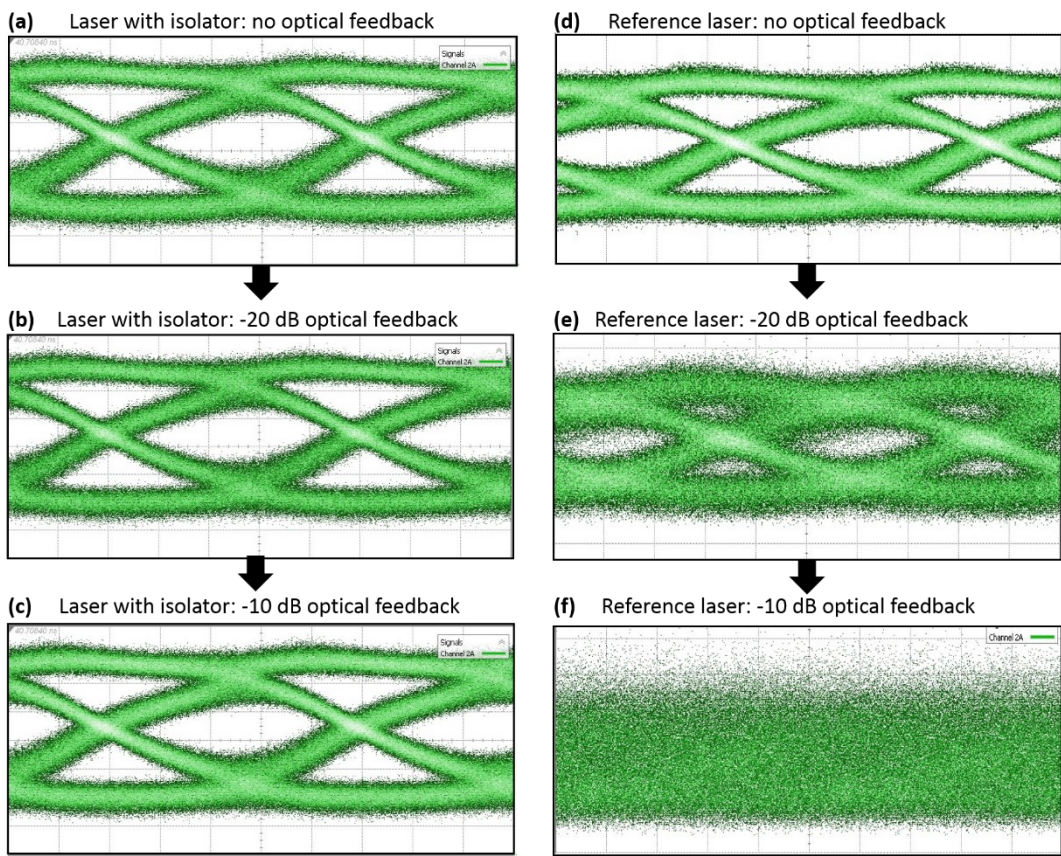


Figure V-19: 10 Gbit/s over 10 km eye diagram of the laser with integrated isolator with no optical feedback (a), -20 dB optical feedback (b), and -10 dB optical feedback. Similarly, a reference laser without an integrated isolator was measured with the respective optical feedback (d-f). It is noted that (a-c) and (d-f) are in scale within both subsets but not in scale to each other.

Unaffected by the amount of optical feedback, the eyes for the tunable laser with integrated isolator are clearly open with an extinction ratio of 2.9 dB and only a slightly decreasing signal-to-noise ratio (SNR) from 4.3 dB to 4.2 dB for Figure V-19 (a-c). With no optical feedback, the eye

Results

diagram of the reference laser without isolator is also clearly open with a SNR of 3.9 dB and an extinction ratio of 4.0 dB. However, for increasing optical feedback, the eye diagram starts to close, resulting in a drop of the SNR below 2 dB for -20 dB feedback and a completely closed eye diagram at -10 dB optical feedback.

Discussion

The measured peak isolation of the tunable DBR laser with >47 dB and excess loss of 1 dB are in good agreement with the values of the measured standalone isolators. Furthermore, the achieved output power of 5.6 mW is in the same range as tunable DBR lasers without the integrated isolator characterized prior to this work.

Even though defined optical feedback in lasers can benefit linewidth and chirp reduction or bandwidth enhancement [91, 92], uncontrolled feedback can lead to linewidth broadening and other unwanted effects. In [92], Tkach and Chraplyvy defined different regimes of optical feedback, today known as T-C diagrams, depending on the feedback power and distance. In the transmission experiment in section V.B.2 with the tunable DBR laser, the length of the optical feedback loop was 5 m with optical feedback of up to -10 dB. This corresponds to the fourth regime of the T-C diagram. In this regime, a significant linewidth broadening, known as coherence collapse and the creation of side modes might occur in the laser, that is observed in Figure V-19 during the transmission experiment with the reference laser. Thus, transmission is no longer possible, and no open eye is observable for the DBR laser without an integrated isolator in Figure V-19. Since the integrated isolator provides optical isolation of >38 dB across the tuning bandwidth of the laser, optical feedback from the loop is reduced to less than -48 dB, and stable operation for all levels of optical feedback is ensured. In the T-C diagram, optical feedback below ~-45 dB for a 5 m feedback length corresponds to the second regime. Even though mode splitting or hopping might occur in this regime due to out of phase feedback [93], this was not observed during the experiment for the DBR laser with integrated isolator. Thus, the transmission for the laser is stable at all levels of feedback with only a minor drop in the signal-to-noise ratio from 4.3 dB to 4.2 dB and clearly open eyes at all levels of optical feedback (Figure V-19a-c). In contrast, besides the aforementioned coherence collapse of the reference laser for -10 dB feedback that completely prevents any form of transmission, already at moderate optical feedback of -20 dB, a significant drop in the transmission quality is observed together with a SNR drop to around one dB in the reference laser (Figure V-19e).

Besides good values in terms of optical loss and isolation, the stable transmission for all levels of optical feedback shows that the co-integration of the isolator with other optical components on the PolyBoard platform is also possible. Even though the integration of laser and isolators has been demonstrated before for a distributed feedback laser in indium phosphide [29] (but with very poor performance), to the best of our knowledge this is the first co-integration of a DBR laser with an optical isolator in a PIC.

3. Integrated optical isolators at other wavelengths

The optical isolators demonstrated in this work are designed to work at a center wavelength of 1550 nm. However, the basic concept of the free-space isolator integration is also applicable to other wavelengths provided that Faraday rotators at the targeted wavelength are available since the polymers are also transparent at visible wavelengths. In this work, rare-earth-doped iron garnets provide the 45° Faraday rotation required for optical free-space isolators, that have a transparency range with low absorption from the C-band down to the O-band. Thus, the proposed isolator design could be directly used for all telecom and datacom wavelengths with an adjusted Faraday rotator length (smaller wavelengths require shorter Faraday rotators) and appropriate

Results

polarization filters. Within two wavelength regions commonly used in laser physics at 1064 nm and 785 nm, RIGs are also transparent, offering two additional windows for applications, even though the material absorption is higher than at 1550 nm (see Appendix VI.4). However, isolators in the visible light regime require a new material. The most commonly used material is terbium gallium garnet (TGG) that provides a large transparency range from 400 nm to 1500 nm, except for a small window of high absorption in the green spectrum [94]. The main disadvantage compared to RIGs are the paramagnetic characteristics of TGGs compared to the ferrimagnetic RIGs. As described in II.C.2, the ferrimagnetic RIGs act as weak intrinsic permanent magnets that require no external magnetic field, and the magnetic permeability strongly enhances the magnetization resulting in a small footprint for a 45° Faraday rotation. In contrast, even though TGG has a relatively high Verdet constant (see Equation (II-54)), it requires a strong external magnetic field to operate in an optical isolator. For example, with a typical Verdet constant of 130.6 Rad/(T m) at 633 nm [95], an applied magnetic flux density of 1 T, a length of 5.9 mm would be required for a 45° Faraday rotation, compared to the 0.5 mm of the Faraday rotators based on RIGs used within this work. Even though the integration of isolators based on TGG might be challenging, other emerging materials like cadmium manganese telluride which offer an up to six times higher Verdet constant, might be a suitable material for isolators in the visible regime [96].

C. Integrated optical circulator

1. Polarization-based circulator

Overview

The first integrated circulator comprises a three-port design based on a nonreciprocal polarization rotation as described and schematically depicted in II.C.4. After the input waveguide, a PBS thin-film filter separates TE and TM polarized light into different waveguides that each include a free-space section. Inside the free-space sections, a -45° Faraday rotator and a 22.5° HWP induce a nonreciprocal polarization rotation in forward and a polarization conservation in backward direction. A second PBS thin-film filter combines the TE and TM path and guides it to the second port. Figure V-20 depicts the assembled device characterized within this work. Similar to the tunable laser with integrated isolator, the circulator is fabricated in the $\Delta n = 0.030$ material system with $3.2 \times 3.2 \mu\text{m}^2$ waveguides.

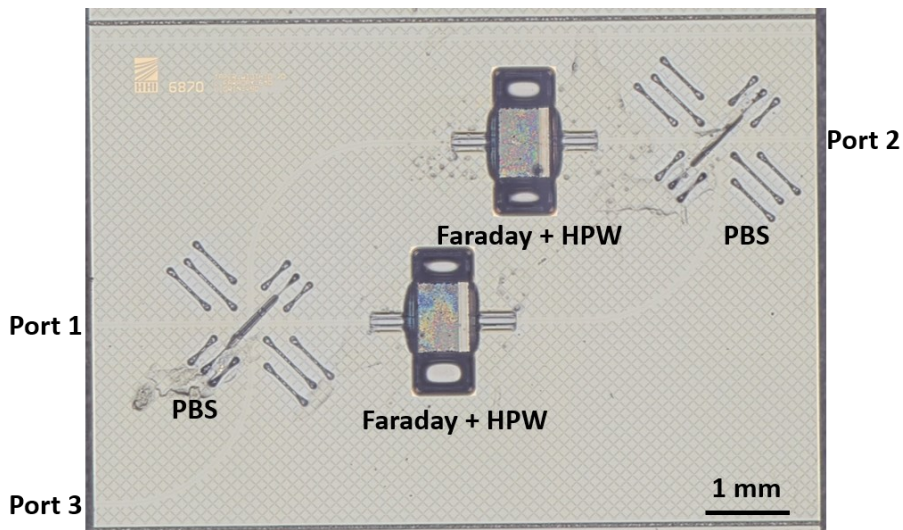


Figure V-20: Assembled integrated circulator comprising an input and output polarization beam splitter (PBS) and two free-space sections with an integrated Faraday rotator and half-wave plate (HWP).

Circulator measurements

All port combinations of the PBS circulator are measured with an input and output lensed fiber in forward and backward direction. For a -45° magnetized Faraday rotator, the measurement results are depicted in Figure V-21(a). After the initial characterization, the measurements were repeated but with a reversed Faraday rotation of $+45^\circ$. Reversal of the intrinsic magnetization is achieved with a strong permanent magnet that is brought temporarily in close proximity of the chip, as described in section II.C.4. The results of the repoled PIC with $+45^\circ$ Faraday rotators are depicted in Figure V-21(b).

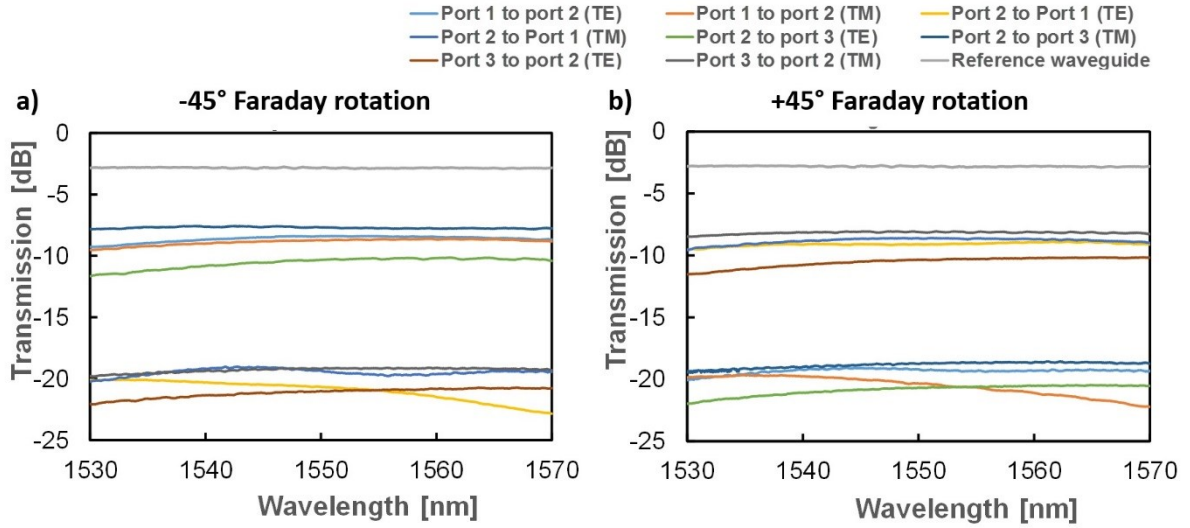


Figure V-21: Transmission measurements in forward and backward direction for TE and TM polarization of the integrated circulator with -45° Faraday rotators (a) and $+45^\circ$ Faraday rotators (b).

Reversal of the Faraday rotation also reverses the port order of transmission. Whereas for the initial -45° rotation, the port transmission was from port 1 to port 2 to port 3, the order reversed to transmission from port 3 to port 2 to port 1 for $+45^\circ$ Faraday rotation. The excess loss (EL) at 1550 nm with respect to a reference waveguide for both magnetization states are depicted together with the achieved optical isolation in Table V-1. It is noted that the optical isolation is calculated as a polarization-independent isolation. Thus it is calculated with respect to TE or TM polarization, whichever is lower, as it was also done for the optical isolator in V.B.

Table V-1: Excess loss at 1550 nm for a -45° and $+45^\circ$ Faraday rotation for all port configurations and the corresponding isolation of the different ports. Pairs of highlighted shades of yellow correspond to optical transmission in the same optical path, while shades of grey correspond to optical isolation in the same optical paths for the differently polarized Faraday rotators.

	-45° Faraday rotation			$+45^\circ$ Faraday rotation		
	EL (TE)	EL (TM)	Isolation	EL (TE)	EL (TM)	Isolation
Port 1 to port 2	5.6 dB	5.9 dB	10.6 dB	16.4 dB	17.5 dB	-
Port 2 to port 3	7.5 dB	4.8 dB	9.0 dB	17.9 dB	16.0 dB	-
Port 3 to port 2	18.1	16.3	-	7.5 dB	5.3 dB	9.5 dB
Port 2 to port 1	17.8	16.5	-	6.3 dB	5.8 dB	10.1 dB

Results

Overall, the measured excess loss are within 4.8 dB and 7.5 dB, with an optical isolation of >9 dB at 1550 nm. Each measurement in Table VI-1 follows a different path that involves different optical elements depending on the polarization and entrance port. For example, transmission from port 1 to port 2 for TE polarized light involves transmission of the first PBS filter and the lower free-space section and reflection at the second PBS filter. TM polarization from port 1 to port 2 involves reflection at the first PBS, transmission of the upper free-space section, and the second PBS. Thus, the different paths allow a good estimation of the losses contributed by the different elements. The free-space sections with integrated Faraday rotator and HWP are estimated to contribute loss of 1.5 dB, and the PBSs add 3 dB of loss in transmission and 1 dB loss in reflection.

Integrated circulator as a latching switch

Repoling of the Faraday rotator inveres the transmission direction of the circulator as depicted in Figure II-13. Besides the operation as a passive circulator, the device can function as an optical 1x2 switch that can switch between port 1 and 3 with port 2 as the input. Since the Faraday rotators conserve their magnetization state and only require a temporary external magnetic field (thus energy) during the repoling process, the circulator acts not only as a switch but a latching switch that requires energy only during the switching process and maintains its state otherwise. The two switching states are depicted in Figure V-22. For this measurement, repoling of the Faraday rotators was done manually with a strong permanent magnet brought in close proximity of the optical circulator.

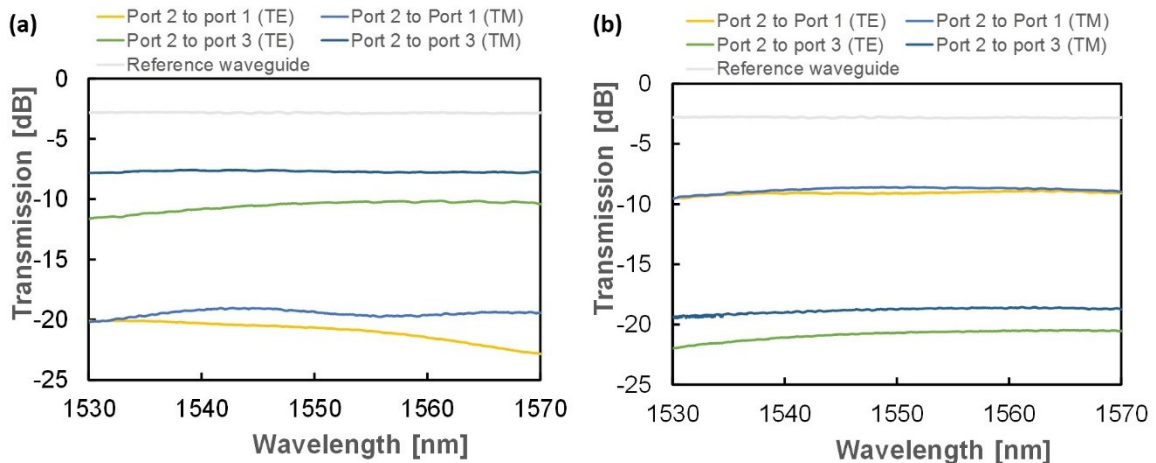


Figure V-22: Demonstrated switching between ports 1 and 3 with port 2 as the input port for a -45° Faraday rotation (a) and +45° Faraday rotation (b).

Discussion

For the PBS circulator, an excess loss of 4.8 dB to 7.5 dB and optical isolation of 9.0 dB to 10.6 dB are measured depending on the different port configurations. The loss breakdown yields a loss contribution of 1.5 dB from each free-space section and 3 dB transmission, and 1 dB reflection loss for the PBS. These PBS values are in good agreement with measured test structures and a loss of 1.5 dB for the free-space section is a good estimation, considering the average measured loss of the different free-space isolators measured in Figure V-12 between 1.0 dB and 1.5 dB. Thus, with 3 dB transmission loss, the PBS filter design used in this work is the limiting factor in terms of optical loss of the circulator. The high PBS loss stems from the width of the filter slot that is etched inside the waveguide. The filter itself is designed to have a width of 14 μm to fit the TFF. Due to the 45° orientation of the filter slot and an estimated undercut of 2 μm in both directions created during the etching process, the unguided transmission path of the optical mode is larger than 24 μm which

Results

results in significant propagation loss. A solution would be the integration of the PBS filter within the on-chip free-space section, as it will be discussed later in this section.

The most likely reason for the limited optical isolation of the circulator are also the PBS filters in combination with the waveguide bends and not the free-space section with integrated Faraday rotator and HWP. The latter showed a high polarization extinction ratio (PER) of >30 dB when tested separately in a free-space setup, whereas the PER of separately measured PBS test structures showed average values of 15 – 18 dB if the polarization is adjusted with respect to the lab system (see Appendix VI.5).

In II.C.1, the formal definition of an optical circulator is given by an asymmetric scattering matrix. For TE operation and a -45° Faraday rotation, the scattering matrix of the circulator can be calculated from the second row in Table II-1. Similarly, the scattering matrix for TE polarization and a +45° Faraday rotation is given by the fifth row in Table II-1. Both scattering matrices are depicted in the table below, where any optical return loss are neglected and set to zero.

Table V-2: Scattering matrix of the PBS circulator based on the measurement results of Table II-1 for a positive and a negative Faraday rotation.

$S_{TE,-45^{\circ}FR}$	$S_{TE,+45^{\circ}FR}$
$\begin{pmatrix} 0 & 0.02 & 0 \\ 0.28 & 0 & 0.02 \\ 0 & 0.18 & 0 \end{pmatrix}$	$\begin{pmatrix} 0 & 0.23 & 0 \\ 0.02 & 0 & 0.18 \\ 0 & 0.02 & 0 \end{pmatrix}$

Neglecting any imbalances that arise from the different optical paths that the light takes, the reversal of the Faraday rotation sign transposes the scattering matrix of the circulator:

$$S_{TE,-45^{\circ}FR} = (S_{TE,+45^{\circ}FR})^T. \quad (\text{V-2})$$

The second row from both matrices describes the light propagation from port 2 to the other ports. Due to the transposed scattering matrix, the circulator acts as an optical switch with integrated isolator.

In this work, the magnetic field was applied manually with a permanent magnet, but switching could also be achieved by a small electromagnet bonded on top of the Faraday rotators. This would enable the development of a latching-type optical switch that maintains its state without power consumption. Even though integrated latching switches, e.g. based on micro-electromechanical systems (MEMS) [97] or plasmonic memory effects have already been reported, integrated latching switches based on magneto-optic materials have not been demonstrated yet.

2. Phase shift based optical circulator

Overview

The second circulator is based on a Mach-Zehnder interferometer that induces a nonreciprocal phase shift, as described in II.C.4. The assembled device before GRIN lens alignment and glue application is depicted in Figure V-23. It comprises a MZI interferometric structure formed by two MMI couplers with a phase shifter and variable optical attenuator in each arm. Two free-space sections with a 45° Faraday rotator and a 22.5° HWP in each arm induce the nonreciprocal phase shift. The MZI circulator is also fabricated in the $\Delta n = 0.030$ material system with $3.2 \times 3.2 \mu\text{m}^2$ waveguides.

Results

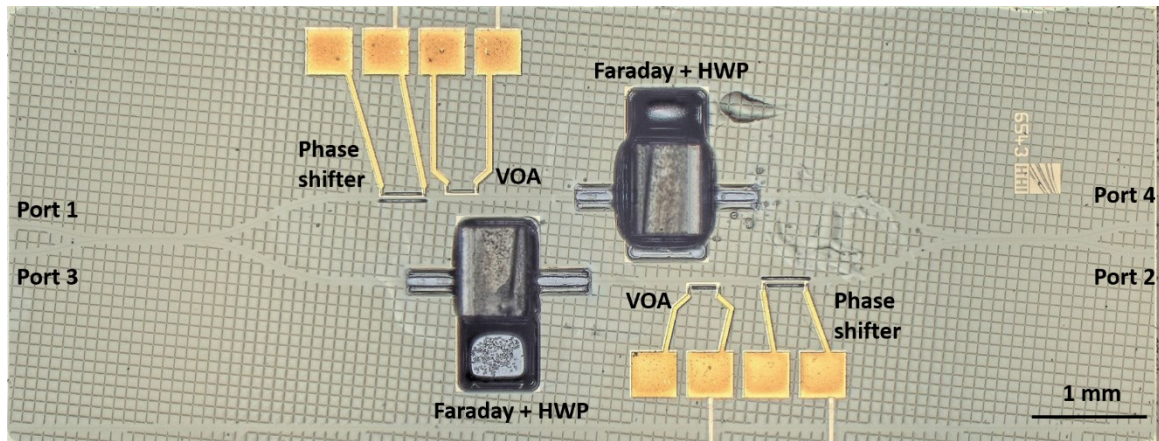


Figure V-23: Fabricated optical circulator based on a Mach-Zehnder-interferometric design that comprises a Faraday rotator plus HWP together with a phase shifter and VOA in each arm

Measurements

Like the PBS-based circulator, the interferometric circulator is measured in forward and backward direction for all port configurations. For TE polarization and a phase shifter current of 10.2 mA in the upper arm, the results are depicted in Figure V-24. In forward transmission excess loss between 3.9 dB – 4.1 dB were measured, resulting in an imbalance below 0.2 dB. Depending on the port configuration, an optical isolation between 15.1 dB and 19.1 dB was measured.

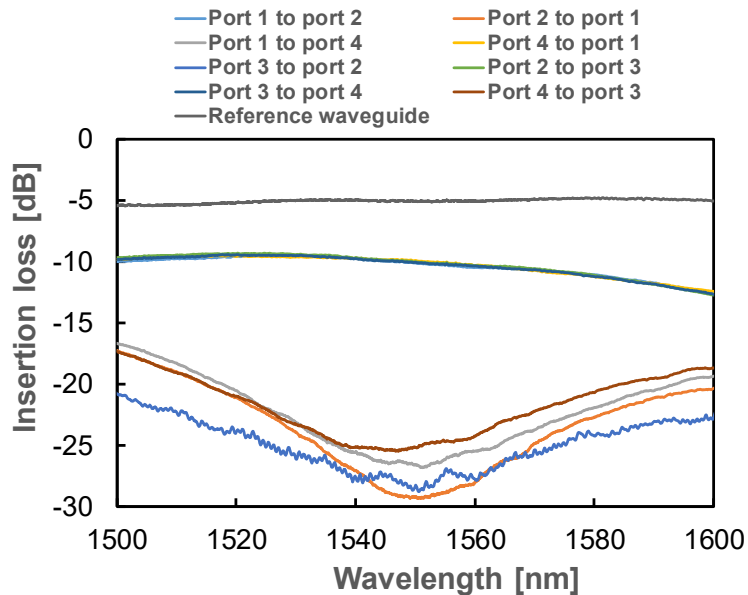


Figure V-24: Forward and backward transmission of all possible port combinations for TE polarized light and a phase shifter current of 10.2 mA.

The measurement results for TM polarization are depicted in Figure V-25. In forward transmission excess loss between 3.7 dB and 4.3 dB with respect to an adjacent reference waveguide were measured for TM polarized light and the optical isolation ranges between 10.9 dB and 18.7 dB. The TM polarization measurements were taken at a phase-shifting current of 14.8 mA at the upper phase shifter.

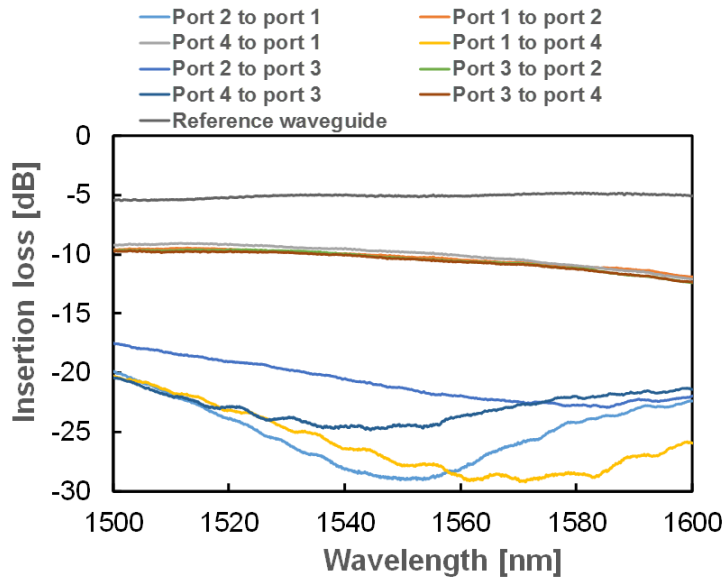


Figure V-25: Forward and backward transmission of all possible port combinations for TM polarized light and a phase shifter current of 14.8 mA.

Similar to the PBS filter based circulator, the excess loss can be attributed to the different optical components. The 2x2 MMIs add 0.5 dB of excess loss each and the typical VOA loss is 1.0 dB, while excess loss of the phase shifter can be neglected. This would leave around 2 dB of loss for the on-chip free-space section with integrated Faraday Rotator and HWP.

Since a thermo-optic phase shifter is integrated into both arms of the circulator, it is possible to tune the operation range of the circulator within a window of more than 40 nm by adjusting the phase current. Figure V-26 depicts this tuning behavior for different phase shifter currents at the phase shifter in the upper arm of the chip.

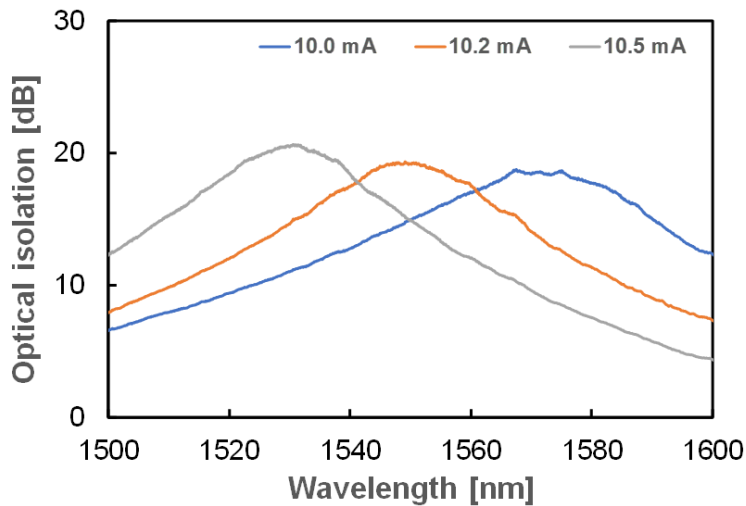


Figure V-26: Tuning of the optical isolation by the adjustment of the phase shifter current. For increasing phase shifter currents, the peak isolation is shifted to lower wavelengths.

Discussion

For the MZI circulator, excess losses between 3.7 – 4.3 dB and a peak isolation between 10.9 dB and 19.1 dB is measured. The losses can be accounted to the excess loss of the MMIs, the VOAs, and the free-space sections. The optical attenuators were integrated to reduce the potential optical

imbalance in both arms due to the manual assembly and alignment of the two free-space sections. However, VOA operation neither improved the extinction nor the structure's excess loss, indicating an already low imbalance in both arms. Since they add an additional loss of 1.0 dB, the overall loss of the circulator could be reduced below 3 dB by removing the VOAs from the circulator design. The achieved optical isolation is most likely limited by the imbalance of the output MMI, resulting in a slight coupling mismatch between the two ports on one side. It is noted that the overall loss of all structures, including the reference waveguides, showed a much higher loss than normally expected. All devices of this wafer showed significantly higher waveguide propagation loss of around 3 – 4 dB/cm in contrast to the normally expected 0.7 dB/cm, indicating a wafer fabrication error during the waveguide structuring. But since the optical loss of the circulator are calculated with respect to a reference waveguide, the additional waveguide propagation loss can be factored out of the shown excess loss measurements.

Even though designed for a center wavelength of 1550 nm, adjustment of the optical phase with the phase shifter also allows the circulator to operate at other wavelengths besides 1550 nm. In Figure V-26, the optical peak isolation is shifted between 1530 nm and 1570 nm for applied phase shifter currents by variation of the phase shifter current, similar to the circulator design proposed by Huang et al. in [26].

During the measurement, a strong polarization dependence between TE and TM polarization was observed. That is why TE operation is demonstrated at a phase-shifting current of 10.2 mA dB and TM operation at a phase shifter current of 14.8 mA. This polarization dependence is observed not only in the circulator structure itself but also in additional Mach-Zehnder interferometric test structures (see Appendix VI.6). In fact, the phase shift between both polarizations is close to π , meaning that while the circulator and the test structures transmit TE polarized light, they block TM polarized light. The reason for this behavior is most likely the small birefringence of the polymer waveguides, which induces a phase shift of $\sim \pi$ between both polarizations. Simulations show that due to the material birefringence, optical modes with TE polarization have an effective refractive index of 1.4620 in $\Delta n = 0.030 / 3.2 \times 3.2 \mu\text{m}^2$ waveguides, while the simulated effective refractive index of the TM mode is 1.4633. This means that for a propagation distance of $\sim 600 \mu\text{m}$, a phase shift of π between TE and TM polarization is induced. In other words, increasing or decreasing the length of the waveguides in both arms by $600 \mu\text{m}$ of the MZI should remove the polarization dependence.

3. Comparison between both circulator designs

In direct comparison, the MZI circulator has lower loss of 0.5 – 3.2 dB than the PBS circulator, depending on the port configuration and an optical isolation that is a few dBs higher. By simply removing the VOA from the MZI design, the overall loss could be reduced by an additional decibel. Reducing the total excess loss below 3 dB is of particular interest because it offers the possibility of exchanging 3 dB couplers in photonic circuit designs requiring bidirectional operation with the optical circulator. One drawback in the current design is the polarization dependence that could be fixed with the previously mentioned propagation length adjustment. However, the most significant drawback is that the MZI circulator requires an active phase stabilization to work. In contrast, the PBS circulator operates completely passive, making it the favorable circulator design to improve. Figure V-27 depicts the 2D chart of insertion loss and optical isolation from Figure II-9 with the added values of both circulator designs.

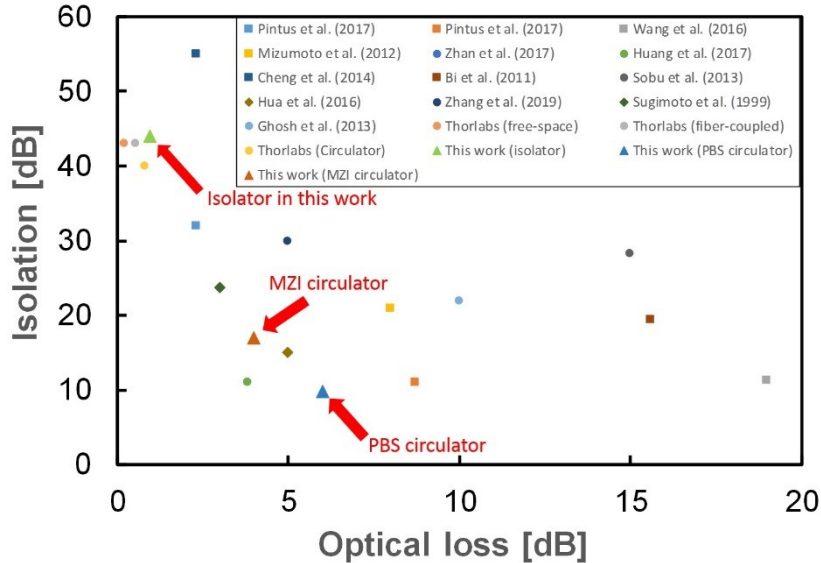


Figure V-27: Comparison of optical loss and isolation of the PBS and MZI circulator with values from other devices reported in the literature.

While the integration of an optical isolator that was demonstrated in V.B works exceptionally well, outperforming any other reported devices in integrated optics, the more complex circulators still require a redesign to improve both insertion loss and optical isolation. However, the PBS circulator design works polarization independent, while all the other designs in Figure V-27, except for the work from Sugimoto et al. [59], work only polarization dependent. In the current PBS design, the performance limiting factor are the waveguide integrated PBS filters that add up to 3 dB of loss in transmission due to the beam divergence in the etched slots. One idea to reduce these loss would be a new design that shifts the PBS filters into the on-chip free-space section, as depicted in Figure V-28. The PBS filters are placed behind the GRIN lenses inside the free-space section in the proposed design, removing any excess loss of the TFF slots inside the waveguides. In order to guide the light, two additional mirrors would be required in the design. But at the same time, it requires only three instead of four GRIN lenses and only one Faraday rotator plus HWP, making the design much smaller than the design tested within this work. One could also think about integrating a separately assembled commercially available free-space circulator, but these require birefringent walk-off crystals that are relatively large, making the proposed design much smaller and beneficial for the total loss inside the on-chip free-space section.

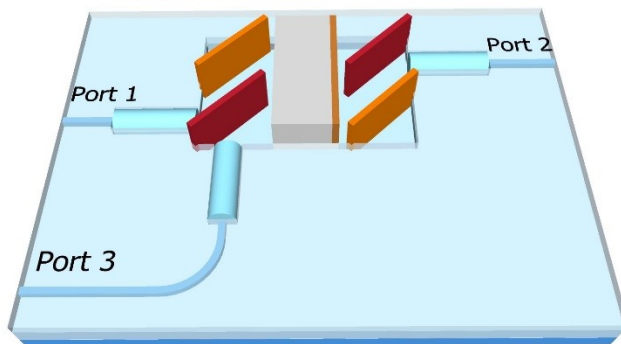


Figure V-28: Proposed design for an integrated circulator where the PBS filters (red) are not waveguide integrated but placed inside the free-space section. In addition to the PBS filters, two 90° mirrors (orange) are required inside the free-space section.

A unique feature of the circulators is the latching ability due to the magnetization preserving Faraday rotators, not possible in other integrated circulator designs depicted in Figure V-27. With the demonstrated isolator already working exceptionally well, further improvement of the circulator should be the priority in nonreciprocal applications. Especially applications beyond Telecom/Datacom in sensing like Fiber-Bragg-sensing or lidar greatly benefit from the implementation of integrated circulators.

D. Integrated second-harmonic generation

1. Overview

In contrast to the previously characterized PICs, the waveguides for the SHG have a cross-section of $7.3 \times 7.3 \mu\text{m}^2$ with a refractive index difference of $\Delta n = 0.005$, that benefit from lower fiber-to-chip coupling loss. As discussed in III.B, these waveguides correspond to GRIN lenses with a numerical aperture of 0.14. Two sets of GRIN lenses are fabricated to create a collimated and a focused free-space section to compare both results in terms of conversion efficiency with each other. The focusing lenses with a calculated ideal length of 1330 μm correspond to a beam waist of 6 μm inside the center of the crystal, as indicated by the simulation in Figure III-6. Corresponding calculated values for the collimating lenses are 840 μm and a waist of 38 μm . The GRIN lenses fabricated for the collimating beam have a length of 840 μm in good accordance with the targeted 840 μm from the simulation. In comparison, the fabricated length of the focusing lenses of 1300 μm deviates slightly from the targeted length of 1330 μm . Both devices are assembled with a 1 mm long AR coated ppLN crystal as depicted in Figure V-29. After assembly of the free-space section, both devices are butt coupled to an input and output 1550 nm SMF.

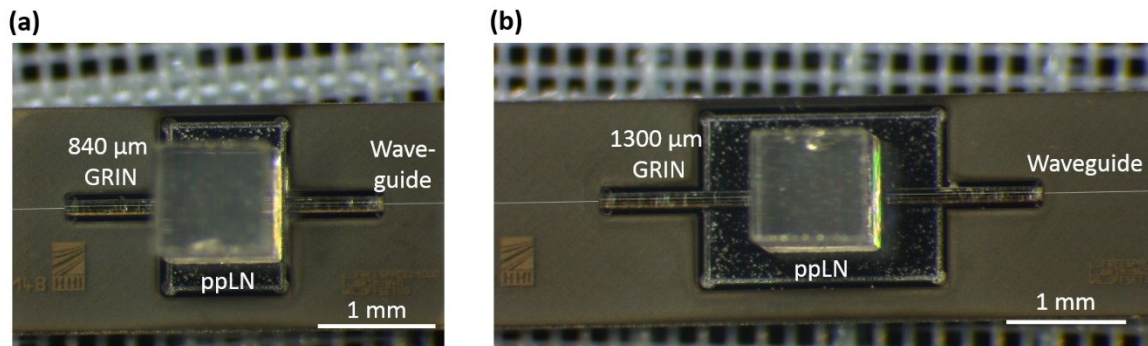


Figure V-29: Fabricated devices with collimating (a) and focusing (b) GRIN lenses with highlighted waveguides before fixation with index-matching glue.

2. Characterization with a continuous wave laser

Before characterization of SHG, the insertion loss of both chips at 1550 nm is measured. Figure V-30 depicts the insertion loss measured with input and output lensed fiber, together with an adjacent reference waveguide of the collimated chip. The coupling loss with 6 μm spot-size lensed fibers is estimated to be $1.5 \text{ dB} \pm 0.2 \text{ dB}$ per facet. Excess losses below $0.7 \text{ dB} \pm 0.1 \text{ dB}$ and $1.8 \pm 0.1 \text{ dB}$ at 1550 nm are measured for the device with collimating lenses and focusing lenses respectively. After this pre-characterization, SMF-28 fibers are aligned and fixed at the input and output of both chips. Due to the better matching optical modes, the coupling loss is reduced to $0.5 \text{ dB} \pm 0.1 \text{ dB}$ per facet, and the overall insertion loss is reduced by $2 \text{ dB} \pm 0.1 \text{ dB}$ for both devices, leaving insertion loss of $1.6 \text{ dB} \pm 0.1 \text{ dB}$ and $2.8 \text{ dB} \pm 0.1 \text{ dB}$ for the fiber-coupled devices.

Results

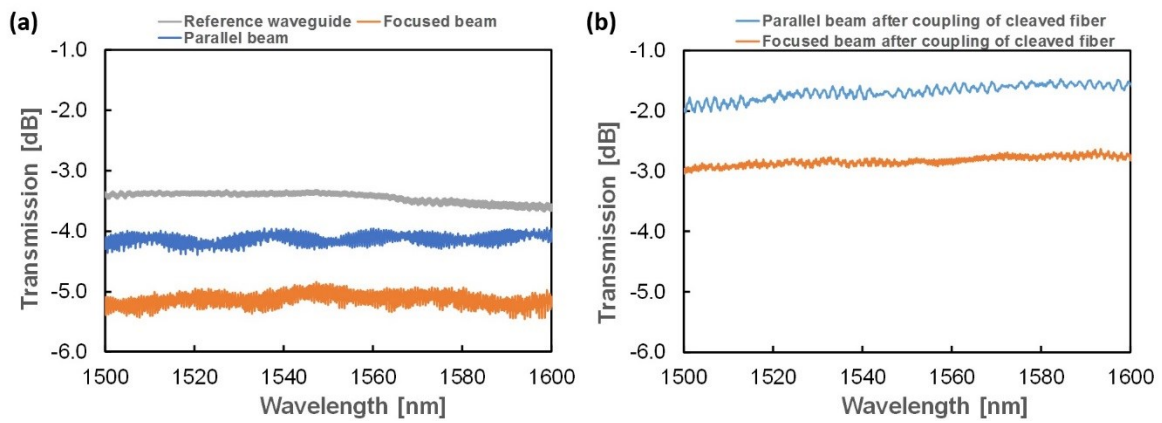


Figure V-30: (a) Insertion loss of the fabricated PolyBoards with integrated ppLN with 840 μm GRIN lenses for a collimated beam (blue curve), 1300 μm GRIN lenses for a focused beam (orange), and an adjacent straight reference waveguide (grey), measured with lensed fibers. (b) Insertion loss for both devices after fixation of input and output cleaved SMF-28 fibers.

The SH conversion efficiency is determined with a tunable continuous-wave laser with adjusted TM polarization at a fixed chip temperature of 40° C. Different power levels for the measurements are set with an erbium-doped fiber amplifier. The output spectrum is measured with an optical spectrum analyzer (OSA) from Yokogawa, and all optical powers measured with the OSA are calculated within the 3 dB bandwidth of the measured SH power. Figure V-31 depicts the SH peaks of both PICs for a pump power of 10 dBm. The output power for the collimating lenses is -57 dBm, which corresponds to a conversion efficiency of 0.005 %/W. The output power increases by 8 dB up to -49 dBm for the focusing lenses or a conversion efficiency of 0.03 %/W.

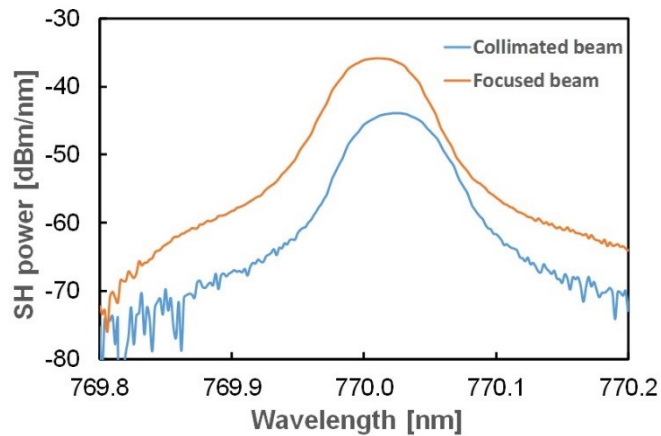


Figure V-31: Comparison of the second harmonic spectrum for the PIC with collimating lenses (blue) and focusing lenses (red).

According to equations (II-79) and (II-80), the SH power depends quadratically on the pump power. In order to verify this relationship, the SH power is measured for different pump powers (Figure V-32(a)) and plotted in a double logarithmic scale against the pump power (Figure V-32(b)). A linear regression of the values in Figure V-32(b) yields a slope of 2.02 ± 0.02 that is in good agreement with the predicted quadratic relationship.

Results

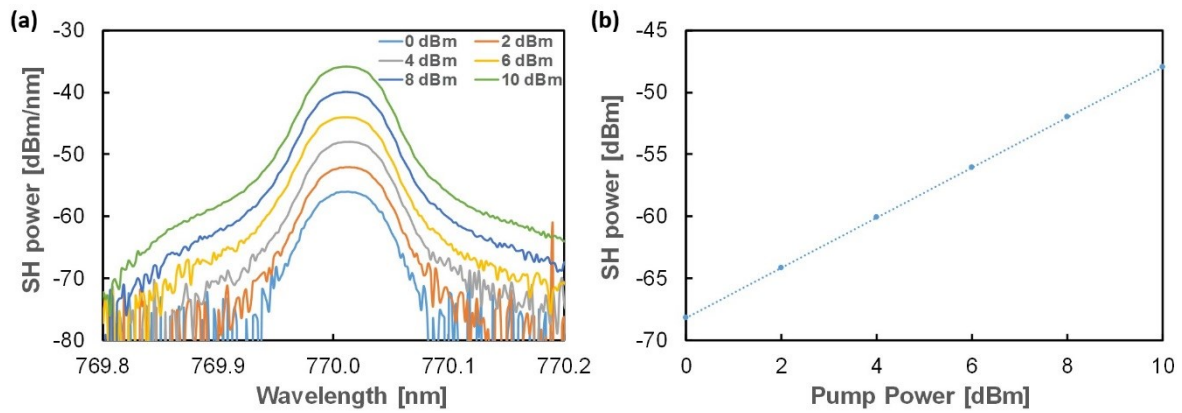


Figure V-32: (a) Influence of pump power onto the SH output spectrum. (b) SH power vs. pump power in a double logarithmic scale with a linear fit of slope 2.02 ± 0.02 that corresponds to a quadratic relationship between pump and SH power.

As a last continuous-wave measurement, the SH bandwidth is measured by variation of the pump wavelength between a wavelength of 1540 nm and 1550 nm at a fixed temperature of 40 °C (Figure V-33).

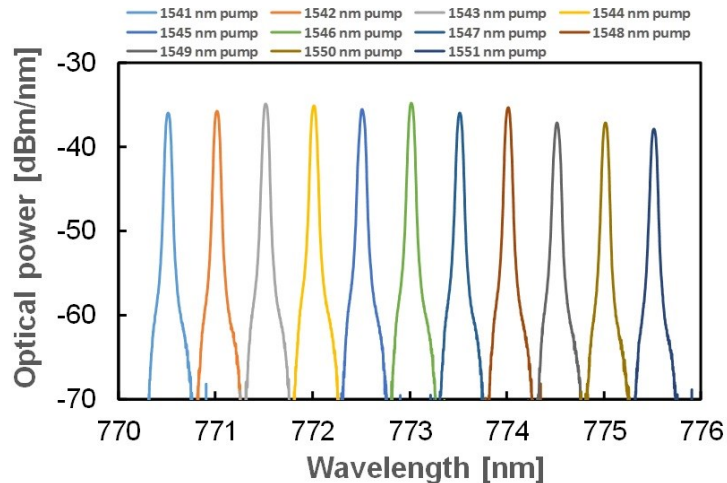


Figure V-33: Tuning of the SH signal for a fixed temperature of 40° C.

3. Characterization with a pulsed laser

Since the conversion efficiency of SHG scales with the optical power, a significant increase in conversion efficiency can be expected for a femtosecond pulsed laser pump source. The femtosecond laser used for the following measurement has an output power of 19 dBm, a 100 MHz repetition rate, and a pulse duration of ~120 fs. This results in peak powers of 68 dBm, or 6.7 kW. The optical spectrum of the chip with focusing lenses measured with an OSA is depicted in Figure V-34. Besides the second harmonic, the third harmonic at 517 nm and the fourth harmonic at 388 nm are also visible in the spectrum.

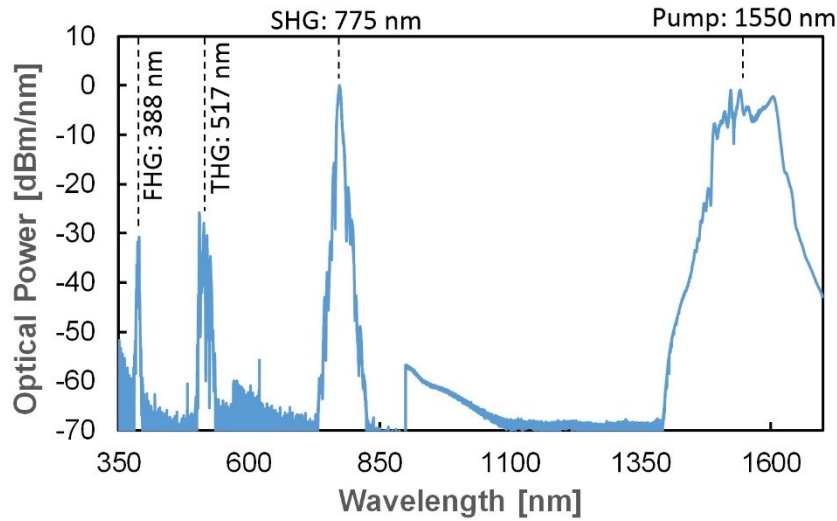


Figure V-34: Optical spectrum of higher harmonic generation with focusing lenses on-chip and the femtosecond laser pump around 1550 nm, the SH at 775 nm, the third harmonic (THG) at 517 nm, and the fourth harmonic (FHG) at 388 nm.

The SH output power increases to 8.2 dBm compared to the -49 dBm achieved with the continuous-wave laser. The output power of the third and fourth harmonics are -20.6 dBm and -28.0 dBm respectively. Corresponding conversion efficiencies are -11 dB, -40 dB, and -47 for the second, third and fourth harmonic. It is noted that even though pump peak powers of 6.7 kW were transferred into the waveguides, no deterioration of the polymers was observed. However, after one hour of testing, the glue used to fix the input fiber started degrading, posing a limit for the overall power that can be used to pump the crystal inside the PolyBoard.

4. Discussion

The measured insertion losses for the fiber-coupled devices in Figure V-30 are 1.6 dB and 2.8 dB for the collimating and focusing lenses respectively. These values also include the input and output fiber-to-chip coupling loss that correspond to 0.5 dB per facet. The excess loss with respect to a reference waveguide are 0.7 dB and 1.8 dB at 1550 nm. The higher loss for the PIC with focusing lenses can be explained by the length of the fabricated GRIN lenses that are 30 μ m shorter than the targeted length of 1330 μ m. Since ppLN crystals have very low absorption loss of \sim 0.01 dB/cm at 1550 nm, the overall loss for the integrated ppLN crystal is also lower than for the integration of the optical isolator from chapter V.B with typical values of $1.2 \text{ dB} \pm 0.2 \text{ dB}$. At 1600 nm, the values are even lower with less than 0.5 dB of excess loss, making it the lowest loss measured for any free-space section in PolyBoard yet.

Overall a conversion efficiency of 0.005 %/W and 0.03 %/W is achieved for the collimating and the focusing lenses in CW operation. Even though the insertion loss of the chip with focusing lenses are 1.2 dB higher compared to the collimating lenses, the conversion efficiency is increased by a factor of 6. Figure VI-30 SH shows a linear relationship with a slope of 2.02 ± 0.02 in a double logarithmic scale between the SH and pump power. This corresponds to a quadratic relationship between the powers as predicted in the equations (II-79) and (II-80). Based on the theory of SHG derived by Boyd and Kleinman elaborated in II.D.3, the achievable conversion efficiency for the PolyBoard integrated ppLN crystal was predicted to be 0.07 %/W for the focusing lenses. Considering the additional loss of the chip, this is in good agreement with the measured conversion efficiency.

SHG with a femtosecond pulsed laser yields a SH power of 8 dBm for an input power of 19 dBm. This corresponds to a conversion efficiency of -11 dB (\sim 8 %) or 100 %/W. Compared to the CW SHG, this is an improvement of four orders of magnitude in terms of conversion efficiency. The SH peak

Results

in Figure V-34 has a 3 dB bandwidth of 6 nm, while the pump bandwidth is much larger with a bandwidth exceeding 100 nm. This means that only a fraction of the pump is actually contributing to SHG. Within the 12 nm bandwidth at 1550 nm that actually contributes to SHG, the conversion efficiency is significantly higher with 45% compared to the 8 % total conversion efficiency calculated with respect to the full bandwidth of the pump. Since the phase-matching acceptance bandwidth scales inversely with the length according to equation (II-79), reducing the crystal length would be beneficial for the overall conversion efficiency to access the whole bandwidth of the femtosecond laser.

An overview of different conversion efficiencies in literature was given in section II.D.5. So far, the highest conversion efficiencies in percent were reported for free-space setups. For example, Taverner et al. achieved a conversion efficiency of 83 % with a pulsed setup [80], and Zhou et al. achieved 52 % with a double resonant cavity scheme [79]. In integrated photonics, mainly two different approaches yielded the highest conversion efficiencies in the last years. The first is based on waveguide inscribed nonlinear crystals, e.g. in [36], where a conversion efficiency of 50 % was reported for femtosecond pulses. The second utilizes nonlinear microring resonators with reported conversion efficiencies between 15 % and 22 % that are especially useful for low power operation with efficiencies of up to 250,000 %/W [75–77]. With 8 % total conversion or 100 %/W conversion efficiency, femtosecond pulse SHG with the free-space section integrated ppLN crystal within this work already yields a good conversion efficiency with a high SH optical power of 8 dBm. Since the experiments were carried out with the chip with focusing lenses with slightly higher loss, two-digit efficiencies in percent should be possible by simply reducing the loss due to offset from the targeted GRIN lens length. A shorter crystal with a higher phase-matching acceptance bandwidth would also be beneficial for the femtosecond laser used in the experiment. Vice versa, using a pulsed laser with a smaller bandwidth and longer pulses would also increase the conversion efficiency.

Even though the conversion efficiency with laser pulses yields much higher efficiencies than the CW experiment, further improvement of the CW efficiency should be the focus in future works because most laser applications require continuous-wave laser sources. The most obvious way to improve the conversion efficiency would be an increased crystal length. According to (II-80), SHG scales linearly with the length of the crystal for a Gaussian beam. The longest possible crystal length, where the Boyd-Kleinman condition would still be fulfilled in close proximity for the GRIN lens free-space section, would be 4 mm. Thus, the conversion efficiency could be improved by a factor of 4 with a longer crystal.

In V.A, the first experiments and promising results for the development of a resonant cavity were discussed. The GRIN lens resonator in V.A had a reflectivity of 80% and intrinsic resonator loss of 2.0 dB, if additional loss of uncoated interfaces are neglected. These values result in an external cavity enhancement factor of $A'_{circ} = 1.5$, meaning that the internal power of the resonator is 1.5 times higher than the pump power [98]. This value of A'_{circ} is only a minor improvement compared to pump power but would already increase the SH power by a factor of 2.25, since SHG scales quadratically with the pump power. One way to improve A'_{circ} , is to build an impedance matched resonant cavity, where the input reflectivity matches the total loss in the resonator, including the transmission from the output mirror. Assuming intrinsic resonator loss of 2 dB measured for the resonator, impedance matching would be achieved for an input reflectivity of 80% and an output reflectivity of >99.9%, resulting in $A'_{circ} = 2.5$ and a 6.25 times increased SH power. Reducing the cavity loss from 1.0 dB to 0.5 dB would further enhance these values to $A'_{circ} = 5.2$ and an increased SH power by a factor of 27.2. Boyd and Kleinman found that the conversion efficiency can also be improved by building a resonant cavity for the second harmonic and not only the pump

Results

wavelength [30]. Thus, the SH conversion efficiency would benefit the most from the development of a double resonant cavity. A final possibility to improve the conversion efficiency would be the hybrid integration of ppLN waveguides instead of bulk crystals. This would be beneficial in two ways because the waveguide confinement offers a higher power density and also the possibility to integrate crystals with a higher length. Even though not covered in this work, first experiments for the coupling of ppLN waveguides and PolyBoard chips to develop a single photon Heralded source were already carried out successfully.

During the experiment with the pulsed laser, not only the second harmonic but also the third and fourth harmonic were observed in the spectrum (Figure V-34). In an experiment where the SH at 775 nm is used explicitly for an application, this would be considered an unwanted parasitic effect, since the higher harmonics might interfere with the application and would require additional filtering. However, since the optical power of the higher harmonics is 29 dB and 36 dB smaller than the second harmonic, this would only be a very weak effect. Nevertheless, this is the first time that wavelengths of green (517 nm) and ultraviolet (387 nm) light were created in the PolyBoard. Similar to second-harmonic generation, a second-order nonlinearity also creates the third and fourth harmonic. Besides SHG, the second-order nonlinearity (equation (II-70)) also enables sum-frequency generation (SFG). In Figure V-34, the third harmonic is created via SFG of the pump wavelength and the second harmonic. The fourth harmonic is created by SHG of the second harmonic. Both processes are enabled by higher-order phase matching (see equation (II-85)), that allows multiple conversion processes to happen simultaneously. For example, third-order phase matching would yield a domain width of 21.1 μm required for SFG from 1550 nm + 775 nm \rightarrow 517 nm, close to the 19.1 μm period of the crystal for first-order phase matching of SHG ((II-86)).

VI. Conclusion

This work successfully demonstrated the possibilities to realize optical isolators, circulators, and SHG in polymer photonic integrated circuits. The challenge of introducing nonreciprocities and nonlinearities in the polymer platform is solved by the creation of on-chip free-space sections that make the insertion of magneto-optic materials and nonlinear crystals with low loss possible. Within this work a theoretical model utilizing Gaussian beam propagation with complex ABCD matrices is applied to the system to predict coupling loss and derive parameters for waveguide-coupled GRIN lenses that create the free-space sections. Based on these findings, a fabrication process for GRIN lenses from GRIN fibers was established. Four PICs, one isolator, also co-integrated with a DBR laser, two circulator designs and one SHG source were demonstrated in the PolyBoard platform.

The integrated isolator, enabled by the integration of a free-space isolator in the PolyBoard, showed a performance close to its well-established free-space counterparts, with measured excess loss below 1 dB for the best devices and an optical peak isolation exceeding 40 dB. This performance is comparable to regular free-space isolators and is to our best knowledge the best-working isolator in integrated photonics. Furthermore, the co-integration of a DBR laser and an optical isolator on a single chip was demonstrated for the first time. During a 10 Gbit/s transmission experiment over a 10 km fiber link, the integrated isolator ensured a stable operation of the DBR laser even at high amounts of optical feedback. Overall, this promises a simplification in photonic packaging designs for lasers, e.g. in fiber-to-the-home applications, because the necessity of free-space components for the isolator implementation is moved from the packaging towards the photonic chip. Even though not shown in this work, the integrated Polyboard isolator was also already successfully co-integrated with a silicon nitride based DBR laser and complex hybrid photonic circuits for Thz communication.

Besides the optical isolator, optical circulators based on a nonreciprocal polarization rotation in the first and a nonreciprocal phase shift in the second design were demonstrated. With minimal excess loss of 4.8 dB and a maximum optical isolation of 10.6 dB, the passively working PBS based circulator is a first demonstration of a polarization-independent optical circulator in the PolyBoard platform. The design still requires a further reduction of the excess loss and improved optical isolation for commercial applications as discussed in V.C.3, but different possibilities to reduce the loss are also discussed within this work. Unique in integrated photonics is the possibility to build a latching switch based on the reversal of the Faraday rotation direction of the magneto-optic crystals with the integrated circulator.

In the second part of this work, second-harmonic generation with an integrated periodically poled lithium niobate crystal was demonstrated. A second harmonic output power of 8 dBm or 6 mW was achieved with a femtosecond laser source. The generation of the third and fourth harmonic in the green and violet wavelength regime respectively also mark the first generation of visible light on the PolyBoard platform. Even though the conversion efficiency demonstrated with a continuous-wave laser source is significantly lower, three options are discussed to improve it. The first is the integration of a longer crystal. The second is the utilization of a resonant cavity design with some promising first results shown in VI.A and the third is the hybrid integration of ppLN waveguides instead of bulk crystals.

Besides demonstrating functional devices like optical isolators and second-harmonic generation sources, this work describes the methods involved in implementing on-chip free-space sections in photonic integrated circuits. This includes a theoretical model of the free-space sections, the fabrication of GRIN lenses for different applications, and the preparation of bulk crystals to be inserted into the PolyBoard. All these methods form a toolset now easily applicable to applications

Conclusion

beyond the ones shown in this work. Thus, the micro-optical bench is established as a fully functional building block of the PolyBoard platform. This opens up many new application fields apart from nonreciprocal and nonlinear elements by simply interchanging the material inside the free-space section. For example two other materials currently being investigated are ppKTP crystals for the creation of entangled photon pairs with parametric down-conversion based on the work of Laudenbach et al. [99], and the integration of diamonds with high nitrogen concentrations are investigated as miniaturized magnetometers for magnetic field measurements similar to the setup described in [100]. Nevertheless, even beyond this, many more potential integrations might come into mind. Together with the resonant cavity design described in V.A.3, the integration of laser gain media and saturable absorbers might enable the development of Q-switched laser, and atomic vapor cells can potentially be used for absolute frequency referencing, opening up branches of new applications that were previously mostly limited to laboratory setups with free-space optics.

Appendix

1. Sellmeier equation for Mg:O doped ppLN

Sellmeier's equation is an empiric function that describes the refractive index of transparent media in dependence of the wavelength λ (in microns), the temperature T (in °C) and the Sellmeyer coefficients a_i and b_i . For 5% MgO:LN used in this work, the Sellmeyer equation is given by [101]:

$$n_e^2 = a_1 + b_1 f + \frac{a_2 + b_2 f}{\lambda^2 - (a_3 + b_3 f)^2} + \frac{a_4 + b_4 f}{\lambda^2 - a_5^2} - a_6 \lambda^2, \quad (0-1)$$

with the temperature dependence

$$f = (T - 24.5^\circ C)(T + 570.82) \quad (0-2)$$

and the coefficients

Sellmeier coefficient	Value
a_1	5.756
a_2	0.0983
a_3	0.202
a_4	189.32
a_5	12.52
a_6	1.32E-02
b_1	2.86E-06
b_2	4.70E-08
b_3	6.11E-08
b_4	1.52E-04

Figure 0-1 depicts a plot of the wavelength dependent refractive index calculated from the Sellmeier equation.

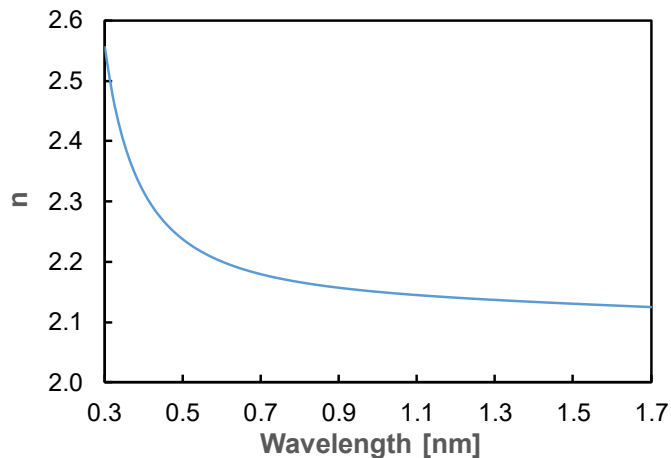


Figure 0-1: Wavelength-dependent plot of the refractive index for the ppLN crystal used in this work, calculated from Sellmeier's equation.

2. Fabry-Pérot resonator and the Airy function

The Airy transmission function A_{trans} , describes the spectral transmission of a Fabry-Pérot resonator:

$$A_{trans} = \frac{I_{trans}}{I_{launch}} = \frac{(1-R)^2 \sqrt{1-L_{ORTL}}}{(1-R)^2 + 4R\sqrt{1-L_{ORTL}} \sin(\frac{\pi}{\Delta\lambda_{FSR}}\lambda + \phi)^2} \quad (0-3)$$

Here, R describes the reflectivity of the coated GRIN lenses, L_{ORTL} the one-way roundtrip loss, and $\Delta\lambda_{FSR}$ is the free-spectral range. More about the physics behind Airy distributions and the Fabry-Pérot resonator can be read in [102]. The free-spectral range can be used to calculate the total length of a resonator, which indicates if the GRIN lenses in the GRIN lens resonator are correctly inserted with the coating facing towards the waveguides. The free-spectral range is defined as the distance between two consecutive transmission maxima in the Fabry-Pérot spectrum and is connected to the length L of the cavity via

$$\Delta\lambda_{FSR} = \frac{\lambda^2}{2nL}, \quad (0-4)$$

where λ is the wavelength in vacuum and n the refractive index.

3. Measurements on thermo-optic components

Figure 0-2 depicts the transmission of an isolated variable optical attenuator structure as described in IV.A.3. At 1550 nm typical excess loss of 1.0 dB with respect to an adjacent reference waveguide can be expected. An optical attenuation of 19 dB is measured for a heater electrode current of 37.5 mA. The spectral oscillations result from the lensed fiber measurement setup used for the characterization.

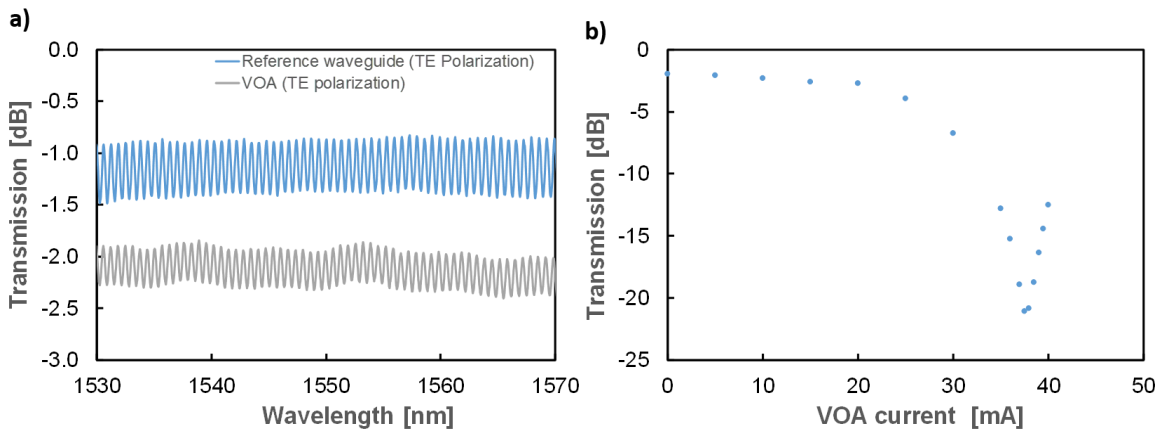


Figure 0-2: Measured optical transmission (a) and an extinction curve (b) of the variable optical attenuator implemented in the MZI circulator.

4. Transparency of rare-earth-doped iron garnets

Figure 0-3 depicts insertion loss measurements of rare-earth-doped iron garnets, similar to those used in this work. Besides high transparency at telecom wavelengths, from 1250 nm – 1600 nm, two additional transparency windows for common laser wavelengths are available. At 1064 nm, the measured loss of the RIGs are slightly below 1 dB and at 785 nm measured insertion loss are around 2 dB.

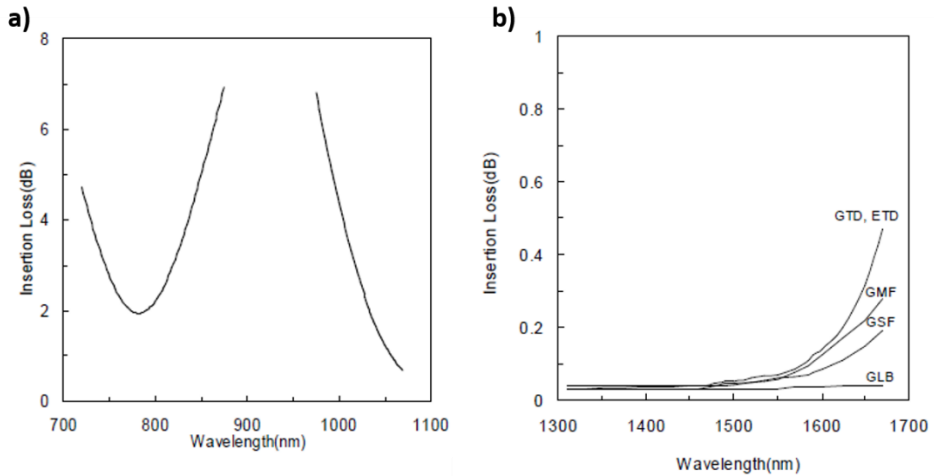


Figure 0-3: Insertion loss measurements of RIGs at different wavelengths, measured at GRANOPT CO., LTD. [103].

5. Measurements on PBS test structures

In order to determine the PER of the PBS structures used in the PBS circulator design in V.C.1, a test structures as depicted in Figure 0-4 is characterized for TE and TM polarization. This helps to determine the reason for the low extinction of the PBS circulator.

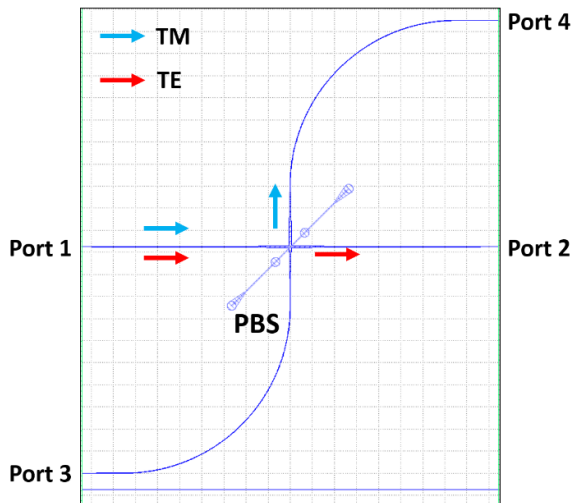


Figure 0-4: Mask layout of the PBS test structure with a four-port configuration similar to the input PBS in the PBS circulator depicted in Figure V-20.

The polarization extinction ratio is measured for two different polarization adjustments. First, the polarization is adjusted within the lab system using an optical lens, a free-space polarization filter, and a detector. Afterwards an output fiber replaces the free-space setup without touching the input fiber, thus maintaining the output polarization of the laboratory system. After a full characterization of the chip, the polarization is adjusted directly at the PBS structure a second time by maximizing the extinction from port 1 to port 2 for TM polarization. After a complete characterization, the measurements are repeated but with a maximized extinction for TE polarization from port 3 to port 2. The three different polarization measurements and the insertion loss measurement are depicted in Figure 0-5.

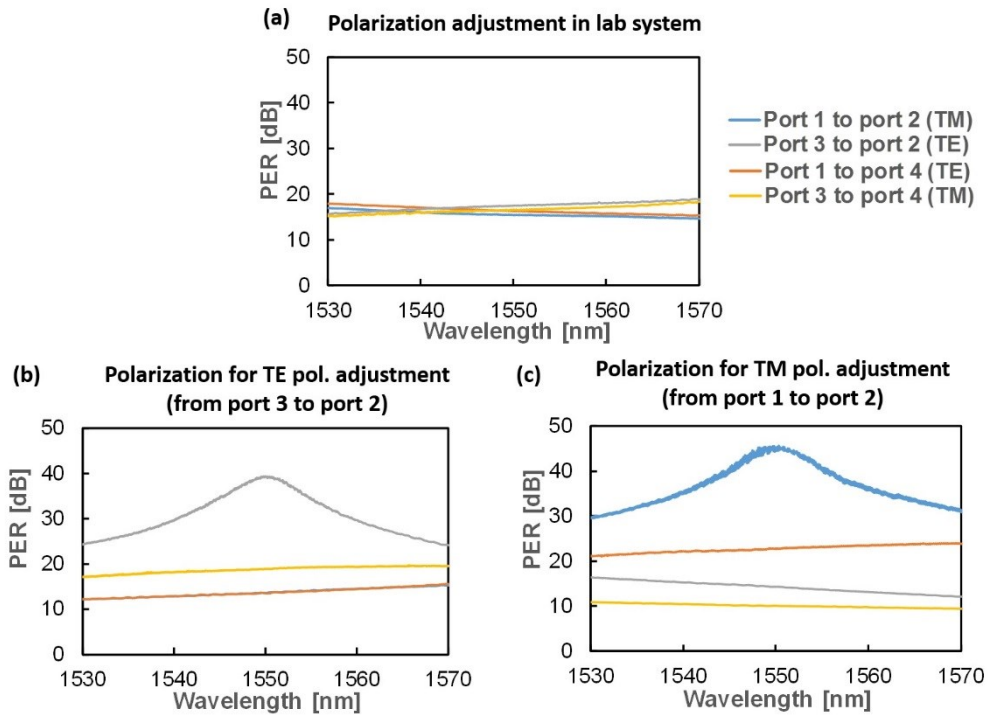


Figure 0-5: Polarization extinction ratio (PER) of the PBS chip depicted in Figure 0-4 for differently adjusted polarizations. In (a), the polarization was adjusted in a free-space setup, while the polarization in (b) to (d) was adjusted on-chip for different port configurations.

For the polarization adjusted in free-space (Figure II-1(a)), a PER of 15.5 dB – 17.5 dB is measured depending on the port and polarization configuration. No distinct peak is visible in this measurement. In the following two measurements (Figure II-1(b-d)), the directly adjusted polarization shows a high peak PER beyond 40 dB, but changing the port configuration results in a significant PER drop to values between 10.0 dB and 22.8 dB for the different port and polarization configurations. Since the separately measured Faraday rotator and HWP show a good PER beyond 30 dB, the PBS filters in combination with the (bent) polymer waveguides is most likely the reason for low optical isolation measured in the PBS circulator in section V.C.1.

6. Measurements on Mach-Zehnder-interferometric test structures

Before characterization of the actual circulator structure in V.C.2, a MZI without any free-space sections but with integrated phase shifters and VOAs is characterized. Depending on the relative optical phase in both arms of the MZI that can be adjusted with the phase shifters, it is possible to switch between transmission and extinction for all input and output port combinations. Figure 0-6 depicts the measurements for TE and TM polarization from port 1 to port 2.

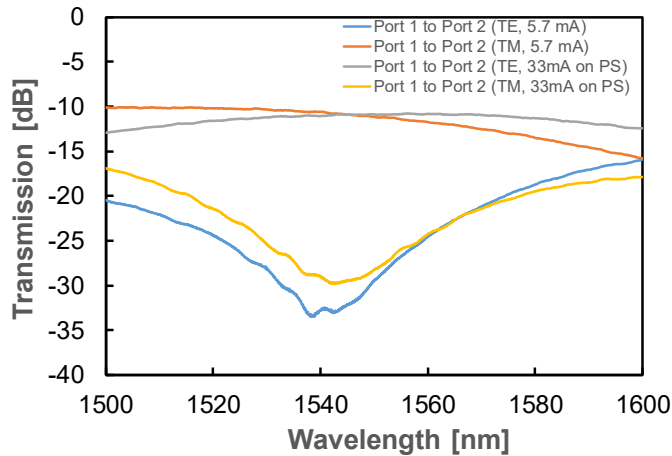


Figure 0-6: Optical transmission from port 1 to port 2 for a Mach-Zehnder interferometric test structure for TE and TM polarization.

For a phase shifter current of 0 mA, TM polarized light is transmitted, while TE polarized light is blocked at 1550 nm. At a phase shifter current of 33 mA, transmission and extinction are reversed for both polarizations, and the TE polarized light is transmitted and TM polarized light blocked. Even though switching with the phase shifter works as expected, the fabricated MZI has a strong polarization dependence. If TE polarized light is transmitted, TM polarized light is blocked and vice versa. This indicates that a phase shift of $\sim\pi$ is induced between both polarizations during the propagation of the MZI.

References

- [1] J. Bardeen and W. H. Brattain, "Physical Principles Involved in Transistor Action," *Phys. Rev.*, vol. 75, no. 8, pp. 1208–1225, 1949, doi: 10.1103/physrev.75.1208.
- [2] W. Shockley, G. L. Pearson, and J. R. Haynes, "Hole Injection in Germanium-Quantitative Studies and Filamentary Transistors," *Bell System Technical Journal*, vol. 28, no. 3, pp. 344–366, 1949, doi: 10.1002/j.1538-7305.1949.tb03641.x.
- [3] C. Sah, R. Noyce, and W. Shockley, "Carrier Generation and Recombination in P-N Junctions and P-N Junction Characteristics," *Proc. IRE*, vol. 45, no. 9, pp. 1228–1243, 1957, doi: 10.1109/jrproc.1957.278528.
- [4] J. S. Kilby, "Invention of the integrated circuit," *IEEE Trans. Electron Devices*, vol. 23, no. 7, pp. 648–654, 1976, doi: 10.1109/T-ED.1976.18467.
- [5] R. R. Schaller, "Moore's law: past, present and future," *IEEE Spectr.*, vol. 34, no. 6, pp. 52–59, 1997, doi: 10.1109/6.591665.
- [6] B. M. Leiner *et al.*, "A Brief History of the Internet," Jan. 1999. [Online]. Available: <https://arxiv.org/pdf/cs/9901011>
- [7] S. Cherry, "Edholm's law of bandwidth," *IEEE Spectr.*, vol. 41, no. 7, pp. 58–60, 2004, doi: 10.1109/MSPEC.2004.1309810.
- [8] K. C. Kao and G. A. Hockham, "Dielectric-fibre surface waveguides for optical frequencies," *Proceedings of the Institution of Electrical Engineers*, vol. 113, no. 7, pp. 1151–1158, 1966, doi: 10.1049/piee.1966.0189.
- [9] T. H. MAIMAN, "Stimulated Optical Radiation in Ruby," *Nature*, vol. 187, no. 4736, pp. 493–494, 1960, doi: 10.1038/187493a0.
- [10] Cisco, *Cisco Annual Internet Report - Cisco Annual Internet Report (2018–2023) White Paper*. [Online]. Available: <https://www.cisco.com/c/en/us/solutions/collateral/executive-perspectives/annual-internet-report/white-paper-c11-741490.html> (accessed: Jun. 1 2021).
- [11] R.-J. Essiambre, G. Kramer, P. J. Winzer, G. J. Foschini, and B. Goebel, "Capacity Limits of Optical Fiber Networks," *Journal of Lightwave Technology*, vol. 28, no. 4, pp. 662–701, 2010, doi: 10.1109/JLT.2009.2039464.
- [12] M. Smit, K. Williams, and J. van der Tol, "Past, present, and future of InP-based photonic integration," *APL Photonics*, vol. 4, no. 5, p. 50901, 2019, doi: 10.1063/1.5087862.
- [13] H. Kroemer, "A proposed class of hetero-junction injection lasers," *Proceedings of the IEEE*, vol. 51, no. 12, pp. 1782–1783, 1963, doi: 10.1109/proc.1963.2706.
- [14] M. Suzuki, Y. Noda, H. Tanaka, S. Akiba, Y. Kushiro, and H. Isshiki, "Monolithic integration of InGaAsP/InP distributed feedback laser and electroabsorption modulator by vapor phase epitaxy," *Journal of Lightwave Technology*, vol. 5, no. 9, pp. 1277–1285, 1987, doi: 10.1109/JLT.1987.1075650.
- [15] B. Corcoran *et al.*, "Ultra-dense optical data transmission over standard fibre with a single chip source," *Nat Commun*, vol. 11, no. 1, p. 2568, 2020, doi: 10.1038/s41467-020-16265-x.
- [16] S. Voinigescu, *High-frequency integrated circuits*. Cambridge: Cambridge University Press, 2013. [Online]. Available: <http://site.ebrary.com/lib/alltitles/docDetail.action?docID=10661188>
- [17] T. Komljenovic, D. Huang, P. Pintus, M. A. Tran, M. L. Davenport, and J. E. Bowers, "Photonic Integrated Circuits Using Heterogeneous Integration on Silicon," *Proceedings of the IEEE*, vol. 106, no. 12, pp. 2246–2257, 2018, doi: 10.1109/JPROC.2018.2864668.

-
- [18] J. van der Tol, Y. S. Oei, U. Khalique, R. Nötzel, and M. K. Smit, "InP-based photonic circuits: Comparison of monolithic integration techniques," *Progress in Quantum Electronics*, vol. 34, no. 4, pp. 135–172, 2010, doi: 10.1016/j.pquantelec.2010.02.001.
 - [19] A. M. Rollins and J. A. Izatt, "Optimal interferometer designs for optical coherence tomography," *Optics letters*, vol. 24, no. 21, pp. 1484–1486, 1999, doi: 10.1364/ol.24.001484.
 - [20] S. A. Babin, S. I. Kablukov, I. S. Shelemba, and A. A. Vlasov, "An interrogator for a fiber Bragg sensor array based on a tunable erbium fiber laser," *Laser Phys.*, vol. 17, no. 11, pp. 1340–1344, 2007, doi: 10.1134/S1054660X07110138.
 - [21] N. J. Doran, K. Sugden, I. Bennion, and J. Williams, "Fibre dispersion compensation using a chirped in-fibre Bragg grating," *Electronics Letters*, vol. 30, no. 12, pp. 985–987, 1994, doi: 10.1049/el:19940661.
 - [22] R. J. Potton, "Reciprocity in optics," *Rep. Prog. Phys.*, vol. 67, no. 5, pp. 717–754, 2004, doi: 10.1088/0034-4885/67/5/R03.
 - [23] Paolo Pintus, Duanni Huang, Chong Zhang, Yuya Shoji, Tetsuya Mizumoto, and John E. Bowers, "Microring-Based Optical Isolator and Circulator with Integrated Electromagnet for Silicon Photonics," *J. Lightwave Technol., JLT*, vol. 35, no. 8, pp. 1429–1437, 2017.
 - [24] C. Zhang, P. Dulal, B. J. H. Stadler, and D. C. Hutchings, "Monolithically-Integrated TE-mode 1D Silicon-on-Insulator Isolators using Seedlayer-Free Garnet," *Scientific reports*, vol. 7, no. 1, p. 5820, 2017, doi: 10.1038/s41598-017-06043-z.
 - [25] Y. Zhang *et al.*, "Monolithic integration of broadband optical isolators for polarization-diverse silicon photonics," *Optica*, vol. 6, no. 4, p. 473, 2019, doi: 10.1364/optica.6.000473.
 - [26] D. Huang, P. Pintus, Y. Shoji, P. Morton, T. Mizumoto, and J. E. Bowers, "Integrated broadband Ce:YIG/Si Mach-Zehnder optical isolators with over 100 nm tuning range," *Opt. Lett., OL*, vol. 42, no. 23, pp. 4901–4904, 2017, doi: 10.1364/OL.42.004901.
 - [27] T. Mizumoto, R. Takei, and Y. Shoji, "Waveguide Optical Isolators for Integrated Optics," *IEEE J. Quantum Electron.*, vol. 48, no. 2, pp. 252–260, 2012, doi: 10.1109/jqe.2011.2168194.
 - [28] Y. Sobe, Y. Shoji, K. Sakurai, and T. Mizumoto, "GaInAsP/InP MZI waveguide optical isolator integrated with spot size converter," *Opt. Express, OE*, vol. 21, no. 13, pp. 15373–15381, 2013, doi: 10.1364/OE.21.015373.
 - [29] H. Shimizu and Y. Nakano, "Monolithic Integration of a Waveguide Optical Isolator With a Distributed Feedback Laser Diode in the 1.5–1.6 μm Wavelength Range," *IEEE Photon. Technol. Lett.*, vol. 19, no. 24, pp. 1973–1975, 2007, doi: 10.1109/LPT.2007.909697.
 - [30] G. D. Boyd and D. A. Kleinman, "Parametric Interaction of Focused Gaussian Light Beams," *Journal of Applied Physics*, vol. 39, no. 8, pp. 3597–3639, 1968, doi: 10.1063/1.1656831.
 - [31] G. Lifante, *Integrated photonics: Fundamentals*. Hoboken, NJ: J. Wiley, 2003.
 - [32] R. Nagarajan *et al.*, "InP Photonic Integrated Circuits," *IEEE Journal of Selected Topics in Quantum Electronics*, vol. 16, no. 5, pp. 1113–1125, 2010, doi: 10.1109/JSTQE.2009.2037828.
 - [33] J. E. Bowers *et al.*, "Recent advances in silicon photonic integrated circuits," in *Next-Generation Optical Communication: Components, Sub-Systems, and Systems V*, San Francisco, California, United States, 2016, p. 977402.
 - [34] Y. Lin *et al.*, "Characterization of Hybrid InP-TriPleX Photonic Integrated Tunable Lasers Based on Silicon Nitride (Si₃N₄/SiO₂) Microring Resonators for Optical Coherent System," *IEEE Photonics J.*, vol. 10, no. 3, pp. 1–8, 2018, doi: 10.1109/JPHOT.2018.2842026.

-
- [35] LIGENTEC, *Silicon nitride - LIGENTEC*. [Online]. Available: <https://www.ligentec.com/siliconnitride-ligentec/> (accessed: Jun. 2 2021).
 - [36] M. Jankowski *et al.*, “Ultrabroadband nonlinear optics in nanophotonic periodically poled lithium niobate waveguides,” *Optica*, vol. 7, no. 1, p. 40, 2020, doi: 10.1364/OPTICA.7.000040.
 - [37] M. Bock, A. Lenhard, C. Chunnillall, and C. Becher, “Highly efficient heralded single-photon source for telecom wavelengths based on a PPLN waveguide,” *Opt. Express, OE*, vol. 24, no. 21, pp. 23992–24001, 2016, doi: 10.1364/OE.24.023992.
 - [38] E. L. Wooten *et al.*, “A review of lithium niobate modulators for fiber-optic communications systems,” *IEEE Journal of Selected Topics in Quantum Electronics*, vol. 6, no. 1, pp. 69–82, 2000, doi: 10.1109/2944.826874.
 - [39] J. Wang *et al.*, “Hybrid-Integrated Polarization Diverse Coherent Receiver Based on Polymer PLC,” *IEEE Photon. Technol. Lett.*, vol. 24, no. 19, pp. 1718–1721, 2012, doi: 10.1109/LPT.2012.2213299.
 - [40] H. Li *et al.*, “Hybrid InP/Polymer Optical Line Terminals for 40-Channel 100-GHz spectrum-sliced WDM-PON,” in *39th European Conference and Exhibition on Optical Communication (ECOC 2013)*: 22-26 Sept. 2013, London, UK, 2013, pp. 237–239.
 - [41] Z. Zhang *et al.*, “40 nm Tuneable Source for Colourless ONUs based on Dual Hybridly Integrated Polymer Waveguide Grating Lasers,” in *39th European Conference and Exhibition on Optical Communication (ECOC 2013)*: 22-26 Sept. 2013, London, UK, 2013, pp. 189–191.
 - [42] Z. Zhang and N. Keil, “Thermo-optic devices on polymer platform,” *Optics Communications*, vol. 362, pp. 101–114, 2016, doi: 10.1016/j.optcom.2015.08.026.
 - [43] M. Happach *et al.*, “On-chip free beam optics on a polymer-based photonic integration platform,” *Opt. Express, OE*, vol. 25, no. 22, pp. 27665–27670, 2017, doi: 10.1364/OE.25.027665.
 - [44] D. d. Felipe *et al.*, “Polymer-based Integrated Tuneable Laser with On-Chip Wavelength Locker,” in *ECOC 2016; 42nd European Conference on Optical Communication*, 2016, pp. 1–3.
 - [45] B. E. A. Saleh and M. C. Teich, *Fundamentals of photonics*. New York: Wiley, 1991.
 - [46] R. Weinstock, *Calculus of Variations*. Newburyport: Dover Publications, 2012. [Online]. Available: <http://gbv.eblib.com/patron/FullRecord.aspx?p=1900985>
 - [47] S. Yuan and N. A. Riza, “General formula for coupling-loss characterization of single-mode fiber collimators by use of gradient-index rod lenses,” *Appl. Opt., AO*, vol. 38, no. 15, pp. 3214–3222, 1999, doi: 10.1364/AO.38.003214.
 - [48] A. E. Siegman, *Lasers*. Mill Valley, California: University Science Books, 1986.
 - [49] R. E. Wagner and W. J. Tomlinson, “Coupling efficiency of optics in single-mode fiber components,” *Applied optics*, vol. 21, no. 15, pp. 2671–2688, 1982, doi: 10.1364/AO.21.002671.
 - [50] Y. K. Chen *et al.*, “Low-crosstalk and compact optical add-drop multiplexer using a multiport circulator and fiber Bragg gratings,” *IEEE Photon. Technol. Lett.*, vol. 12, no. 10, pp. 1394–1396, 2000, doi: 10.1109/68.883841.
 - [51] D. Jalas *et al.*, “What is — and what is not — an optical isolator,” *Nature Photon*, vol. 7, no. 8, pp. 579–582, 2013, doi: 10.1038/nphoton.2013.185.
 - [52] C. G. Poulton, R. Pant, A. Byrnes, S. Fan, M. J. Steel, and B. J. Eggleton, “Design for broadband on-chip isolator using Stimulated Brillouin Scattering in dispersion-engineered chalcogenide waveguides,” *Opt. Express, OE*, vol. 20, no. 19, pp. 21235–21246, 2012, doi: 10.1364/OE.20.021235.

-
- [53] Zongfu Yu and Shanhui Fan, "Complete optical isolation created by indirect interband photonic transitions," *Nature Photon.*, vol. 3, no. 2, pp. 91–94, 2009, doi: 10.1038/nphoton.2008.273.
 - [54] P. Hansen and J.-P. Krumme, "Magnetic and magneto-optical properties of garnet films," *Thin Solid Films*, vol. 114, 1-2, pp. 69–107, 1984, doi: 10.1016/0040-6090(84)90337-7.
 - [55] V. J. Fratello, S. J. Licht, and C. D. Brandle, "Innovative improvements in bismuth-doped rare-earth iron garnet Faraday rotators," *IEEE Trans. Magn.*, vol. 32, no. 5, pp. 4102–4107, 1996, doi: 10.1109/20.539312.
 - [56] Thorlabs - IO-2.5-1310-VLP Free-Space Isolator, 1310 nm, Ø2.3 mm Max Beam, 0.4 W Max (accessed: Apr. 26 2021).
 - [57] Thorlabs - IO-G-1550-APC Fiber Isolator, 1550 nm, PM, 300 mW, FC/APC (accessed: Apr. 26 2021).
 - [58] Thorlabs - 6015-3-APC Fiber Optic Circulator, 1525 - 1610 nm, SMF, FC/APC (accessed: Apr. 26 2021).
 - [59] N. Sugimoto *et al.*, "Waveguide polarization-independent optical circulator," *IEEE Photon. Technol. Lett.*, vol. 11, no. 3, pp. 355–357, 1999, doi: 10.1109/68.748233.
 - [60] L. Bi *et al.*, "On-chip optical isolation in monolithically integrated non-reciprocal optical resonators," *Nat. Photonics*, vol. 5, no. 12, pp. 758–762, 2011, doi: 10.1038/nphoton.2011.270.
 - [61] Y. J. Cheng, Q. D. Huang, Y. R. Wang, and J. L.-W. Li, "Narrowband Substrate Integrated Waveguide Isolators," *IEEE Microw. Wireless Compon. Lett.*, vol. 24, no. 10, pp. 698–700, 2014, doi: 10.1109/LMWC.2014.2344440.
 - [62] S. Hua, J. Wen, X. Jiang, Q. Hua, L. Jiang, and M. Xiao, "Demonstration of a chip-based optical isolator with parametric amplification," *Nat Commun*, vol. 7, no. 1, p. 13657, 2016, doi: 10.1038/ncomms13657.
 - [63] S. Ghosh, S. Keyvaninia, W. van Roy, T. Mizumoto, G. Roelkens, and R. Baets, "Adhesively bonded Ce:YIG/SOI integrated optical circulator," *Opt. Lett., OL*, vol. 38, no. 6, pp. 965–967, 2013, doi: 10.1364/OL.38.000965.
 - [64] K. Wang *et al.*, "Four-Wave-Mixing-Based Silicon Integrated Optical Isolator With Dynamic Non-Reciprocity," *IEEE Photon. Technol. Lett.*, vol. 28, no. 16, pp. 1739–1742, 2016, doi: 10.1109/LPT.2016.2565460.
 - [65] E. Hecht, *Optics*, 5th ed. Boston, Columbus, Indianapolis: Pearson, 2017.
 - [66] L. B. Soldano and E. Pennings, "Optical multi-mode interference devices based on self-imaging: principles and applications," *J. Lightwave Technol., JLT*, vol. 13, no. 4, pp. 615–627, 1995, doi: 10.1109/50.372474.
 - [67] R. W. Boyd, *Nonlinear optics*, 3rd ed. Amsterdam: Elsevier/Academic Press, 2008. [Online]. Available: <http://site.ebrary.com/lib/alltitles/docDetail.action?docID=10258886>
 - [68] Y. F. Chen and Y. C. Chen, "Analytical functions for the optimization of second-harmonic generation and parametric generation by focused Gaussian beams," *Appl Phys B*, vol. 76, no. 6, pp. 645–647, 2003, doi: 10.1007/s00340-003-1190-y.
 - [69] S. Guha, "Second-harmonic generation efficiency of a focused Gaussian beam in presence of pump depletion," in *Technical Digest. Summaries of Papers Presented at the Conference on Lasers and Electro-Optics. Conference Edition. 1998 Technical Digest Series, Vol.6 (IEEE Cat. No.98CH36178)*, San Francisco, CA, USA, May. 1998 - May. 1998, pp. 391–392.

-
- [70] S. Guha and L. P. Gonzalez, "Theory of second harmonic generation in presence of diffraction, beam walk-off, and pump depletion," in *Nonlinear Frequency Generation and Conversion: Materials, Devices, and Applications VI*, San Jose, CA, 2007, 64550W.
 - [71] D. S. Hum and M. M. Fejer, "Quasi-phasematching," *Comptes Rendus Physique*, vol. 8, no. 2, pp. 180–198, 2007, doi: 10.1016/j.crhy.2006.10.022.
 - [72] J. A. Armstrong, N. Bloembergen, J. Ducuing, and P. S. Pershan, "Interactions between Light Waves in a Nonlinear Dielectric," *Phys. Rev.*, vol. 127, no. 6, pp. 1918–1939, 1962, doi: 10.1103/PhysRev.127.1918.
 - [73] R. Paschotta, *Quasi-phase Matching*. [Online]. Available: https://www.rp-photonics.com/quasi_phase_matching.html (accessed: Jun. 3 2021).
 - [74] M. Yamada, N. Nada, M. Saitoh, and K. Watanabe, "First-order quasi-phase matched LiNbO₃ waveguide periodically poled by applying an external field for efficient blue second-harmonic generation," *Appl. Phys. Lett.*, vol. 62, no. 5, pp. 435–436, 1993, doi: 10.1063/1.108925.
 - [75] X. Lu, G. Moille, A. Rao, D. A. Westly, and K. Srinivasan, "Efficient photoinduced second-harmonic generation in silicon nitride photonics," *Nature Photon*, vol. 15, no. 2, pp. 131–136, 2021, doi: 10.1038/s41566-020-00708-4.
 - [76] J. Lu *et al.*, "Periodically poled thin-film lithium niobate microring resonators with a second-harmonic generation efficiency of 250,000%/W," *Optica*, vol. 6, no. 12, p. 1455, 2019, doi: 10.1364/OPTICA.6.001455.
 - [77] X. Guo, C.-L. Zou, and H. X. Tang, "Second-harmonic generation in aluminum nitride microrings with 2500%/W conversion efficiency," *Optica*, vol. 3, no. 10, p. 1126, 2016, doi: 10.1364/OPTICA.3.001126.
 - [78] S. S. Sané *et al.*, "11 W narrow linewidth laser source at 780 nm for laser cooling and manipulation of Rubidium," *Opt. Express, OE*, vol. 20, no. 8, pp. 8915–8919, 2012, doi: 10.1364/OE.20.008915.
 - [79] M. Zhou *et al.*, "52% optical-to-optical conversion efficiency in a compact 1.5 W 532 nm second harmonic generation laser with intracavity periodically-poled MgO:LiNbO₃," *Laser Phys.*, vol. 20, no. 7, pp. 1568–1571, 2010, doi: 10.1134/S1054660X10130232.
 - [80] D. Taverner, P. Britton, P. G. Smith, D. J. Richardson, G. W. Ross, and D. C. Hanna, "Highly efficient second-harmonic and sum-frequency generation of nanosecond pulses in a cascaded erbium-doped fiber:periodically poled lithium niobate source," *Optics letters*, vol. 23, no. 3, pp. 162–164, 1998, doi: 10.1364/ol.23.000162.
 - [81] G. N. Lawrence, "Optical Modeling," *Applied Optics and Optical Engineering, Volume XI*, vol. 11, p. 125, 1992.
 - [82] X. Jiang *et al.*, "Compact variable optical attenuator based on multimode interference coupler," *IEEE Photon. Technol. Lett.*, vol. 17, no. 11, pp. 2361–2363, 2005, doi: 10.1109/LPT.2005.857238.
 - [83] D. de Felipe *et al.*, "Polymer-Based External Cavity Lasers: Tuning Efficiency, Reliability, and Polarization Diversity," *IEEE Photon. Technol. Lett.*, vol. 26, no. 14, pp. 1391–1394, 2014, doi: 10.1109/LPT.2014.2324760.
 - [84] J. C. Palais, "Fiber coupling using graded-index rod lenses," *Applied optics*, vol. 19, no. 12, pp. 2011–2018, 1980, doi: 10.1364/AO.19.002011.
 - [85] M. Saruwatari and T. Sugie, "Efficient laser diode to single-mode fiber coupling using a combination of two lenses in confocal condition," *IEEE J. Quantum Electron.*, vol. 17, no. 6, pp. 1021–1027, 1981, doi: 10.1109/JQE.1981.1071230.

- [86] J. Knittel, L. Schnieder, G. Buess, B. Messerschmidt, and T. Possner, "Endoscope-compatible confocal microscope using a gradient index-lens system," *Optics Communications*, vol. 188, 5-6, pp. 267–273, 2001, doi: 10.1016/S0030-4018(00)01164-0.
- [87] A. Yariv, *Optical Electronics*. Philadelphia, PA: Saunders College Publishing, 1991. [Online]. Available: <https://authors.library.caltech.edu/106173/>
- [88] M. Bagheri *et al.*, "Passively mode-locked interband cascade optical frequency combs," *Sci Rep*, vol. 8, no. 1, p. 3322, 2018, doi: 10.1038/s41598-018-21504-9.
- [89] G. Berden, R. Peeters, and G. Meijer, "Cavity ring-down spectroscopy: Experimental schemes and applications," *International Reviews in Physical Chemistry*, vol. 19, no. 4, pp. 565–607, 2000, doi: 10.1080/014423500750040627.
- [90] D. Skoczowsky *et al.*, "Monolithic ring resonator with PPLN crystal for efficient cw SHG of 976 nm emitted by a diode laser," in *Nonlinear Frequency Generation and Conversion: Materials, Devices, and Applications VIII*, San Jose, CA, 2009, 71970K.
- [91] R. Kazarinov and C. Henry, "The relation of line narrowing and chirp reduction resulting from the coupling of a semiconductor laser to passive resonator," *IEEE J. Quantum Electron.*, vol. 23, no. 9, pp. 1401–1409, 1987, doi: 10.1109/JQE.1987.1073531.
- [92] R. Tkach and A. Chraplyvy, "Regimes of feedback effects in 1.5-μm distributed feedback lasers," *J. Lightwave Technol., JLT*, vol. 4, no. 11, pp. 1655–1661, 1986, doi: 10.1109/JLT.1986.1074666.
- [93] S. Donati and R.-H. Horng, "The Diagram of Feedback Regimes Revisited," *IEEE Journal of Selected Topics in Quantum Electronics*, vol. 19, no. 4, p. 1500309, 2013, doi: 10.1109/JSTQE.2012.2234445.
- [94] Z. Chen, L. yang, X. Wang, J. Wang, and Y. Hang, "Highly transparent terbium gallium garnet crystal fabricated by the floating zone method for visible–infrared optical isolators," *Optical Materials*, vol. 46, pp. 12–15, 2015, doi: 10.1016/j.optmat.2015.03.034.
- [95] D. Vojna, O. Slezák, A. Lucianetti, and T. Mocek, "Verdet Constant of Magneto-Active Materials Developed for High-Power Faraday Devices," *Applied Sciences*, vol. 9, no. 15, p. 3160, 2019, doi: 10.3390/app9153160.
- [96] M. Prakasam *et al.*, "Crystal growth and analysis of ohmic contact and magneto-optical isolator properties of cadmium manganese telluride," *Journal of Crystal Growth*, vol. 318, no. 1, pp. 533–538, 2011, doi: 10.1016/j.jcrysgro.2010.10.210.
- [97] H.-B. Liu and F. CHOLLET, "Moving Polymer Waveguides and Latching Actuator for 2 x 2 MEMS Optical Switch," *J. Microelectromech. Syst.*, vol. 18, no. 3, pp. 715–724, 2009, doi: 10.1109/JMEMS.2009.2017073.
- [98] N. Ismail, C. C. Kores, D. Geskus, and M. Pollnau, "Fabry-Pérot resonator: spectral line shapes, generic and related Airy distributions, linewidths, finesse, and performance at low or frequency-dependent reflectivity," *Opt. Express, OE*, vol. 24, no. 15, pp. 16366–16389, 2016, doi: 10.1364/OE.24.016366.
- [99] F. Laudenbach, S. Kalista, M. Hentschel, P. Walther, and H. Hübel, "A novel single-crystal & single-pass source for polarisation- and colour-entangled photon pairs," *Sci Rep*, vol. 7, no. 1, p. 7235, 2017, doi: 10.1038/s41598-017-07781-w.
- [100] V. M. Acosta, E. Bauch, A. Jarmola, L. J. Zipp, M. P. Ledbetter, and D. Budker, "Broadband magnetometry by infrared-absorption detection of nitrogen-vacancy ensembles in diamond," *Appl. Phys. Lett.*, vol. 97, no. 17, p. 174104, 2010, doi: 10.1063/1.3507884.

- [101] O. Gayer, Z. Sacks, E. Galun, and A. Arie, "Temperature and wavelength dependent refractive index equations for MgO-doped congruent and stoichiometric LiNbO₃," *Appl Phys B*, vol. 91, no. 2, pp. 343–348, 2008, doi: 10.1007/s00340-008-2998-2.
- [102] M. Pollnau and M. Eichhorn, "Spectral coherence, Part I: Passive-resonator linewidth, fundamental laser linewidth, and Schawlow-Townes approximation," *Progress in Quantum Electronics*, vol. 72, p. 100255, 2020, doi: 10.1016/j.pquantelec.2020.100255.
- [103] Graonopt, *Product information on RIGs, GRANOPT*. [Online]. Available: <http://www.granopt.jp/en/product.html> (accessed: May 31 2021).

Danksagung

An dieser Stelle möchte ich mich bei all denjenigen bedanken die mich während der Anfertigung dieser Dissertation unterstützt haben.

Ein besonderer Dank gilt Prof. Martin Schell für die Betreuung der Arbeit als Doktorvater und die Einführung in die Welt der Photonik auf zahlreichen Messen und Konferenzen sowie am Fraunhofer Heinrich Hertz Institut.

Außerdem danke ich Moritz Kleinert und Lennart Jehle für den regen Austausch, die zahlreichen häufig sehr kollegialen und humorvollen Diskussionen insbesondere im Messlabor und das Korrekturlesen dieser Arbeit.

Weiter möchte ich mich bei Norbert Keil und der gesamten Hybrid PICs-Gruppe für die sehr angenehme Arbeitsatmosphäre bedanken aus der viele Freundschaften auch jenseits der Arbeit hervorgegangen sind.